Synthesis of Fe-SSZ-13 using a ferrocene-based structure directing agent for the NH3 -SCR reaction

ADAM DEACON

Synthesis of Fe-SSZ-13 using a ferrocene-based structure directing agent for the NH_3 -SCR reaction

Adam Deacon

MSc by research Thesis

Department of Chemistry

Durham University

Supervisors: Dr Russell A. Taylor

Dr Alessandro Turrina

Abstract

Nitrogen oxide (NO_X) emissions from industrial processes and transportation continues to cause harm to both the environment and human health through the production of acid rain, depleting the ozone layer and causing cardiovascular and respiratory problems in humans. Over the past 50 years selective catalytic reduction of NO_X by ammonia (NH_3-SCR) has been successfully used to limit NO_x emissions. Iron and copper zeolite catalysts have been extensively used for NH_3-SCR due to their high activity, high selectivity to N_2 and low N_2O formation. While Cu-based zeolites are favoured for NH_3-SCR application due to their excellent activity and stability at lower temperatures, Fe-zeolites have shown greater stability at higher temperatures typical of diesel exhausts and produce less N_2O. Improving the lower temperature activity of Fe-Zeolites is of great interest to industry.

This thesis outlines the use of (Ferrocenylmethyl)trimethylammonium hydroxide (FMTMA OH) as a template in a one-pot method to produce a chabazite with homogenously distributed Fe species. The original idea for the use of (Ferrocenylmethyl)trimethylammonium hydroxide (FMTMA OH) as a template came from Raul Lobo during a previous Johnson Matthey sponsored project. This thesis details the development work done to find suitable conditions for the synthesis of FMTMA OH, evaluation of calcination conditions on the Fe species in the final material and finally testing of fresh and aged catalysts under standard NH_3-SCR conditions against a benchmark material made using incipient wetness impregnation.

Analysis of the fresh Fe chabazite synthesised with FMTMA OH (Fc-SSZ-13) samples showed they contained homogenously distributed Fe, mainly isolated and dimeric species, regardless of the calcination conditions. Conversely, the fresh benchmark sample contained a wide range of Fe species and significant agglomeration of Fe was seen in these samples. Catalytic testing of the Fc-SSZ-13 showed comparable NO_x conversion to the benchmark sample although, aged samples showed much greater deactivation compared the benchmark. Analysis of the aged samples showed significantly more Fe clusters seen in Fc-SSZ-13 than in the benchmark sample, indicating that sintering of the Fe in Fc-SSZ-13 was much more prevalent.

Table of Contents

List of Abbreviations

ASC	Ammonia slip catalyst
BEA	Beta zeolite topology
BTMA	Benzyltrimethylammonium
CBU	Composite building unit
CHA	Chabazite zeolite topology
Cu-TEPA	Cu-tetraethylenepenamine
DOC	Diesel oxidation catalyst
DON	Dallas-one zeolite topology
DPF	Diesel particulate filter
DR UV-Vis	Diffuse reflectance ultraviolet-visible
EDTA	ethylenediaminetetraacetate
EPR	Electron paramagnetic resonance
FAU	Faujasite zeolite topology
FMTMA	(Ferrocenylmethyl)trimethylammonium
FT-IR	Fourier-transform infrared spectroscopy
GDP	Gross domestic product
GIS	gismondine zeolite topology
H_2-TPR	Hydrogen Temperature Programmed Reduction
HC	Hydrocarbon
HERFD-XANES	High energy resolution fluorescence detected X-ray absorption near edge structure
IZC	Inter zeolite conversion
KFI	Kerr five zeolite topology
MAS	magic angle spinning
MFI	Mobil-type five zeolite topology

MOR	mordenite zeolite topology
OSDA	organic structure directing agent
PM	Particulate matter
pXRD	Powder X-ray diffraction
SAPO-34	Synthetic aluminophosphate thirty four
SBU	Secondary building unit
SCR	Selective catalytic reduction
SDA	Structure directing agent
SEM	Scanning electron microscopy
ssNMR	Solid-state NMR
SSZ-13	Standard oil synthetic zeolite-thirteen
TEA	tetraethylammonium
TGA	Thermo gravimetric analysis
TMAdmA	N,N,N-trimethyl-1-1-adamantammonium
USY	Ultrastable Y
VOC	Volatile organic compound
XANES	X-ray absorption near edge structure
XASLIB	X-Ray Adsorption Library
XPS	X-ray photoelectron spectroscopy
XRD	X-Ray diffraction
XRF	X-ray fluorescence
ZIF-8	Zeolitic Imidazolate Framework-8
ZSM-5	Zeolite Socony Mobil–five

Acknowledgments

I would like to thank my supervisors Dr Alessandro Turrina and Dr Russell Taylor for their support and guidance throughout the project and review of the thesis and, Prof. Raul Lobo and Dr Nicholas McNamara for the initial idea and constructive discussions.

I also extend my gratitude to Dr Veselina Georgieva for catalytic testing, DR UV-Vis measurements, and helpful discussions. Dr Monik Panchal and the Durham X-ray Absorption Facility for XAS measurements. Dr Damian Broens for Mößbauer measurements.

I must also acknowledge the outstanding work done by the following analytical services in Johnson Matthey: solid-state NMR spectroscopy, X-ray photoelectron spectroscopy, porosimetry.

I thank all my colleagues in JMTC zeolites and catalysis research for their support throughout the project.

Johnson Matthey for funding this project.

Finally, all my friends and family for their support.

Chapter 1 . Selective catalytic reduction and zeolite catalysis

1.1 Catalysis

Catalysis plays a major role in almost every aspect of our lives, simply, catalysis is a process of acceleration of a chemical reaction using a substance (catalyst) that is not consumed in the reaction. Catalysis has evolved into two main branches homogenous, a catalyst in the same phase as reactants and heterogenous a catalyst in a different phase as the reactants. This work will focus on heterogeneous catalysis as zeolites are solid and will be applied to the conversion of gasses.

Heterogenous catalysis is incredibly important for the chemical industry. Approximately 80 % of processes in the chemical industry require the use of a catalyst, and catalysis contributes directly or indirectly to around 35 % of global GDP (gross domestic product).[1] The field has grown rapidly since its inception in the 19th century when in 1835 Jöns Jakob Berzelius first coined the term catalysis, coming from the Greek words *kata* meaning down and *lyein* meaning loosen. He described catalysis as "the property of exerting on other bodies an action which is very different from chemical affinity. By means of action, they produce decomposition in bodies, and from new compounds into the composition of which they do not enter".[2] The modern definition of a catalyst states that a catalyst is "a substance that increases the rate of a chemical reaction without itself undergoing any permanent chemical change".[3]

Typically, for a reaction to occur, two molecules need to collide with enough energy (known as activation energy) and, in the correct orientation for the reaction to progress. A catalyst can reduce this activation energy by providing an alternative path for the reaction. Figure 1-1 shows a potential energy diagram for the reaction $A_2 + B_2$ making two molecules of AB. The top path shows the non-catalytic route to AB illustrating the large amount of energy needed for that route. The bottom route shows the alternative catalytic route; this route shows different steps in the catalytic reaction. Initially adsorption of the two components A and B occurs onto the surface of the catalyst. Molecules can adsorb onto the catalyst in two ways, either through physisorption or through chemisorption. In

physisorption processes, molecules are attracted to the surface through Van Der Waals forces. This type of adsorption generally does not affect the electronic state of the molecule. In chemisorption processes, molecules are close enough to the surface of the catalyst so that their electron orbitals overlap which results in the formation of a chemical bond to the catalyst. This orbital overlap and new bond formation stretches and weakens existing bonds in the molecule as electron density is drawn towards the catalyst. This weakening of the bond reduces the activation energy significantly and in some cases can break the bond into isolated atoms. This is a very dynamic process, and these adsorbed molecules move over the surface of the catalyst until they meet another molecule and can form new bonds with that atom or molecule allowing a reaction to occur. Finally, the new product AB desorbs from the surface of the catalyst completing the reaction catalytic route.[4]

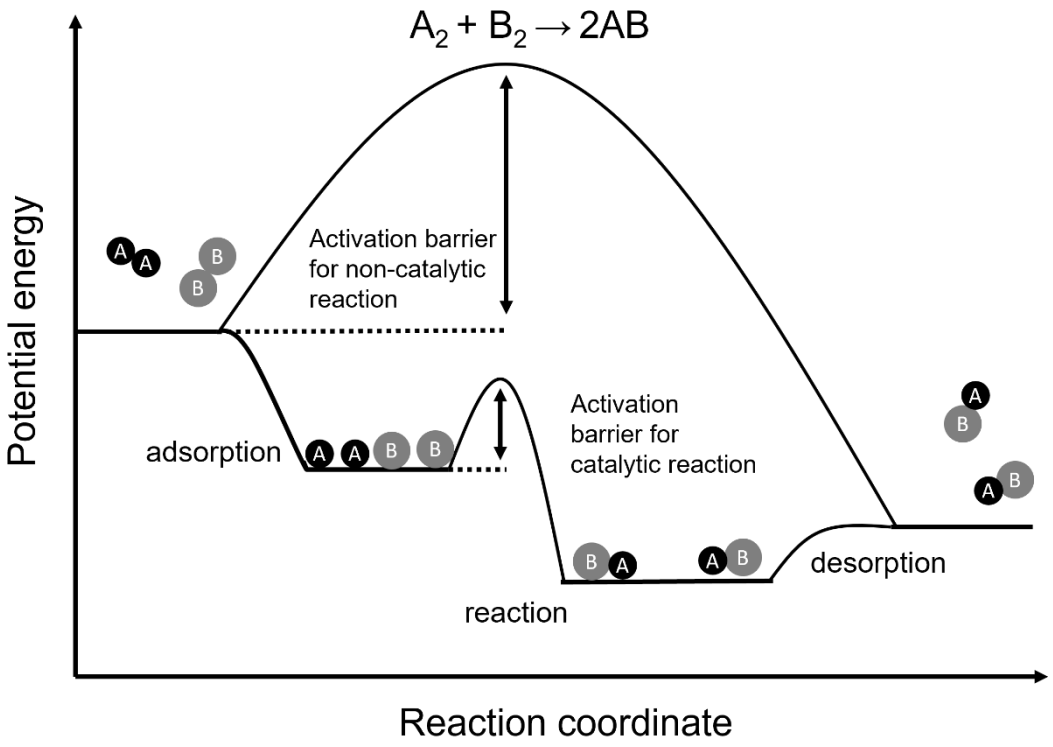

Figure 1-1. Potential energy diagram of a reaction (A_2+B_2→2AB) in catalytic and non-catalytic reactions. Reproduced with permission from ref [4]. Copyright 2017 Wiley-VCH

1.2 NO_x emission reduction

1.2.1 NO_x emission sources

Oxides of nitrogen are typically referred to as NO_x. This term covers a range of nitrogen and oxygen containing molecules. The most abundant NO_x gasses in the air are NO, NO_2 and N_2O however, in terms of air polluting NO_x gasses N_2O is not considered harmful to human health although it may affect the Earth's ozone layer.[5] NO_x gasses are produced in three ways; natural NO_x is formed through lightning strikes due to the extreme temperature during these events. Biogenic NO_x is generated through the nitrification and denitrification process, these processes can be both chemical and biological. However, biological processes with microorganisms are thought to be the major contributor of NO_x emissions from soils.[6] Anthropogenic sources of NO_x (originating from human activity) are typically produced during the combustion of fuels in air, this NO_x typically consists of 95 % NO and 5 % NO_2.[7] The nitrogen and oxygen in air can react during this combustion producing NO_x gasses, these reactions are defined by the Zeldovich mechanism (R 1.1, 1.2).[8] A further contribution to this mechanism was made by Lavoie, Heywood and Keck shown in R 1.3.[9]

$$\mathrm{N_2 + O\cdot \rightleftharpoons NO + N\cdot} \qquad \text{(R 1.1)}$$

$$\mathrm{N\cdot + O_2 \rightleftharpoons NO + O\cdot} \qquad \text{(R 1.2)}$$

$$\mathrm{N\cdot + OH\cdot \rightleftharpoons NO + H\cdot} \qquad \text{(R 1.3)}$$

1.2.2 Impact of NO_x emissions

NO_x gasses are harmful to human health and the environment. There is evidence suggesting that NO_2 exposure can affect the respiratory and cardiovascular systems and can lead to diabetes, poorer birth outcomes, premature mortality and cancer.[10] NO_x gasses affect the environment through the production of acid rain and ozone. NO_2 reacts with water in the air to produce nitric acid (R1.4) which is a component of acid rain that travels through global ecosystems causing major damages. When acid rain is deposited onto the soil and causes soil acidification this can negatively affect plant life and consequently other organisms and

animals in that ecosystem. Likewise, when acid rain makes its way to freshwater bodies it causes damage to the aquatic ecosystem harming fish and other aquatic animals. Finally, when acid rain makes its way into the ocean its causes ocean acidification harming coral reefs and causing harm to algal blooms.

$$2NO_2 + H_2O \longrightarrow HNO_3 + HNO_2 \qquad (R.\,1.4)$$

NO_x emissions also contribute to tropospheric ozone production, which can contribute to chronic respiratory diseases such as asthma and can damage lungs.[11] Ozone is produced through a series of reactions (R 1.5-1.10) when volatile organic compounds (VOC) and NO_x react in the presence of sunlight.[12]

$$VOC + OH \xrightarrow{[O_2]} RO_2 + H_2O \qquad (R\,1.5)$$

$$CO + OH \xrightarrow{[O_2]} HO_2 + CO_2 \qquad (R\,1.6)$$

$$RO_2 + NO \xrightarrow{[O_2]} \text{secondary VOC} + HO_2 + NO_2 \qquad (R\,1.7)$$

$$HO_2 + NO \rightarrow OH + NO_2 \qquad (R\,1.8)$$

$$NO_2 + h\upsilon \rightarrow NO + O\cdot \qquad (R\,1.9)$$

$$O\cdot + O_2 + M \rightarrow O_3 + M \qquad (R\,1.10)$$

Mobile sources of NO_x emissions account for around 50 % of all NO_x emissions, electric power plants make up around 20 % while natural and biogenic make up around 30 %.[13] Considering two major hydrocarbon (HC) road transportation fuels used, diesel cars emit around 10 times more NO_X than gasoline cars and more particulate matter (PM) under real world driving conditions as they operate at higher temperatures.[14] Molecular atmospheric nitrogen combines with fuel under fuel-rich conditions of a diesel engine. The fuel combusts and the nitrogen is oxidised to NO_x under these conditions. Mobile NO_x emissions can be reduced using catalysis. Typically, a three-way catalyst is used for gasoline engines (an emissions control catalyst that converts HC, CO and NO_x into less harmful gases) however, these cannot be used for diesel engines due to the high oxygen content. Selective catalytic reduction is the leading method to reduce NO_X emissions from diesel engines.

Governments around the world brought in legislation to limit emissions from vehicles. The European Union first brought in the legislation in 1992 and have regularly introduced new regulations with stricter limits. Table 1.1 and 1.2 show the emission limits over the years for passenger diesel and heavy-duty diesel engines.[15]

Table 1-1. Emission limits for passenger cars with diesel engines[15]

	Emission limits g/km					
Pollutant	Euro I	Euro II	Euro III	Euro IV	Euro V	Euro VI
	1992	1996	2000	2005	2009	2014
CO	3.16	1.00	0.66	0.50	0.50	0.50
NO_x	-	-	0.50	0.25	0.18	0.08
HC + NOx	1.13	0.70	0.56	0.30	0.23	0.17
PM	0.14	0.08	0.05	0.025	0.0045	0.0045

Table 1-2. Emission limits for heavy-duty diesel engines[16]

	Emission limits g/kWh							
Pollutant	Euro I	Euro I	Euro II	Euro II	Euro III	Euro IV	Euro	Euro
	1992	1992	1995	1997	2000	2005	V	VI
	< 85 kW	> 85 kW					2008	2012
CO	4.5	4.5	4.0	4.0	2.1	1.5	1.5	1.5
NO_x	8.0	8.0	7.0	7.0	5.0	3.5	2.0	0.46
HC	1.1	1.1	1.1	1.1	0.66	0.46	0.46	0.16
PM	0.61	0.36	0.25	0.15	0.1	0.02	0.02	0.01

1.2.3 Selective catalytic reduction

Selective catalytic reduction (SCR) is a process for the chemical reduction of NO_x to N_2 and H_2O with the aid of a catalyst and a reductant. Typically, the reductant is added to the exit gas, where it reacts in the presence of a catalyst. The process can be used for both stationary and mobile sources of NO_x. It was first reported in 1958 by Endter[17] and first implemented for power plants in Japan in the 1970's.[18] The first mobile SCR systems were installed in 1989 on marine engines[19] and then implemented in the mid 2000's to meet the Euro IV and Euro

V emission standards (see Table 1-2).[20] A typical schematic of a vehicle SCR system is shown in Figure 1-2.

Each manufacturer may arrange their system differently however they will all contain the four main processes: diesel oxidation catalyst (DOC), diesel particulate filter (DPF), selective catalytic reduction (SCR) and an ammonia slip catalyst (ASC).

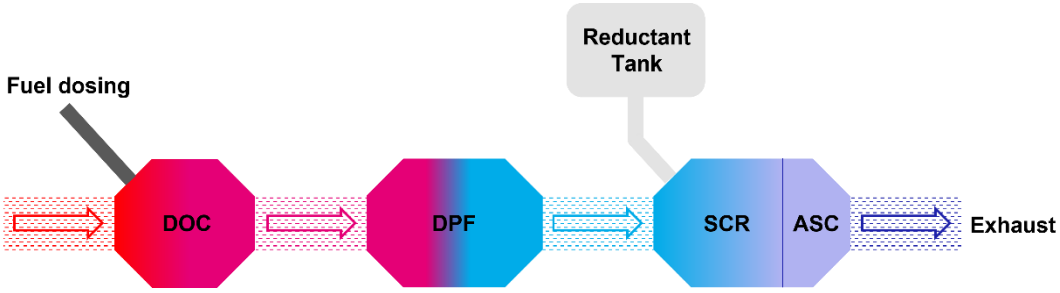

Figure 1-2. Schematic of a typical SCR exhaust system

The diesel oxidation catalyst will oxidise any un-combusted hydrocarbons, CO and NO coming from the engine. The DOC typically comprises of a noble metal catalyst such as platinum or palladium, it is usually positioned upstream of the exhaust system to increase the NO_2/NO_x ratio.[21] This higher ratio will increase the low temperature soot oxidation rate in the DPF and it will improve NO_x conversion in the SCR unit.[22] The main role of the DPF is to remove particulate matter produced during diesel combustion. It can be made from alumina coated wire mesh, ceramic fibre, porous ceramic monoliths; current DPF's use honeycomb ceramic monoliths.[23] There has been research aiming at combining the DOC and DPF processes by using noble metal coated DPF's.[24] This approach has benefits of reducing the size of the exhaust treatment system, however as both process require different regeneration conditions it is technically difficult. SCR is usually placed towards the end of the emission control system, its role is to reduce NO_x emissions. NO decomposition is relatively simple and thermodynamically favoured at low temperatures, however the reaction is kinetically limited and sufficiently active catalysts have not yet been found,[7] therefore a reducing agent is required to convert NO to N_2. CO and hydrocarbons can be used, however this requires fuel to be introduced to the catalyst reducing fuel efficiency. Ammonia has widely been used for stationary SCR applications although urea is preferred for mobile SCR systems.[25] Urea is used as it can decompose, either thermally or catalytically, to produce ammonia (R 1.11), which is then used as the reductant for the process.

$$NH_2CONH_2 + H_2O \rightarrow 2NH_3 + CO_2 \quad (R\ 1.11)$$

The ammonia produced by the decomposition of urea reacts with NO in the presence of oxygen from the air to produce N_2 and water (reaction 1.12).[26, 27]

$$4NO + 4NH_3 + O_2 \rightarrow 4N_2 + 6H_2O \quad (R\ 1.12)$$

When NO_2 is precent in the feed, an equimolar NO-NO_2 reaction occurs (Reaction 1.13). This reaction is known as fast SCR as it is considerably faster than the standard SCR reaction (Reaction 1.12).[27, 28]

$$NO + NO_2 + 2NH_3 \rightarrow 2N_2 + 3H_2O \quad (R\ 1.13)$$

This fast SCR reaction has been vital to meet the emission regulations and has benefited from the conversion of NO to NO_2 in the DOC. If the ratio of NO_2/NO is larger than 1 the reaction can progress through alternative routes (Reaction 1.14 and 1.15).[28]

$$2NO_2 + 2NH_3 \rightarrow N_2 + N_2O + 3H_2O \quad (R\ 1.14)$$

$$3NO_2 + 4NH_3 \rightarrow 3.5N_2 + 6H_2O \quad (R\ 1.15)$$

First generation mobile SCR systems used WO_3 and V_2O_5 supported on TiO_2 honeycomb monoliths. As more stringent NO_x legislation was implemented, research moved away from V_2O_5 and WO_3. This was due to the requirement of catalysts to remain active at higher temperatures, vanadium's toxicity and its high activity for the oxidation of SO_2 to SO_3. Researchers focused on alternatives such as metal modified zeolites for NH_3-SCR reactions due to their stability at higher temperatures, isolated active sites and their activity over a broad temperature range.[29] ASC systems are typically located at the end of the exhaust system, their primary aim is to convert residual ammonia that is not consumed during the SCR process to N_2 and H_2O (R1.16), modern ASC systems can also convert NO_x to N_2.[30]

$$4NH_3 + 3O_2 \rightarrow 2N_2 + 6H_2O \quad (R\ 1.16)$$

1.3 Zeolites

1.3.1 A history of zeolites

The first zeolite publications originate from the 18th century, which outlined the initial discovery of the material class. The term zeolite was first used by the Swedish mineralogist Axel Fredrik Cronstedt who, upon heating certain minerals, observed the evolution of steam. This led him to name these minerals zeolites, originating from the Greek words zein (ζέω), to

boil, and lithos (λιθος), stone.[31] In the subsequent years there were several other observations, which used the zeolite term. Ignaz von Born used the term in 1772 to describe cubic crystals discovered in Iceland. These crystals would later be defined as zeolite en cube in 1783 by Jean-Baptiste Louis de Romé l'Isle and chabasie in 1788 by Louis Augustin Guillaume Bosc d'Antic, now called chabazite. It was almost 100 years after Cronstedt's first observation for the first direct investigation of zeolites.[32] Later in the XIX century scientists began to explore the materials properties. These very initial exploration of zeolite properties focused on the reversible adsorption phenomenon of zeolites. A. Damour showed in 1856 reversible water adsorption in several natural zeolites and showed that the adsorption did not have an effect on the morphology of the material.[33] It was not until the 20th century when zeolite science began its rapid growth with many research articles and patents being published during this period (Figure 1-3). This was initiated by the development of characterisation techniques, allowing scientists to better understand the structure of these materials. R M Barrer was one of the first people to realise the potential of zeolites and is known as one of the pioneers in the zeolite field. Barrer was the first to report the preparation of zeolites P and Q by high temperature and pressure synthesis,[34-36] these zeolites were later found to have the zeolite Kerr five (KFI) framework topology[37] which has no known natural counterpart. This period also saw rapid industrialisation of zeolites with the filing of many patents, and development of zeolite-based industrial processes. Union Carbide first commercialised zeolites for separation and purification processes and later sold zeolite Y as a catalyst for isomerisation. Mobil Oil later took over Union Carbide with their use of zeolite X for hydrocarbon cracking and Zeolite Socony Mobil–five (ZSM 5) for a range of acid catalysed reactions.[38] Zeolite science continued to grow all the way to the 21st century, primarily in the area of catalysis; currently, there are 265 structures deposited into the zeolite database.[39]

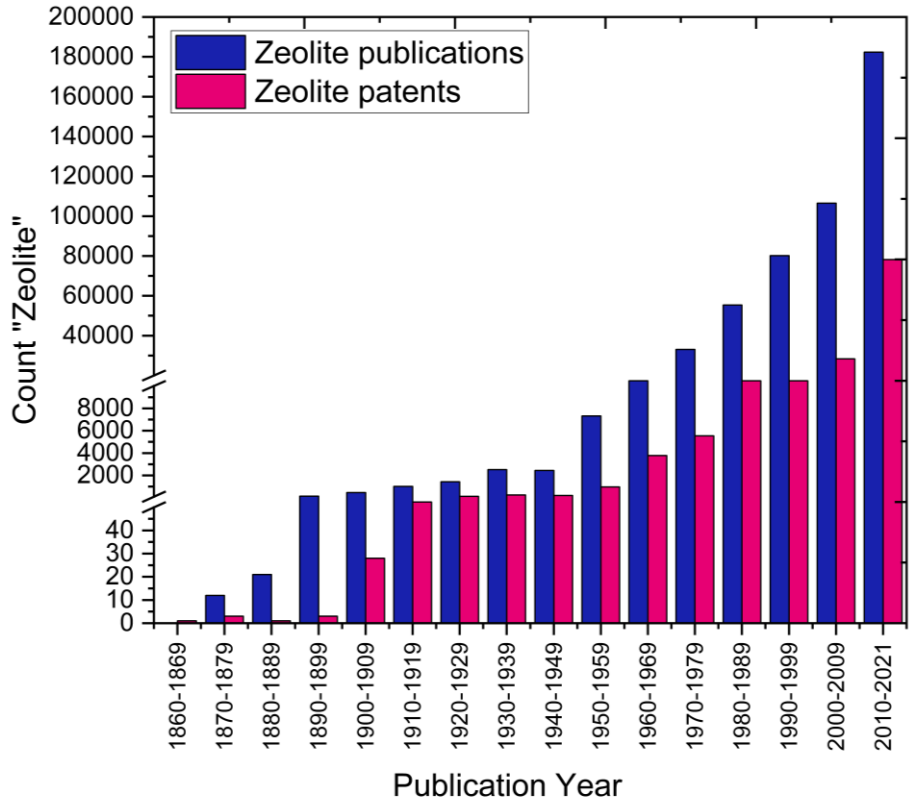

Figure 1-3. Number of publications and patents per year. Produced using Scifinder^{n} using the search term "Zeolite"

1.3.2 Zeolite composition, structure, and properties

Zeolites are a class of microporous materials, they typically consist of silicon, aluminium, and oxygen, these atoms form TO_4 tetrahedral units where T is either Si or Al. These units link together though Si-O-Si and Si-O-Al linkages, Al-O-Al linkages are energetically unstable and therefore forbidden, this is known as the Lowenstein rule.[40] The overall charge of the network is unbalanced as silicon is present in its +4 oxidation state and Al is present in its +3 oxidation state, which results in a negative charge associated with AlO_4 tetrahedra in the framework. This negative charge is counterbalanced by a cation (e.g. a proton or metal cation) stabilising the whole structure. Eq 1.01 shows the general formula for a zeolite where M is a cation counterbalancing the negatively charged framework.

$$M_{2/n}O \,.\, (AlO_2)_x \,.\, (SiO_2)_y \,.\, zH_2O \qquad \text{(Eq. 1.01)}$$

The three-dimensional pore and channel network forms from the starting TO_4 units, also known as primary building units. These units link together via the oxygen linkages to from ring structures known as secondary building units (SBU). These in turn form more complex three-dimensional cage structures known as composite building units (CBU). These CBUs arrange themselves into the final zeolite structure, the same CBU can form different zeolite frameworks depending on the arrangement. Figure 1-4 shows a schematic representation of the formation of the zeolite structure. Zeolites are often classified by their aluminium content, either by SiO_2/Al_2O_3 ratio (SAR) or Si/Al ratio. SAR is typically used when preparing catalysts while Si/Al is used when describing acid site densities, Si/Al is approximately half the value of SAR. Low Si/Al zeolites range between 1-2, medium Si/Al zeolites range between 3-10 and high Si/Al zeolite range from 10-∞.[41]

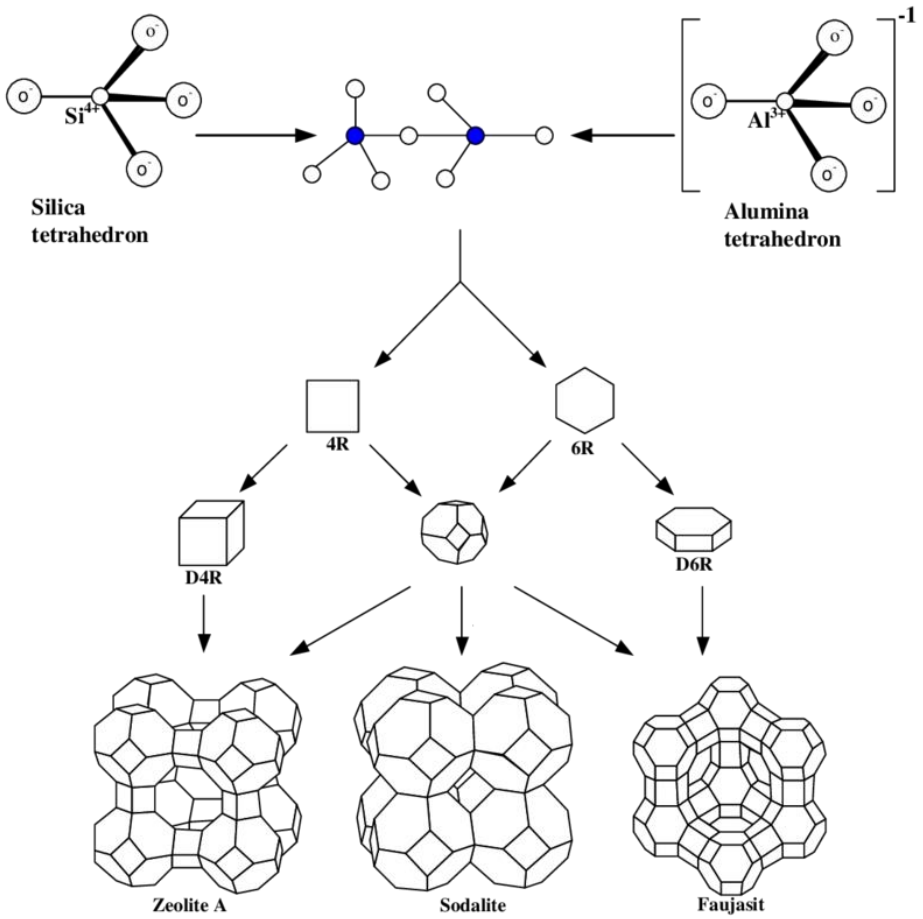

Figure 1-4. Schematic representation of zeolite formation from tetrahedral primary building units, secondary building units and to the final zeolite framework Reprinted with permission from ref [42]. Copyright 2013 by Authors, Published by BCREC Group

Figure 1-4 shows some of the more common framework structures and the composite building units that organise into zeolites final structure. Each zeolite framework is given a unique three letter code, these code are assigned by the International Zeolite Association following the International Union of Pure and Applied Chemistry rules for zeolite nomenclature.[39] Natural zeolites are typically named after the mineral in which they were discovered while synthetic zeolites are typically named by the discoverers. In some case the natural zeolite and synthetic zeolite will have the same framework structure, for example Standard Oil synthetic zeolite-13 (SSZ-13) has the same CHA framework as chabazite and the names are often used interchangeably. The same CHA framework can also be found in other non-zeolite materials such as silicoaluminophosphate thirty-four (SAPO-34) and zeolitic imidazolate framework-8 (ZIF-8).

Table 1-3. Composite building units (CBUs) present in different framework structures[39]

Framework type-code	FAU	*BEA	LEV	MAZ	CHA	GIS	LTL	MOR	FER	MFI
Framework structure	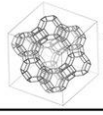									
Composite building unit	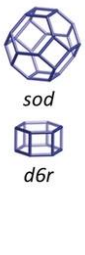						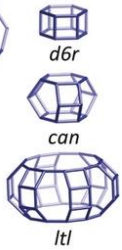			

An important property of zeolites is their ability to exchange ions within its structure. This property arises due to a charge imbalance in the TO_4 network, when a silicon atom with a +4 charge is replaced with an aluminium atom with a +3 charge, a net negative charge is introduced into the framework. This negative charge is counterbalanced by a cation such as H^+, Na^+, K^+, etc. and it is held in place in the zeolite structure. If the negative charge is counterbalanced by a proton, a strong Brønsted acid site is formed (Figure 1-5) and the site can participate in catalytic reactions such as fluid catalytic cracking.[43]

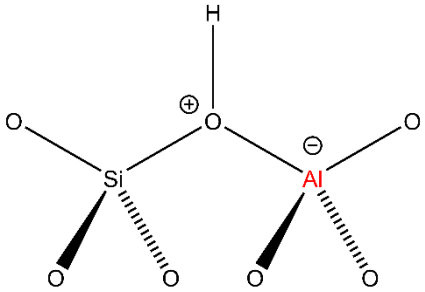

Figure 1-5. Examples of a Brønsted acid site in a zeolite framework

Brønsted acid sites are formed in zeolites when a proton bonds directly to a bridging oxygen atom as shown in Figure *1-5*. It is considered that all bonds; O-Si, O-Al and O-H are all strong covalent bonds with additional contributions from small electrostatic interactions.[44-46] The oxygen atom in the Brønsted environment can be compared to a hydronium cation H_3O^+. While bond angles in the H_3O^+ cation are similar around 120°, the preferred angle in Al-O(H)-Si would ordinarily be slightly narrower in the deprotonated state however this is prevent by the long range order of the zeolite crystal.[47]

Substituting Al^{3+} ions with other trivalent ions in the TO_4 zeolite network has shown to change the acidity of the zeolite.[48] This has method has been used successfully used to tune the acidity of zeolites and has shown promise in reactions where strong acidity may promote side reactions such as in propane dehydrogenation,[49] methanol to aromatics[50] and in biomass conversion reactions.[51-53] The trend in acidity for widely used trivalent atoms are as follows Al > Ga > Fe > B this trend has been shown experimentally.[48, 54, 55] The fundamental reason for this trend is still not fully understood many theories have been proposed from electronegativity,[56, 57] electrostatic potential,[58] polarisability[59] and deprotonation energy.[47, 60, 61]

Lewis acid sites can also form in zeolites, these can be either framework or extraframework Lewis acid sites. Framework sites are formed by substituting tetravalent cations such as Ti^{4+}, Sn^{4+} or Zn^{4+} into the structure as seen in Figure 1-6 (A). Extraframework sites typically form by ion-exchange this can fix and stabilise an active metal cation species as shown in Figure 1-6 (B).

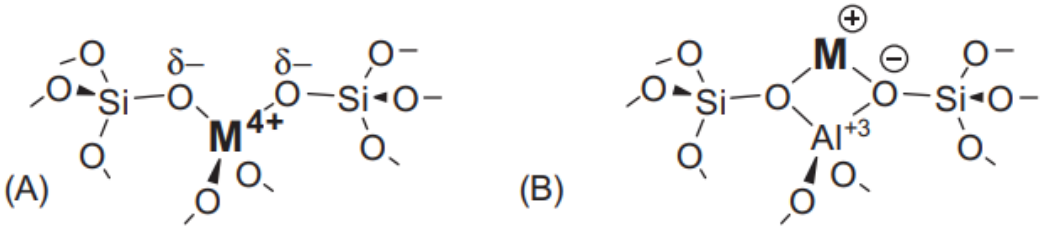

Figure 1-6. Framework (A) and extraframework (B) Lewis acid sites in zeolites. Reproduced with permission from ref [62]. Copyright 2018 Elsevier

Shape selectivity is also an important property of zeolites as it can control product distribution in reactions, favouring desired products and reducing unwanted side products. Shape selectivity arises from the pore and the channel network of the zeolite it is characterised by three primary mechanisms.[63-66]

i) Reactant shape selectivity, whereby molecules are discriminated by their size and shape to enter the zeolite pore.

ii) Product shape selectivity, whereby bulky molecules are sterically hindered from leaving the zeolite.

iii) Transition state selectivity whereby the formation of molecular transitions states is restricted by the confines of the zeolite channels, intersections or cages.

1.3.3 Zeolite synthesis

Zeolites can be formed by different methods; natural zeolites are formed during geological processes, under very high temperatures, pressures and extremely long timeframes. Most synthetic zeolites are synthesised hydrothermally,[67, 68] this method was first established by Barrer and Milton in the 1940s.[34, 35] In this method zeolites are typically synthesised via sol-gel process, where a source of T atoms, a structure directing agent (SDA), a mineralising agent, and a solvent are required; in certain preparations zeolite seeds crystals may also be used. Generally, aluminium and silicon containing precursors are used as a source of T atoms in the synthesis.

Typically, sodium silicate, colloidal silica, fumed silica, or volcanic ash can be used as the silica T atom precursors, while aluminium salts or oxides can be used at the aluminium source of T atoms for aluminosilicate zeolites.

SDA's can be divided into: i) inorganic cations, such as K^+ or ii) organic templates, generally containing a quaternary ammonium ion. Templates direct the structure of the zeolite by occupying space in the pore structure of the zeolite preventing the structure from collapsing. The choice of template will influence the final structure of the zeolite.

Hydroxide is the most common mineralising agent for aluminosilicate zeolites. Fluoride can also be used as a mineralising agent and for these synthesis fluoride salts and acids are used. The primary purpose of the mineralising agent is to dissolve the aluminium and silicon source in the reaction mixture.

Water is typically used as the solvent in the synthesis as the reagents are soluble in water and it is the preferred solvent for large scale production as it is nontoxic and cheap.

A typical hydrothermal synthesis proceeds via the following steps[69], a schematic of the process can be seen in Figure 1-7.

1. Reactants; T atom source, template, mineralising agent, and solvent are first mixed to produce a homogenous gel.

2. The resulting gel is heated in a sealed autoclave to temperature above 100 °C.

3. After an induction period, crystalline products start to form.

4. Gradually, the starting reagents are converted into the crystalline zeolite product. These can then be collected by filtration.

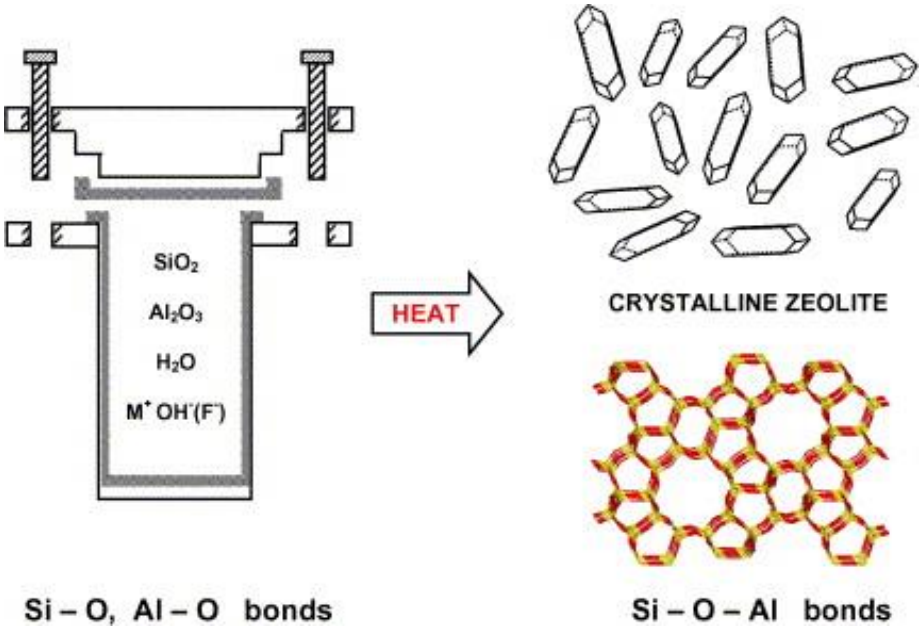

Figure 1-7. Schematic for the hydrothermal synthesis of zeolites. Reproduced with permission from ref [69]. Copyright 2018 Elsevier

The mechanism of zeolite formation is very complex, with many chemical reactions along with equilibrium and solvation processes occurring during the synthesis. In the simplest terms, the mechanism can be described as a nucleation growth process. Crystal nuclei start to form from the amorphous gel mixture, these nuclei continue to grow following the classic s-shaped growth curve (Figure 1-8) into the crystalline phase.[70] Zeolites are thermodynamically metastable phases therefore producing a zeolite with the desired crystal phase is difficult as the reaction needs to be kinetically controlled. This is typically done by altering variables such as temperature, crystallisation time and gel composition.

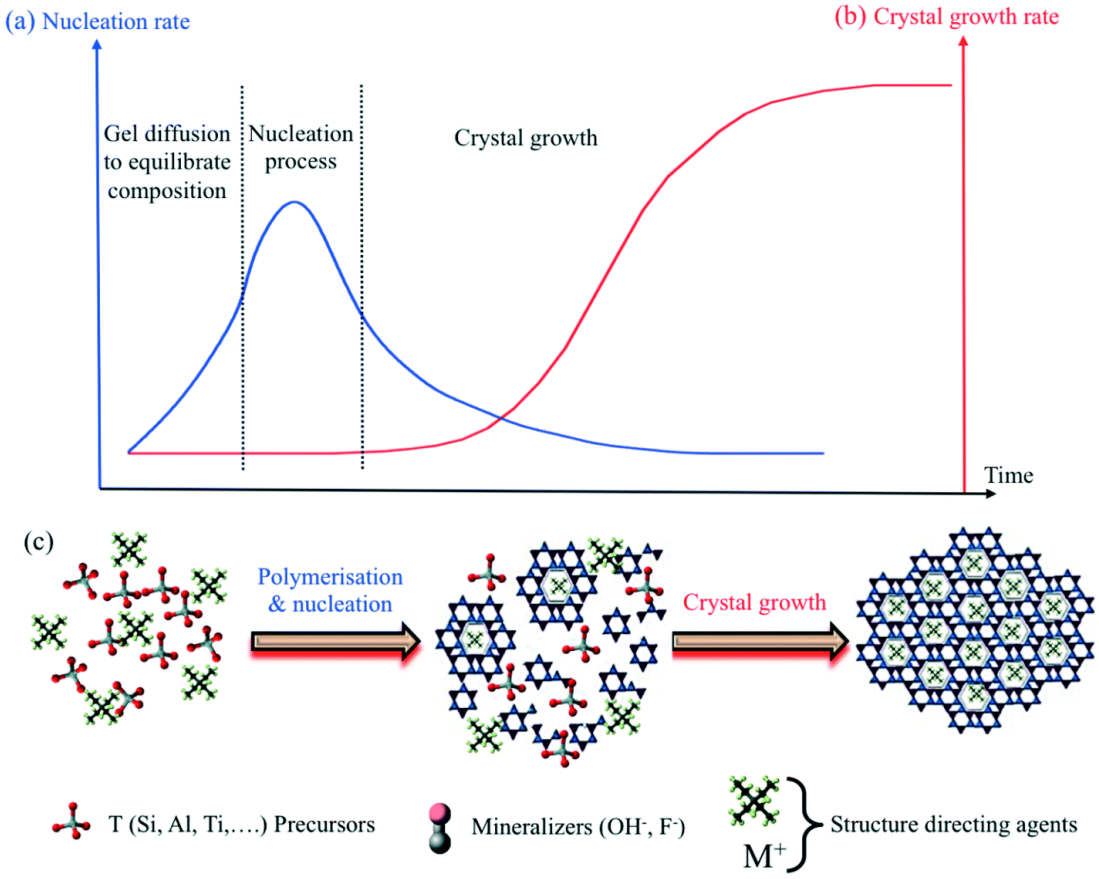

Figure 1-8. Schematic for the nucleation and growth process of zeolite synthesis. Reproduced with permission from ref [70]. Copyright 2016 Royal society of chemistry

The freshly synthesised zeolite also known as the as-made zeolite requires further processing for most catalytic applications. The as-made zeolite may still contain organic templating agent or alkali cations within the structure. Organic templates are typically removed by air calcination; this process oxidises the template to gaseous products so it can be removed from the zeolite. Cations are removed by ion exchange, generally the proton form of the zeolite is required for catalysis. The proton form is produced by ion-exchanging with an ammonium salt such as ammonium hydroxide and then heating to remove ammonia and leave a proton. Ion exchange in zeolites is an equilibrium and diffusion limited process therefore multiple ion exchanges may be required to fully ion exchange the zeolite.

1.4 Synthetic Chabazite (SSZ-13)

The zeolite framework has been shown to influence NH_3-SCR performance, large pore zeolites such as beta zeolite (BEA) have been shown to produce more N_2O than medium and small pore zeolite such as MFI or CHA.[71-73] The trend is reported to be caused by susceptibility of large pore zeolites to accumulated ammonium nitrate within their structures, blocking channels and inhibiting SCR reactions.[74-76] Ammonium nitrate then undergoes thermal decomposition into N_2O and thus accounts for the trend. As emissions regulation has focused on lowering NO_x generally more work has focused on small pore zeolites with much of the attention on SSZ-13.[16]

Standard Oil Synthetic Zeolite-13 known as SSZ-13 was first synthesised by Stacey I. Zones in 1983.[77] SSZ-13 has the chabazite (CHA) framework structure which consists of *cha* cages which are linked together with double six-ring (d6r) forming a 3-dimensional network with a pore diameter of 0.37 nm and *cha* cage windows of 0.74 nm as demonstrated in Figure 1-9.[78] The large cavity coupled with small windows can prevent sintering in SSZ-13 and favour the stabilisation of extra-framework active metal species. This, as well as the hydrothermal stability of CHA ,makes SSZ-13 a good candidate for the SCR reaction.[79, 80]

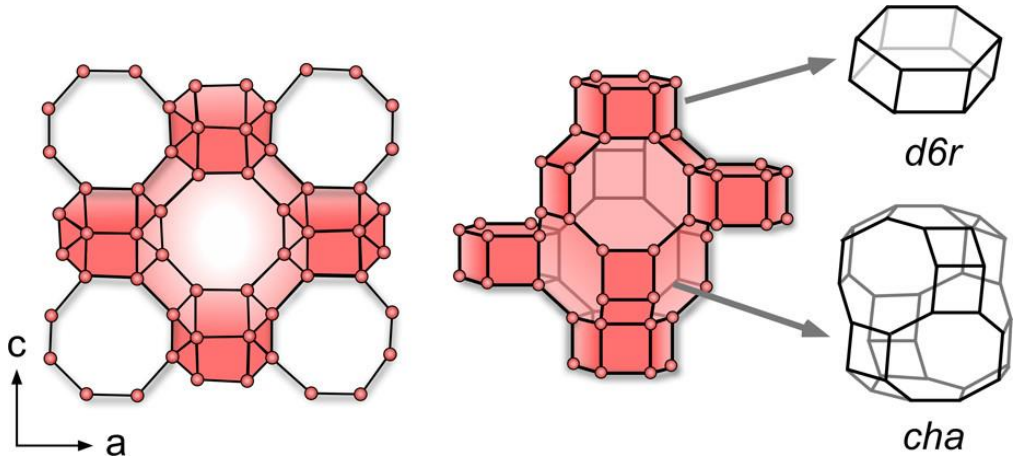

Figure 1-9. Structure of SSZ-13 with showing the *cha* cages and d6r building units. Reprinted with permission from ref [78]. Copyright 2015 American Chemical Society

While SSZ-13 can be made organic-free with a Si/Al ratio between 2 and 4 in hydroxide media[81] there was little use for these low Si/Al materials. The use of SSZ-13 increased rapidly after Zones demonstrated the synthesis of SSZ-13 with higher Si/Al ratios using N,N,N-trimethyl-1-1-adamantammonium (TMAdmA) as an OSDA.[77, 82] The synthesis has since been adapted to produce various Si/Al ratios and the amount of OSDA used has been reduced to

improve economics.[83] Several alternative OSDAs have also been used to synthesize SSZ-13 such as benzyltrimethylammonium (BTMA),[84, 85] tetraethylammonium (TEAOH),[86] choline chloride, [87, 88], mesoporogen,[89] Cu-tetraethylenepenamine (Cu-TEPA),[90-92] and N,N,N-dimethylethylcyclohexylammonium bromide.[93] Examples of the structures can be seen in Figure 1-10.

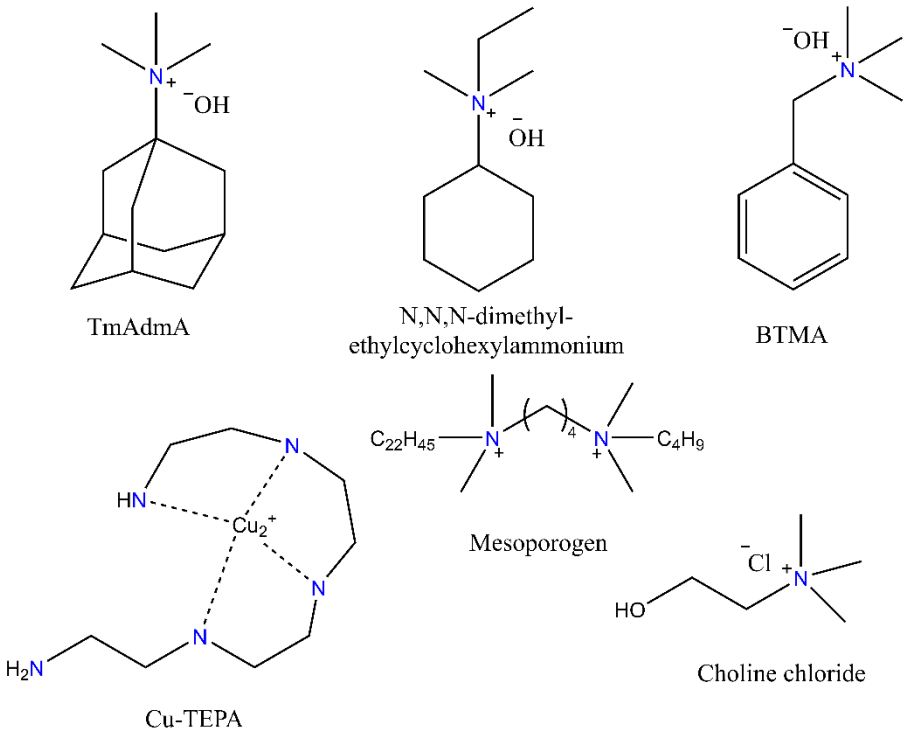

Figure 1-10 Examples of OSDAs for SSZ-13. BTMA (N,N,N-trimethylbenzylammonium), TEPA (tetraethylenepentamine)

Instead of synthesising SSZ-13 directly from Al and Si precursors, inter zeolite conversion (IZC) has been shown to be a successful method to produce SSZ-13.[81, 85, 86, 94-99] Faujasite (FAU) zeolites have been used for this conversion and it is said the structural similarity between FAU and CHA frameworks can assist in the construction of SSZ-13.[100] However, multiple other zeolites without d6r units have also been used to make CHA.[96, 99, 101, 102] IZC is a useful method and can improve the economics of the SSZ-13 if the starting zeolite is low cost.

1.4.1 Metal modified zeolites

Zeolite make excellent catalysts as they are able stabilise isolated metal atoms within their structure. This is due to their well-ordered structure of pores, channels and cavities as well as their ion-exchange properties. Metal atoms can be introduced into the zeolite structure in three different locations. These are defined as: i) isolated metal clusters, ii) ion exchanged cations stabilized on the $[AlO_4]^-$ site, and iii) single atoms substituted into the framework of the zeolite (Figure 1-11).[103]

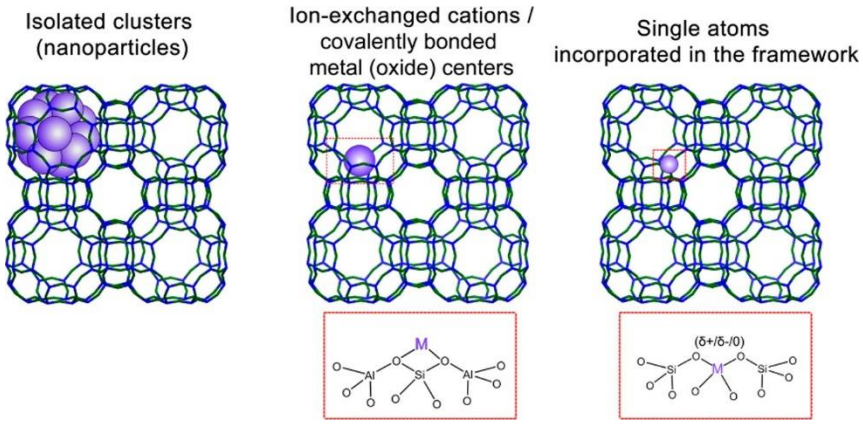

Figure 1-11. Potential metal atom locations in zeolite framework. Reproduced with permission from ref[103]. Copyright 2018 American Chemical Society

The previous section already explained how different framework T atoms can change the Brønsted acidity in a zeolites and how metal cations can induce Lewis acidity in zeolites. In particular, Cu and Fe ion-exchanged zeolites are extensively used in NH_3-SCR, these zeolites are generally considered to be redox catalysts however they form Lewis acid – base pairs. These pairs comprise of an electropositive cation typically a metal centre and an electronegative component commonly a basic framework oxygen. These Lewis acid base pairs act cooperatively to stabilise unstable species within the zeolite.[62] These sites can be present in a wide range of species including isolated metal cations, complexed mono and di-nuclear cationic species, oligomeric species, and bulk oxides. The formation of these species is dependent on the chemical composition of the zeolite, chemistry of the metal ions, material preparation and the catalyst activation procedure.

These modified zeolites are used in many current catalytic applications such as in oil processing,[104-106] natural gas processing,[107, 108] biomass conversion,[109] environmental applications[110-113] and for various chemical synthesis reactions.[114-116]

1.5 Iron zeolites

Iron zeolites typically refer to zeolites with framework iron where Al atoms in the zeolite framework have been replaced with Fe atoms. In the context of this work iron zeolites will also refer to extraframework iron zeolites where iron cations replace alkali cations to maintain the charge balance in the zeolite. Iron zeolites have been studied for many years, in the early years zeolites were mainly used to remove Fe from waste streams.[117] There was a stark increase in the number of publications in the 1950's this is in line with the general interest in zeolites during that period. The specific interest in framework iron zeolites came upon the realisation that Brønsted acidity could be tuned by replacing Al atoms with other trivalent atoms.[48] More recently extraframework iron zeolites have been attracted increased attention due to their use catalysis (Figure 1-12). Iron zeolites have mainly been used in oxidation catalysis for instance, the conversion of benzene to phenol,[118] phenol hydroxylation,[119] oxidation of VOCs, [120] selective partial oxidation.[121-124]. One of the major areas of interest for iron zeolites is hydrocarbon or ammonia selective catalytic reduction of NO_x.[27, 125-128] Fe zeolites offer advantages over bulk metal catalysts for these reactions as the unique properties of zeolites such as shape and selectivity and zeolite's ability to stabilise isolated active metal centres results in higher catalytic activity vs bulk metal catalyst. The major challenge of Fe-Zeolites is in their preparation, Fe is very reactive and synthesising zeolites with homogenously distributed isolated extraframework Fe sites is very difficult as the Fe often reacts to form other species.

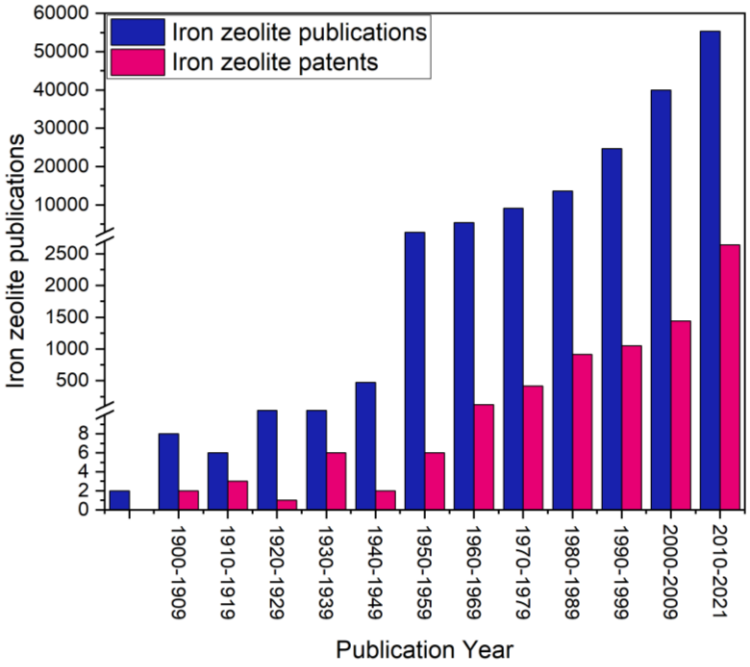

Figure 1-12. Number of publications and patents per year. Produced using Scifinder^{n} using the search term "Iron zeolite"

1.5.1 Nature of iron in zeolite catalysts

Understanding the nature of iron in zeolites is very complex and has been debated for many years.[129, 130] This has largely been due to recognising the many different forms of iron that can exist in the zeolite and the difficulty synthesising zeolites with only one iron species. Iron can be present in the zeolite as framework or extra-framework components, these are shown in Figure 1-13. Framework iron (a) replaces Al^{3+} ions with Fe^{3+} ions in the structure[131] while extra framework iron can sit anywhere in the structure. Isolated ionic extra-framework iron (b), typically Fe^{3+} or Fe^{2+} replaces alkali cations that counterbalance the zeolite structure,[128] they are typically located within the cavities of the zeolite. Dimeric iron species (c) or oligemic species such as α-Fe_2O_3 or Fe_3O_4 can be present within the zeolite (d), on the surface of the zeolite (e) or between zeolite crystals (f).[132]

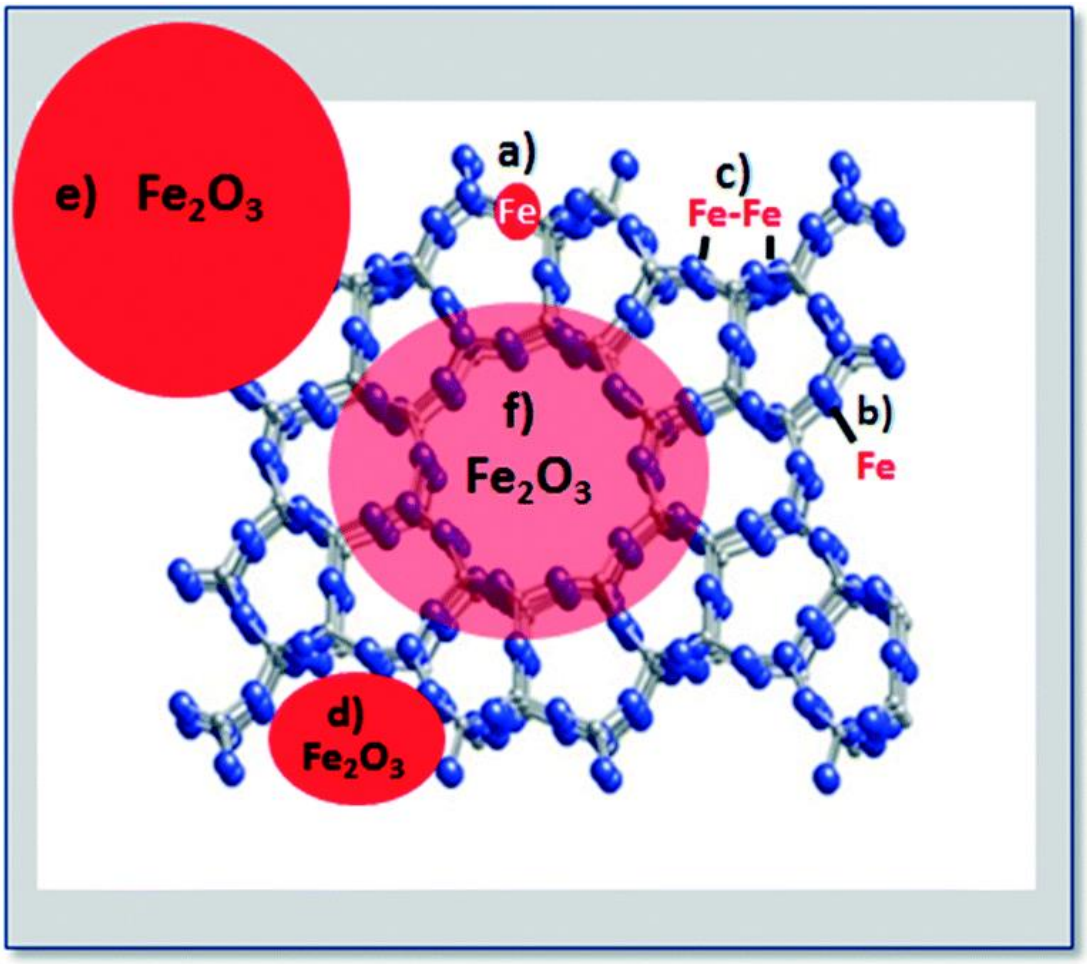

Figure 1-13. Schematic representation of different Fe species in a zeolite. Reprinted with permission from ref[133]. Copyright 2016 Royal society of chemistry

1.5.2 Synthesis of iron zeolites

Several methods have been developed to incorporate iron into zeolites. The method of introduction will affect the oxidation state, nuclearity and location of the iron sites and therefore will influence the performance of the catalyst. Examples of common iron incorporation methods are outline below.

Ion exchange with Fe^{3+} and Fe^{2+} salts

Ion exchange is readily used in the preparation of extra-framework metal-doped zeolite catalysts (Figure 1-14). The procedure exchanges metal ions within structure of the zeolite by replacing charge balancing cations that are already present, producing a material with

highly dispersed metal particles. The method for ion exchange requires the dissolution of a metal precursor salt such as $FeCl_2$, $FeCl_3$, $FeSO_4$ or $FeNO_3$, typically in water, although other solvents can be used.[134, 135] The solution is mixed with the zeolite powder and left to equilibrate. The material is then filtered, washed, dried, and finally calcined to produce the final material.[110, 128, 136-138] This method should selectively target extraframework positions, however Fe chemistry in solution can affect the process, and can lead to the formation of large bulky Fe species (e.g. FeOOH) that may not be able to diffuse into the zeolite.[127]

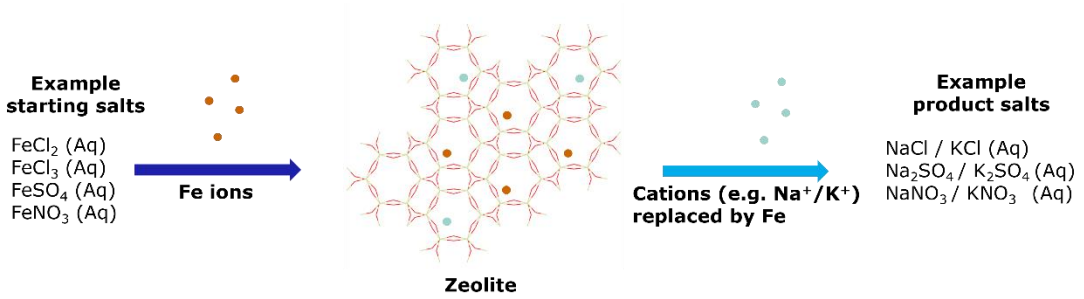

Figure 1-14. Schematic of Ion exchange process

Incipient wetness impregnation

Incipient wetness impregnation is widely used for the synthesis of heterogenous catalysts (Figure *1-15*). The method is simple, low cost and generates very little waste. Similarly, to ion-exchange, the method requires the dissolution of a metal salt, however in this case the volume of solution is equal to the pore volume of the parent material. The solution enters the parent material through capillary action, dispersing the metal throughout the material. The material is then dried and then activated by calcination or reduction to yield the final active zeolite catalyst.[139-141] This method generally produces a heterogeneously distributed material as practically it is difficult ensure all the Fe is located withing the zeolite structure and is present as isolated species.

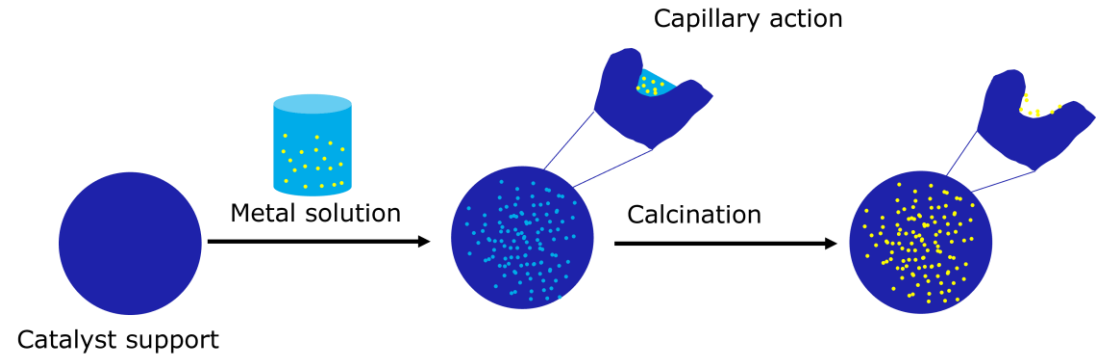

Figure 1-15. Schematic of incipient wetness impregnation

One-pot introduction methods

The one-pot introduction method introduces the metal during the synthesis of the zeolite (Figure 1-16). The metal is typically introduced to the zeolite gel as a metal salt and is present as the zeolite crystallises. This method can incorporate the metal in both framework and extra-framework positions throughout the zeolite. The material is processed using the same procedure as a traditional zeolite, where the final product may need to be activated by calcination or reduction.[91, 142-144] The majority of one-pot methods for Fe-Zeolites add Fe salts such as $FeNO_3$ or $FeSO_4$ directly into the zeolite synthesis mixture.[145-148]

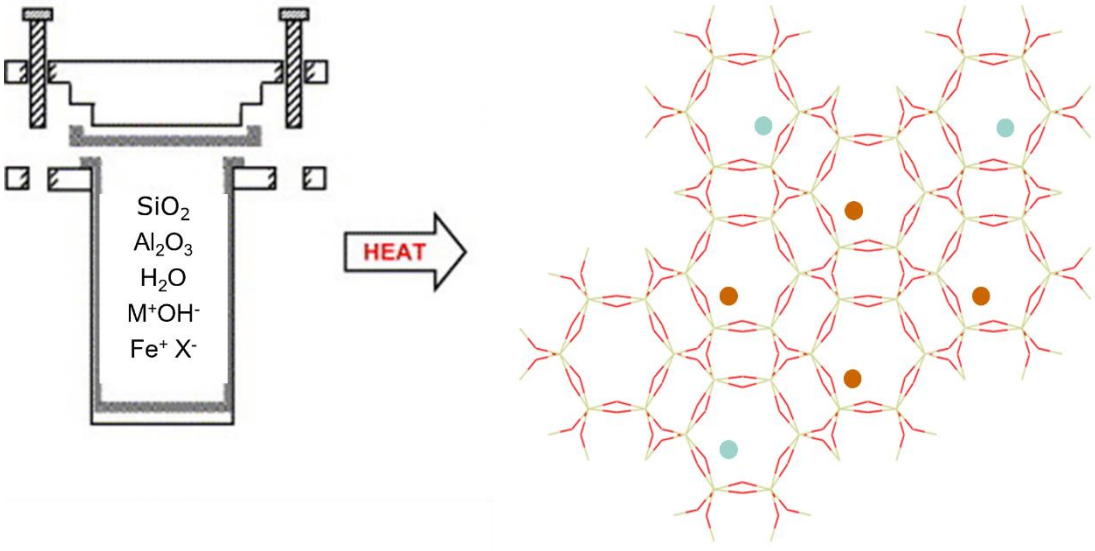

Figure 1-16. Schematic of one-pot introduction process

1.6 Transition metal complexes as OSDAs for zeolite

Using metal complexes as OSDAs for metal exchanged zeolite synthesis has the advantage of simplifying the process as the cation exchange step with the active metal can be avoided. An important consideration when using metal complexes as OSDAs in zeolite synthesis is the calcination step at the end. Calcination conditions such as temperature and air or inert environments should be carefully considered as this can affect the final metal speciation in the zeolite. There are several examples in the literature where transition metal complexes have been used in the synthesis of zeolite and aluminophosphate. For example, Cu-SAPO-18, Cu-SAPO-34 and Cu-SSZ-13 were synthesised using Cu amino complexes, these were later tested as SCR catalysts.[143, 149-152] Other transition metal complexes have been used, such as bis(pentamethylcyclopentadienyl)cobalt(III) hydroxide in the synthesis of the DON zeolite structure.[153] There are few examples of Fe complexes being used in zeolite synthesis, likely due to Fe ions in solution favouring the formation of hydroxide precipitates. Yuan et al.[154] used an EDTA-FeNa complex as an OSDA and Fe source in a one-pot method. The synthesis produced a mixture of highly dispersed isolated species and oligomeric Fe_xO_y clusters. This material exhibited good low temperature NO_x conversion in NH_3-SCR reaction however, Yuan et al. did not conduct aging studies and therefore it is unclear if this material deactivates over time. Wierzbicki et al.[155] ion exchanged ethylenediaminetetraacetate (EDTA)-Fe complexes into a de-aluminated ZSM-5 to produce Fe-ZSM5 with isolated Fe species. Like the previous study this material showed good low temperature NO_x Conversion in NH_3-SCR although yet again Wierzbicki et al. did not conduct aging studies. Agota- Aran[156] used an ammonium citrate Fe complex to produce a Fe Silicalite-1 and compared this material to Fe-ZSM5 and Fe-SSZ-13 produced using conventional ion exchange. The Fe-Silicate-1 material contained a mixture of Fe species and did not improve NO_x conversion in NH_3-SCR.

1.6.1 Characterisation of Fe zeolites

A broad variety of characterisation techniques are used to understand the iron species present in the zeolite. Quantitative Fe characterisation is very difficult as there are many different analogous Fe species. A summary of detectable Fe species by characterisation technique is shown in Table 1-4.

XRD

Structural analysis is typically done by powder X-ray diffraction (XRD) which is used to understand the crystal phase composition, and crystallinity of zeolites. When an X-ray source is shone onto a crystal the X-rays are scattered by the atoms in the crystal. The X-rays that aren't scattered pass through to the next layer of atoms and are scattered by atoms in the next layer. The scattered X-rays that undergo interference are collected by a detector to reveal a diffraction pattern. For an X-ray to diffract the sample must be crystalline and the distance between the atom layers must be similar to the X-ray wavelength.

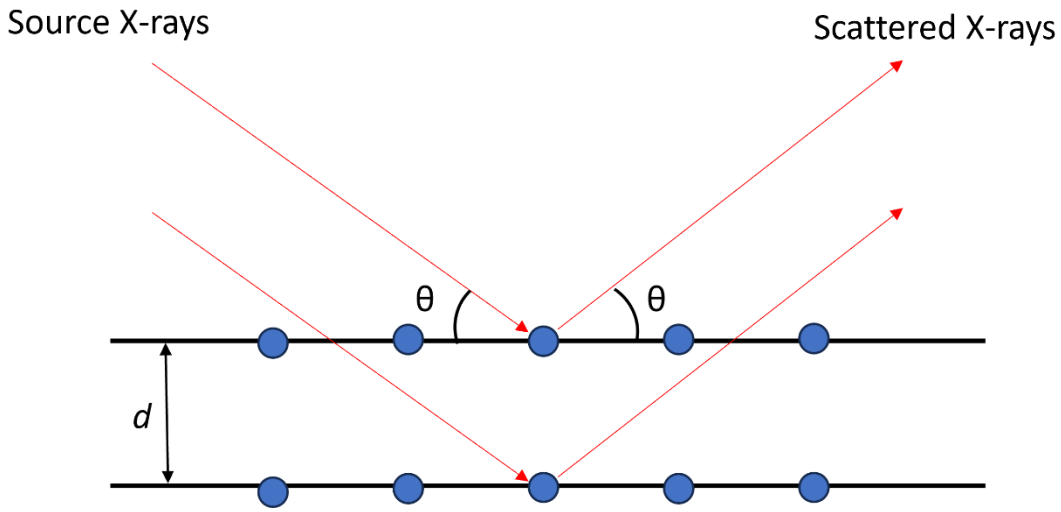

Figure 1-17. Simplified diagram of Bragg's law

Bragg's law ($Eq.1.02$) can then be used to determine the structural orientation of the atoms in the crystal (Figure 1-17).[157] Bragg's law states that when a beam of X-rays with an angle of θ encounters an atom in a crystal the X-rays are reflected at the sample angle θ. In order for the X-rays reflecting off two different planes in the crystal to interfere constructively and produce a diffraction pattern the path length d must be a whole number, n of wavelength λ.

$$n\lambda = 2dsin\theta \qquad (Eq.1.02)$$

XRD can be used to identify α-Fe_2O_3 if Fe loading is greater than 5 wt%, peaks corresponding to α-Fe_2O_3 can be seen at 33.2° and 35.5° [96, 97] (see Figure 1-18 as an example). It should be noted that when analysing Fe containing samples by XRD, using copper radiation us not

recommended as high background signals are observed due to fluorescence.[158] Fluorescence occurs as the copper emission energy is similar to the adsorption energy of Fe.[159]

analysis of samples rich in Fe the choice of X-Ray radiation should be considered. X-rays produced from copper radiation causes Fe rich samples to fluoresce as the adsorption energy is similar to copper emission energy.

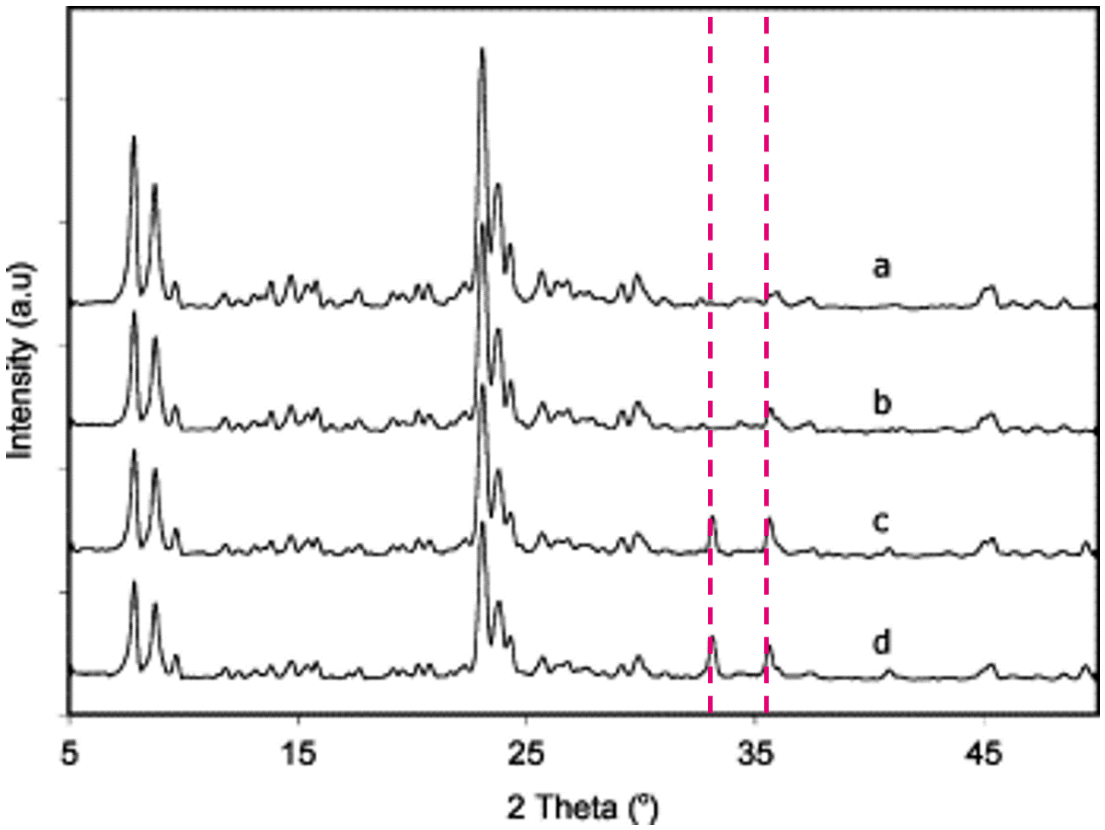

Figure 1-18. Example of XRD profiles showing samples of Fe-ZSM-5 with increasing Fe loadings a) 1 wt%; b) 2.5 wt%; c) 5 wt%; d) 7.5 wt%. Peaks corresponding to α-Fe_2O_3 are highlighted with pink lines. Adapted with permission from ref[131]. Copyright 2005 Elsevier

Fourier-transform infrared spectroscopy (FT-IR)

Fourier-transform infrared spectroscopy (FT-IR) is generally used to identify chemical functional groups and chemical species either adsorbed or intrinsic to the material. Infrared radiation is passed through a sample and some of that radiation is absorbed by the sample and converted to rotation and vibrational energy. The radiation that passes through the sample is collected and can be used to identify adsorbed species. It can also be used to understand the structure of materials by analysing the various vibrational bands that occur in the structure.

Framework species such as Fe-O-Si can be seen in bands at 660, 960 and 1080 cm^{-1}.[160] While extra-frame species are determined using probe molecules. Molecules such as NO and CO are commonly used as they form well defined complexes with high IR extinction coefficients.[161-164] These molecules can form poly-adsorption complexes ($Fe^{x+}(NO)_n$) where n = 1,2,3) which are seen in spectroscopic bands, for example mono-nitrosyl complexes are seen around 1870-80 cm^{-1} (see Figure 1-19 for an example)..[164-169] These nitrosyl species can identify the oxidation sate of the Fe in the material as mono-nitrosyls only form on Fe^{3+} while di and tri-nitrosyls can form on Fe^{2+}.[170-172]

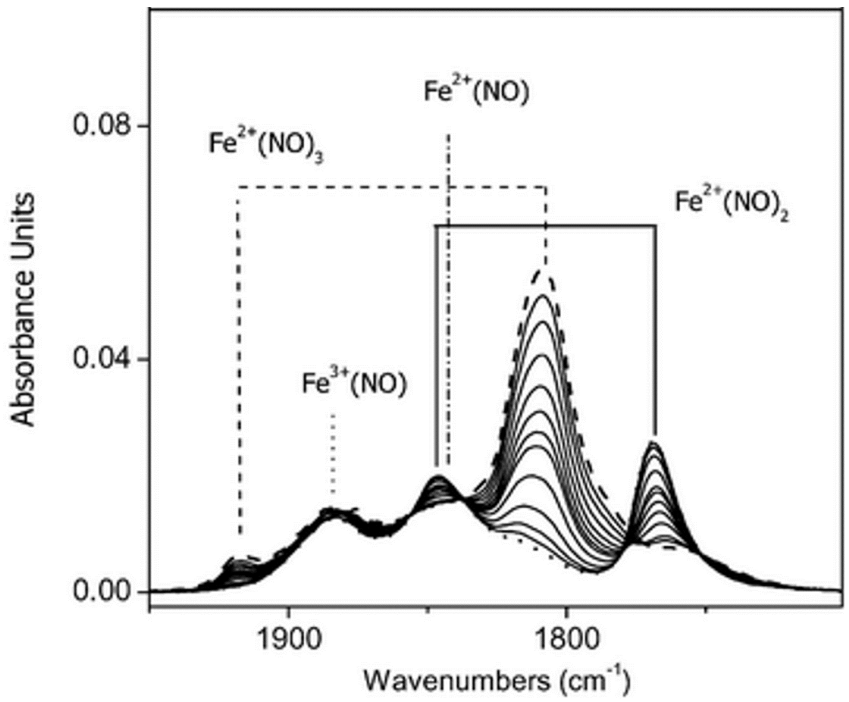

Figure 1-19. Example of FT-IR spectra of NO dosed Fe-ZSM-5 showing the spectra for mono, di and tri-nitrosyls coordinated to different oxidation states of Fe. Reproduced with permission from ref[173]. Copyright 2005 Springer Nature

DR-UVIS

Diffuse reflectance ultraviolet–visible spectroscopy (DR UV-Vis) can be used to determine the coordination species in Fe Zeolites.[174] DR UV-Vis is typically used for solid samples, reflected UV-Vis radiation is used to determine molecular spectroscopic information.[175] Peaks seen below 250 nm are related to isolated iron in a tetrahedral coordination geometry, peaks between 250 and 300 nm relate to isolated iron in octahedral coordination geometry, peaks between 300 and 450 nm relate to dimeric Fe and oligomeric Fe_xO_y species, while peaks above 450nm relate to bulk iron oxide particles[176-180] (see Figure 1-20 as an example).

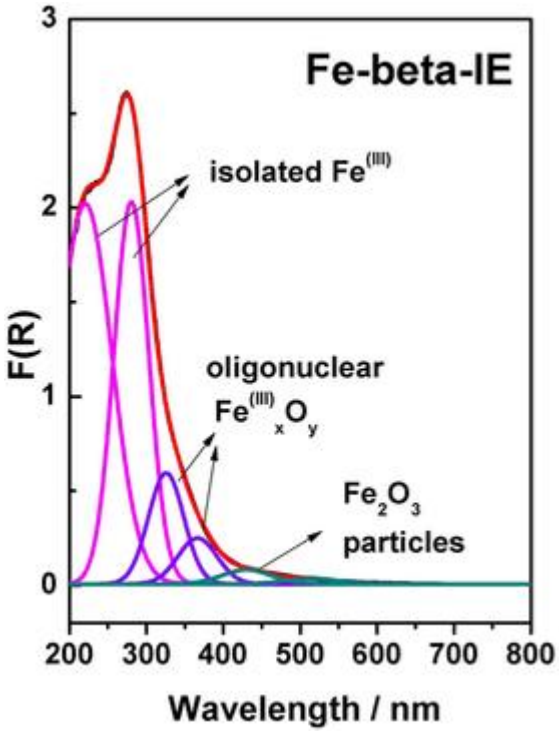

Figure 1-20. Example of DR UV-vis spectra of Fe-Beta, spectra has been deconvoluted using a gaussian function to highlight the contribution of different Fe species present in the sample. Reproduced with permission from ref[148]. Copyright 2020 Springer Nature

EPR

Electron paramagnetic resonance spectroscopy (EPR) is used to characterise the transition metal ions in zeolites. EPR uses microwave radiation to probe molecules with unpaired electrons in the presence of a magnetic field. [181] EPR is a useful tool to identify isolated Fe^{3+} species of different coordination geometries and oligomeric Fe_xO_y species. [162, 169, 182, 183] Fe signals can be found at g' = 8.8, 6 and 4.3 at low-field and g' = 2.3 and 2 at high field. Signals at g' = 8.8, 6, 4.3 and 2 are attributed to isolated Fe^{3+} and g' = 2.3 is attributed to Fe_xO_y oligomers[79] (an example can be seen in Figure 1-21).

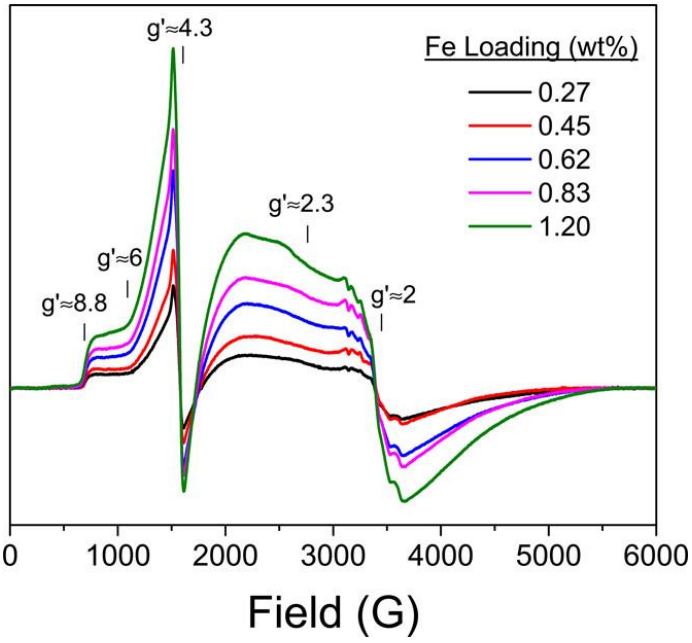

Figure 1-21. Example of EPR spectra of Fe/SSZ-13 samples measured at 125 K. Samples with different Fe loadings are shown with different colours. Reproduced with permission from ref[79]. Copyright 2016 American Chemical Society

Mößbauer

Mößbauer spectroscopy is one of the most useful tools to understand the nature of iron in samples (see Figure 1-22 as an example). The Mößbauer effect involves the nearly recoil-free emission and absorption of nuclear gamma-rays within solids. When a nucleus emits or absorbs a gamma-ray, it experiences recoil. However, in a solid crystal lattice, nuclei are bound in place and cannot freely recoil, and momentum of recoil is delivered to the surrounding crystal lattice rather than solely to the emitting or absorbing nucleus. As a result, no energy is lost to recoiling nuclei; leading to strong, resonant absorption, this then allows precise information about energy levels and interactions within solids to be determined. The technique measures the hyperfine interactions between nuclear moments and electromagnetic fields. Not all atoms are Mößbauer active, this is because low energy gamma-rays and long-lived excited states are needed for the precise measurement of energy transitions, ^{57}Fe is the most commonly studied isotope by Mößbauer spectroscopy and is used to determine the iron species and the environment around the iron in samples.[184] Tetrahedral Fe^{3+} ions can be seen in the regions of $0.1 \leq IS \leq 0.3$ mm/s and $0.87 \leq Qs \leq 1.24$ mm/s, framework tetrahedral Fe^{3+} ions can be seen at $0.25 \leq IS \leq 0.27$ mm/s and Qs (1.2-1.5 mm/s) while Fe^{2+} ions can be seen in the $0.7 \leq IS \leq 1.4$ mm/s region.[132] The line shape of the spectra can also give information about the iron, a doublet feature relates to paramagnetic iron and sextet features relate to magnetic iron.[79, 127]

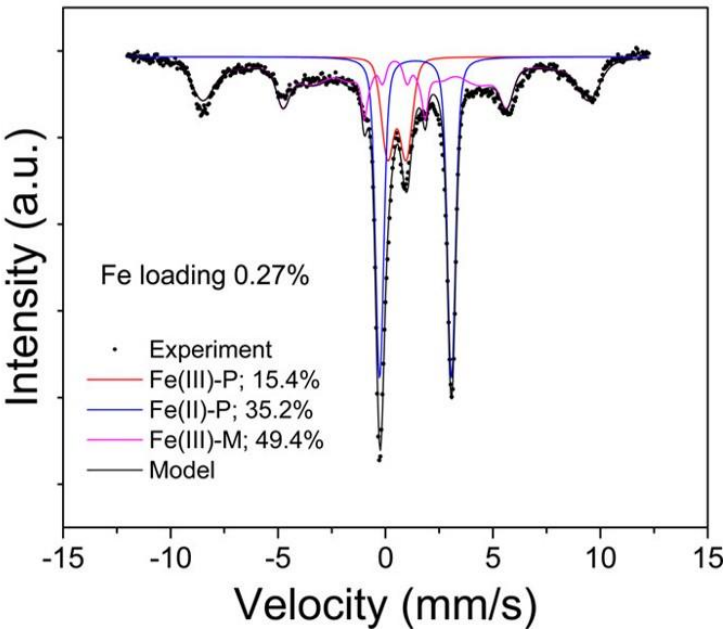

Figure 1-22. Example of 3.3.3.4 Mößbauer spectra of Fe/SSZ-13. Peak fitting results of Fe 0.27% 57Fe/SSZ-13 sample. Percentages of three the components, Fe(II)-Paramagnetic, Fe(III)-Paramagnetic, and Fe(III)-Magnetic, are also displayed. Reproduced with permission from ref[79]. Copyright 2016 American Chemical Society

XPS

X-ray photoelectron spectroscopy (XPS) can be used to understand the oxidation state of iron within zeolite samples. X-rays are absorbed by electrons in a sample, electrons with enough energy are ejected by the sample with a certain kinetic energy. A detector measures the energy of the ejected electrons which are specific to different elements.[185] For Fe samples the most used signals are: the Fe2p signal, as it is the strongest, while the weaker Fe3p signal can also be used for quantification. The Fe2p core levels are split into $Fe2p_{1/2}$ and $Fe2p_{3/2}$ doublets due to spin-orbit coupling,[186] the binding energies of these levels have been shown to be dependent on the state of iron in the sample.[187-191] Satellite features are also used to distinguish between Fe^{2+} and Fe^{3+} in the spectra[192] (an example can be seen in Figure 1-23).

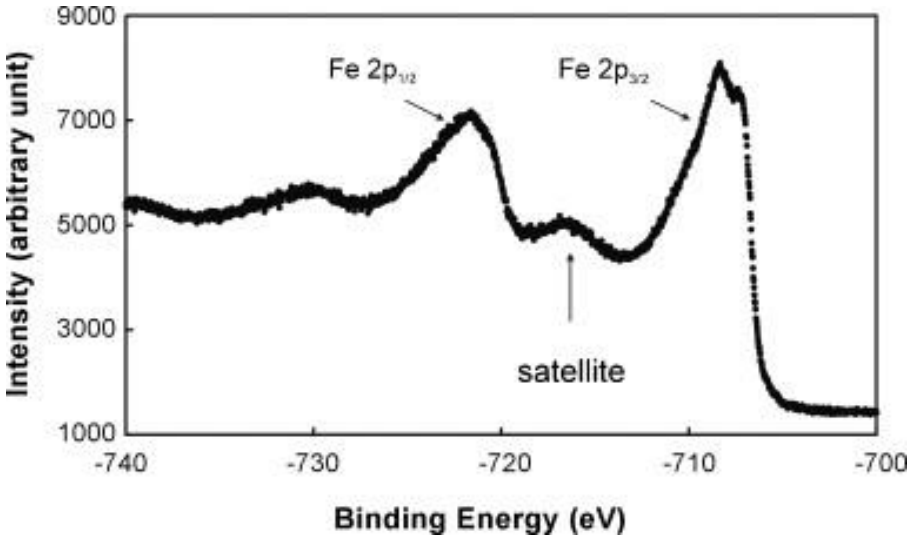

Figure 1-23. Example of XPS spectra of Fe samples showing various features in the Fe2p signal. Reproduced with permission from ref[190]. Copyright 2008 Elsevier

H_2-TPR

Hydrogen temperature programmed reduction (H_2-TPR) is a technique that is used to understand the surface chemistry of metals and metal oxides under varying temperature conditions. The technique can be applied to Fe zeolites to understand the Fe species present in the zeolite. Hydrogen is flowed over a sample and monitored as the temperature is increased. An increase in the hydrogen consumption at different temperatures can indicate specific reduction events. For example, increases of hydrogen consumption at temperature below 773 K points to the reduction of Fe^{3+} in isolated ions, oligomeric clusters, or nanoparticles, hydrogen consumption between 773 and 1023 K indicates the reduction of Fe^{2+} to Fe^0 in oligomeric clusters or nanoparticles and hydrogen consumption at temperatures above 1023 K indicate the reduction of Fe^{2+} to Fe^0 of isolated species [132, 154, 165, 193] (an example can be seen in Figure 1-24).

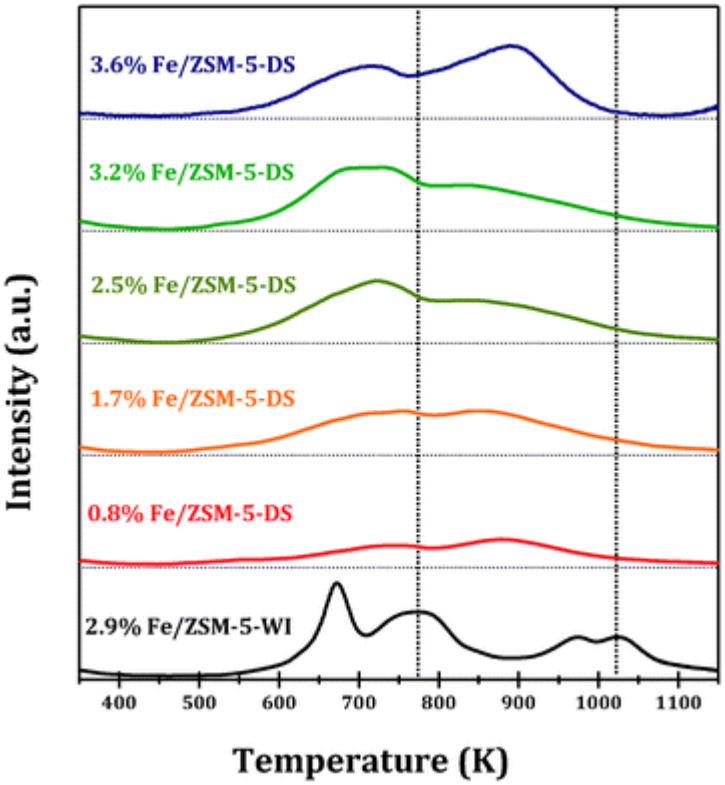

Figure 1-24. Example of H_2-TPR profiles of Fe/ZSM-5 samples with different Fe loadings. Reproduced with permission from ref [154]. Copyright Royal Society of Chemistry (2017)

Table 1-4. Summary of detectable Fe species by each technique

Technique	Detectable Fe species
XRD	> 5 wt% Fe: α-Fe_2O_3
FT-IR	Fe-OH, Bridged Si(OH)Fe, Fe-O-Si, Fe^{2+} and Fe^{3+} (using probe molecules)
DR-UV-Vis	Isolated Fe ions in tetrahedral and octahedral coordination, dimeric Fe, oligomeric Fe_xO_y species, bulk iron oxide particles
EPR	Isolated Fe^{3+} and oligomeric Fe_xO_y species
Mößbauer	Fe^{3+} ions with tetrahedral coordination, Framework substituted Fe^{3+}, Small Fe_xO_y nanoparticles in octahedral coordination, Fe-O-Fe pairs, Fe^{2+} ions
XPS	Fe^{2+}, Fe^{3+},Fe_2O_3, Fe_3O_4
H_2-TPR	Fe^{3+} (isolated Fe^{3+}, Fe_xO_y, α-Fe_2O_3 nanoparticles), Extra-framework Fe^{3+} to Fe^{2+}, Framework Fe^{3+} to Fe^{2+}, Fe^0

1.7 Fe Zeolites for SCR applications

Modern NH_3-SCR systems use Cu zeolites as they are more active at lower temperatures and have excellent hydrothermal stability. Cu-SSZ-13 was first reported for the NH_3-SCR reaction in a patent in which it was able to achieve 90-100% NO_x conversion.[194] Later, Kwak et al.[72] published results showing Cu-SSZ-13 outperformed both Cu-beta and Cu-ZSM-5 and, it has also been shown Cu-SSZ-13 produces less N_2O than both Cu-beta and Cu-ZSM-5.[195] Those discoveries led to the commercialisation of Cu-SSZ-13 for diesel engine exhaust aftertreatments.[196-198] While Cu-zeolite are preferred for automotive applications research is ongoing into Fe zeolite as they show improved higher temperature SCR activity and generate less N_2O over their Cu counterparts.[127]

There is still uncertainty around the exact nature of the active Fe centre that catalyses the NH_3-SCR reaction however, studies in the last decade have indicated that the majority of Fe containing moieties can contribute to NH_3-SCR.[199-202] Fe Zeolites are less active than Cu zeolites for low temperature (≤ 300 °C) standard SCR (R 1.12), however at high temperatures (>300 °C) they are more active and selective toward N_2 than Cu Zeolites (an example can be seen in Figure 1-25).[203, 204] Low temperature activity can be enhanced for Fe zeolites by increasing the ratio of N_2O leading to the so called fast SCR reaction (R 1.13),[110] however this is difficult to control in practice due to the low activity of the DOC at low temperatures.[28, 205] This lower , low temperature activity for standard SCR is the main issue with the use of Fe zeolites for SCR. The lower activity is suggested to be caused by ammonia inhibition,[206] this has been explained as the strong complexing of NH_3 with Fe^{2+} or Fe^{3+} ions rendering them inactive for further reactions. However, this is disputed as in aqueous media Cu^{2+} and Cu^{1+} ions form much stronger NH_3 complexes while Fe ions prefer to form hydroxide precipitates.[127] Another explanation is that NH_3 can readily reduce Fe^{3+} to Fe^{2+} under low temperature SCR conditions and this interferes with the redox cycle during the SCR reaction. This second explanation seems more plausible as Fe zeolites are known to be more active for the fast SCR (R 1.13) as Fe^{3+}/Fe^{2+} redox cycling is not kinetically limiting for this reaction.[207]

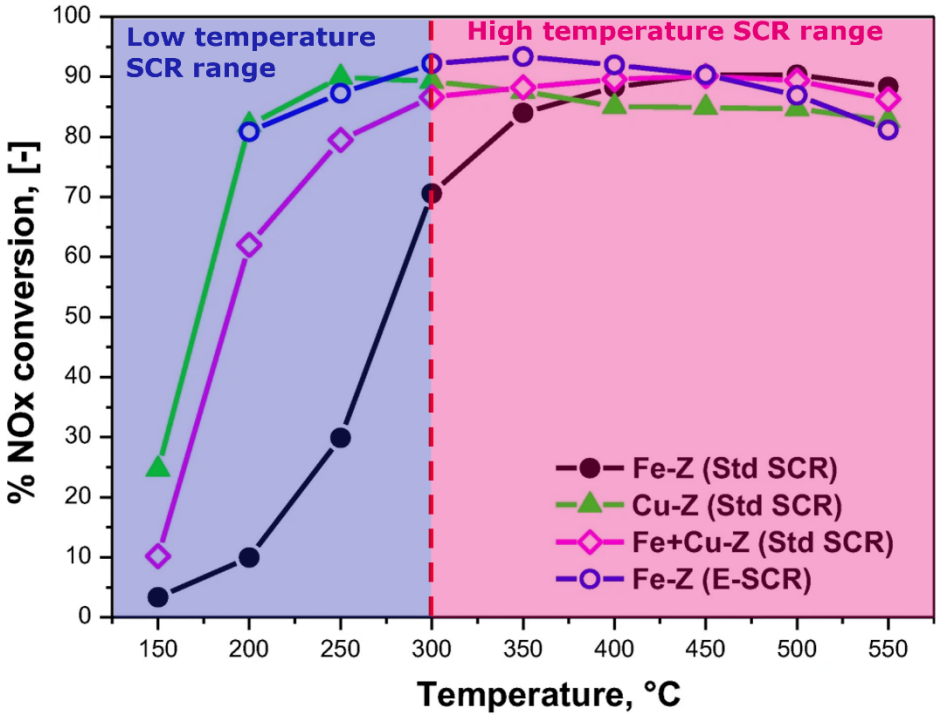

Figure 1-25. Example of a NOx conversion vs Temperature plot from ref[204]. Plot has been adapted with permission to highlight the low and high temperature zones

1.7.1 Mechanism of NO_X reduction using Fe-Zeolites

A definitive mechanism for standard NH_3-SCR over Fe zeolites has yet to be confirmed. The numerous side reactions and lack of clarity of the active Fe sites for the reaction makes it difficult to devise a mechanism. Most proposed mechanisms use a redox cycle where Fe is reversibly oxidised and reduced however, there is a debate around the various intermediates that form during the process. Ruggeri et al. trapped and identified intermediates using physical mixtures of BaO/Al_2O_3 and Fe-ZSM5.[208] They propose that the mechanism occurs via a HONO species (R 1.21– 1.24) in which the active specie is a monomeric hydroxylated Fe^{3+}. This series of reactions eventually produce a nitrate species (R 1.25). Other intermediates such as N_2O_4 or NO^+ have also been proposed.[209-211]

$$Fe^{3+}OH + NO \leftrightarrow Fe^{2+} + HONO \quad (R\ 1.21)$$

$$HONO + Fe^{3+}\ OH \leftrightarrow Fe^{3+}ONO + H_2O \quad (R1.22)$$

$$Fe^{3+}ONO \rightarrow Fe^{2+} + NO_2 \quad (R1.23)$$

$$2Fe^{2+} + \frac{1}{2}O_2 + H_2O \rightarrow 2\,Fe^{3+}OH \quad (R1.24)$$

$$Fe^{3+}ONO + NO_2 \rightarrow Fe^{3+}NO_3 + NO \quad (R1.25)$$

The final steps in the reaction can then proceed via NH_4NO_3 formation[27, 207, 212, 213] (R 1.26) as NH_3 reactions with a Brønsted acid site to form NH_4^+, NH_4NO_3 can then decompose via N_2O[213] (R1.27 -1.28) to form nitrogen and water.[203, 214]

$$Fe^{3+}NO_3 + NH_4^+ \rightarrow Fe^{3+} + NH_4NO_3 \quad (R1.26)$$

$$NH_4NO_3 \rightarrow N_2O + 2H_2O \quad (R1.27)$$

$$3N_2O + 2NH_3 \rightarrow 4N_2 + 3H_2O \quad (R1.28)$$

Alternative mechanisms using theoretical studies suggest the reaction proceeds via the adsorption of NH_3 with an Fe^{3+} site to form a $Fe^{2+}NH_2$ species.[215] This then reacts with NO to form N_2 and water while the Fe^{2+} site is re-oxidised by O_2.[215-217] Boubnov et al. used operando studies of HERFD-XANES (high energy resolution fluorescence detected X-ray absorption near edge structure) and valence to core X-ray emission spectroscopy to probe the mechanism. They concluded that the mechanism proceeded via the pathway shown in Scheme 1-1 with the key reactions in this pathway being: 1) Adsorption of NO and ammonia on an Fe^{3+} site resulting in the reduction to Fe^{2+}, 2) release of Fe^{2+}, N_2 and water, 3) reoxidation of Fe^{2+} which is stated as the rate limiting step, 4) water inhibition by adsorption onto the active site.[217]

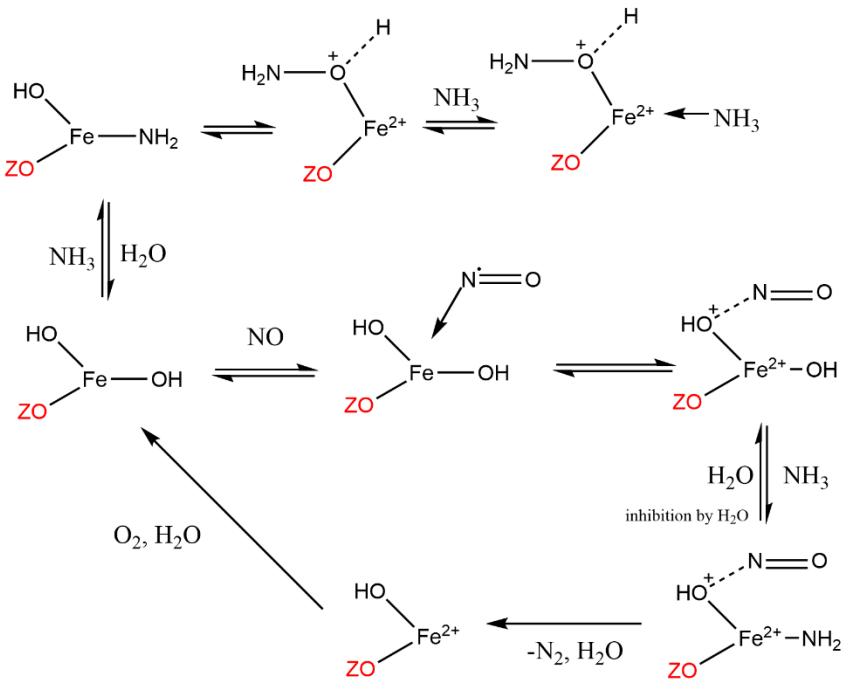

Scheme 1-1 Suggested intermediates during SCR of NO over ZSM-5[217]

In addition to the main SCR reaction Fe zeolites have also been found to consume more NH_3 than is needed for standard SCR.[218] This overconsumption is not though to be from non-selective NH_3 oxidation (R 1.18) as it has not been seen below 300 °C [79] but likely from 'parasitic NH_3 oxidation' such as reactions of NH_3 with O_2 as in reaction R1.29.[79] This reaction is likely catalysed by oligomeric Fe_xO_y. Brandenberger et al. conducted a series of experiments using ZSM-5 that contained only monomeric iron species and these experiments showed no NH_3 oxidation activity up to 500 °C, whereas samples that contained larger amounts of iron in the form of clusters were more active for NH_3 oxidation.[128] This is likely due to the stronger O_2 activation potential of Fe_xO_y species.

$$NO_2 + 2NH_3 + O_2 \rightarrow NO + N_2 + 3H_2O \qquad (R1.29)$$

Low temperature NH_3 -SCR (<300 °C) activity in Fe zeolites is thought to be catalysed by isolated Fe^{3+} species. In situ X-ray absorption near edge structure (XANES) analysis has suggested isolated tetrahedral,[219] octahedral and distorted[202] Fe^{3+} species are responsible for the low temperature activity.

To summarise, specific Fe speciation correlating to NH_3-SCR performance is still debated. In general, it can be said that isolated Fe species account for low temperature NH_3-SCR performance in Fe-zeolites, while isolated and polyatomic Fe species contribute to the higher temperature NH_3-SCR performance. If a method could be developed to control the Fe species produced in SSZ-13 then an Fe-SSZ-13 could be produced which outperforms Cu counterparts

1.8 Novel Fe-SSZ-13 preparation

The development of novel Fe containing OSDAs could lead to the synthesis of highly active Fe containing zeolites. One example of an Fe containing complex is ferrocene, which consists of two cyclopentadienyl rings bound to a central Fe atom in a +2 oxidation state. The compound is stable at high temperatures (400 °C) and in the presence of air and water. Ferrocene can undergo many reactions to produce various derivatives. It can react in a Mannich reaction to produce N,N-dimethylaminomethylferrocene (Scheme 1-2), this can then be methylated to produce (Ferrocenylmethyl)trimethylammonium (FMTMA) (*Scheme* 1-3), which creates an ammonium functional group and can be used as an OSDA in zeolite synthesis.[220]

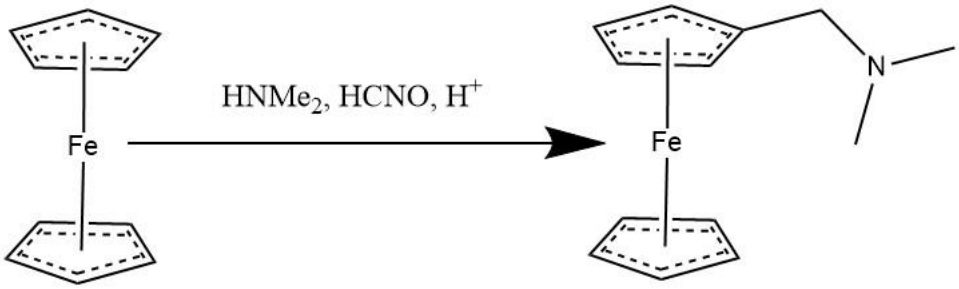

Scheme 1-2. Example synthesis of N,N-dimethylaminomethylferrocene

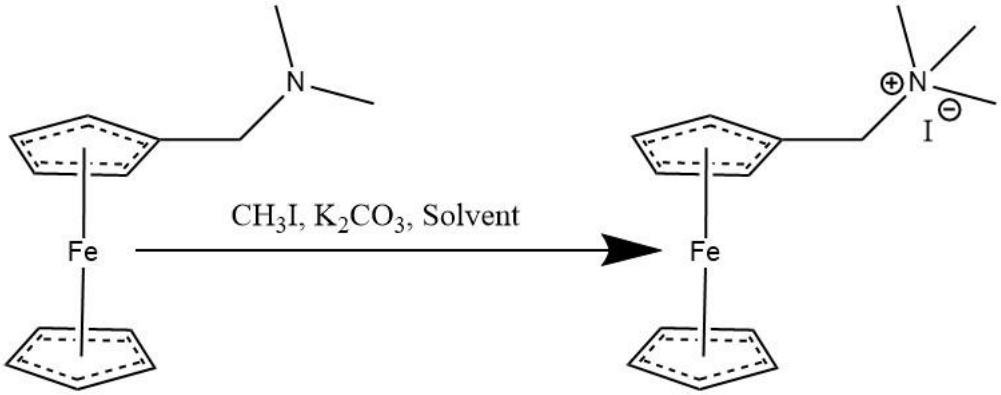

Scheme 1-3. Synthesis of (Ferrocenylmethyl)trimethylammonium via the methylation of N,N-dimethylaminomethylferrocene with methyl iodide.

1.9 Scope of this work

Global warming and the release of harmful pollutants into the atmosphere is having a detrimental impact on the environment and the health of people on a global scale. Nitrous oxides produced from the exhaust of diesel vehicles pollute the atmosphere, leading to the formation of acid rain and respiratory diseases in the general population. Reducing emissions from transportation sector will have a significant impact on this global issue. Advances of environmental catalysis are vital to prevent the acceleration of these catastrophic events. Iron modified zeolites have been shown to be active for the selective catalytic reduction of NO_x. Understanding how these materials work will aid in the development of improved versions of NH_3-SCR catalysts that could be used at scale and reduce the emissions of harmful gasses. This thesis will examine the synthesis of Fe-SSZ-13 for NH_3-SCR. The first part of this thesis will focus on the extensive synthesis of Fe-SSZ-13 using a ferrocene-based structure directing agent, while the second part will focus on the testing and characterisation of the Fe-SSZ-13 as well as comparison with other Fe-SSZ-13 made using traditional methods. Below is an outline of the work undertaken for this thesis.

Synthesis of Fe-SSZ-13 using a ferrocene-based structure directing agent for the NH_3 -SCR reaction

- Investigation of synthesis parameters to find suitable conditions to produce phase pure SSZ-13 using the ferrocene directing agent.
- Characterisation of the ferrocene-based Fe-SSZ-13 material and identification the Fe species present.

- NH_3 -SCR testing of the ferrocene-based Fe-SSZ-13 and comparison with a benchmark material.
- Correlation of Fe species to activity and any deactivation of the material.

1.10 References

1. C. R. Catlow, M. Davidson, C. Hardacre and G. J. Hutchings, *Philosophical Transactions of the Royal Society A: Mathematical, Physical and Engineering Sciences*, 2016, **374**.
2. J. J. Berzelius, *Jahres-Bericht* 1835, **4**, 1823-1825.
3. K. J. Laidler, *Pure Appl. Chem.*, 1996, **68**, 149-192.
4. I. N. J. W. Chorkendorff, Wiley-VCH GmbH & co. KGaA, Newark, 2003, ch. 1, p. 3.
5. A. R. Ravishankara, J. S. Daniel and R. W. Portmann, *Science*, 2009, **326**, 123-125.
6. F. X. Meixner and W. X. Yang, in *Dryland Ecohydrology*, 2006, ch. 14, pp. 233-255.
7. G. Busca, L. Lietti, G. Ramis and F. Berti, *Applied Catalysis B: Environmental*, 1998, **18**, 1-36.
8. Y. B. Zel'dovich, *Acta Physicochimica USSR*, 1946, **21**, 577–628.
9. G. A. Lavoie, J. B. Heywood and J. C. Keck, *Combust. Sci. Technol.*, 1970, **1**, 313-326.
10. U. S. EPA, *Integrated Science Assessment (ISA) for Oxides of Nitrogen - Health Criteria (Final Report, Jan 2016)*, U.S. Environmental Protection Agency, 2016.
11. U. E. P. A. U. EPA), *Review of National Ambient Air Quality Standards for Ozone: Assessment of Scientific and Technical Information.* , O. o. A. Q. P. a. Standards Report EPA-452/R-96-007, Research Triangle Park. NC., 1996.
12. P. J. Crutzen, *Annual Review of Earth and Planetary Sciences*, 1979, **7**, 443-472.
13. U. E. P. A. U. EPA), *Nitrogen Oxides (NOx), Why and How They Are Controlled*, I. T. a. P. I. Division Report EPA-456/F-99-006R, Research Triangle Park. NC., 1999.
14. R. O'Driscoll, M. E. J. Stettler, N. Molden, T. Oxley and H. M. ApSimon, *Sci. Total Environ.*, 2018, **621**, 282-290.
15. EU Commission, *Journal*, Regulation (EC) No 715/2007 of the European Parliament and of the Council of 20 June 2007 on type approval of motor vehicles with respect to emissions from light passenger and commercial vehicles (Euro 5 and Euro 6) and on access to vehicle repair and maintenance information.
16. EU Commission, *Journal*, Regulation (EC) No 595_2009 of the European Parliament and of the Council of 18 June 2009 on type-approval of motor vehicles and engines with respect to emissions from heavy duty vehicles (Euro VI) and on access to vehicle repair and maintenance information.
17. F. Endter, *Chem. Ing. Tech.*, 1958, **30**, 305-310.
18. D. Cobb, L. Glatch, J. Ruud and S. Snyder, *Environ. Prog.*, 1991, **10**, 49-59.
19. J. Gibson, O. Groene, *Automotive Engineering*, 1991, 18-22.
20. DMGK, *AdBlue as a Reducing Agent for the Decrease of NOx Emissions from Diesel Engines of Commercial Vehicles*, Report Research Report 616-1, DMGK, 2003.
21. D. Chatterjee, T. Burkhardt, T. Rappe, A. Güthenke and M. Weibel, *SAE International Journal of Fuels and Lubricants*, 2009, **1**, 440-451.
22. K. Hauff, U. Tuttlies, G. Eigenberger and U. Nieken, *Applied Catalysis B: Environmental*, 2012, **123-124**, 107-116.
23. S. Mohankumar and P. Senthilkumar, *Renewable and Sustainable Energy Reviews*, 2017, **80**, 1227-1238.
24. A. Srinivasan and K. Price, presented in part at the SAE Technical Paper Series, 2019.

25. J. He, K. Chen and J. Xu, in *Encyclopedia of Sustainable Technologies*, ed. M. A. Abraham, Elsevier, Oxford, 2017, pp. 243-257.
26. M. Koebel, G. Madia and M. Elsener, *Catal. Today*, 2002, **73**, 239-247.
27. A. Grossale, I. Nova and E. Tronconi, *Catal. Today*, 2008, **136**, 18-27.
28. M. Iwasaki and H. Shinjoh, *Applied Catalysis A: General*, 2010, **390**, 71-77.
29. Y. Pu, X. Xie, W. Jiang, L. Yang, X. Jiang and L. Yao, *Chin. Chem. Lett.*, 2020, **31**, 2549-2555.
30. J. W. Girard, G. Cavataio and C. K. Lambert, *SAE Transactions*, 2007, **116**, 182-186.
31. A. F. Cronstedt, *Svenska Vetenskaps Akademiens Handlingar Stockholm*, 1756, **17**, 120.
32. M. Avrami, *The Journal of Chemical Physics*, 1939, **7**, 1103-1112.
33. D. W. Breck, *Zeolite molecular sieves : structure, chemistry, and use*, Wiley, New York, 1973.
34. R. M. Barrer, *J. Chem. Soc.*, 1948, 127-132.
35. R. M. Barrer, L. Hinds and E. A. White, *J. Chem. Soc.*, 1953, 1466-1475.
36. R. M. Barrer and C. Marcilly, *J Chem Soc A*, 1970, 2735-2745.
37. W. M. Meier and G. T. Kokotailo, *Zeitschrift für Kristallographie - Crystalline Materials*, 1965, **121**, 211-219.
38. P. A. Jacobs and J. A. Martens, *Introduction to Zeolite Science and Practice*, 2001, **58**, 445-496.
39. C. Baerlocher., D. Brouwer., B. Marler. and L. B. McCusker., *Database of Zeolite Structures,* http://www.iza-structure.org/databases/
40. LoewensteinWalter, *Am. Mineral.*, 1954, **39**, 92-96.
41. E. M. Flanigen, in *Introduction to Zeolite Science and Practice*, 1991, ch. 2, pp. 13-34.
42. S. K. Masoudian, S. Sadighi and A. Abbasi, *Bulletin of Chemical Reaction Engineering & Catalysis*, 2013, **8**.
43. E. T. Vogt and B. M. Weckhuysen, *Chem Soc Rev*, 2015, **44**, 7342-7370.
44. A. Corma, *Chemical Reviews*, 1995, **95**, 559-614.
45. J. Sauer, *Chemical Reviews*, 1998, **89**, 199-255.
46. R. A. van Santen and G. J. Kramer, *Chemical Reviews*, 1995, **95**, 637-660.
47. M. Boronat and A. Corma, *Catal. Lett.*, 2014, **145**, 162-172.
48. C. T. W. Chu and C. D. Chang, *The Journal of Physical Chemistry*, 1985, **89**, 1569-1571.
49. L. Ni, R. Khare, R. Bermejo-Deval, R. Zhao, L. Tao, Y. Liu and J. A. Lercher, *J Am Chem Soc*, 2022, **144**, 12347-12356.
50. P. Gao, Q. Wang, J. Xu, G. Qi, C. Wang, X. Zhou, X. Zhao, N. Feng, X. Liu and F. Deng, *ACS Catalysis*, 2017, **8**, 69-74.
51. T. Ennaert, J. Van Aelst, J. Dijkmans, R. De Clercq, W. Schutyser, M. Dusselier, D. Verboekend and B. F. Sels, *Chem. Soc. Rev.*, 2016, **45**, 584-611.
52. R. K. Mishra, S. M. Chistie, S. U. Naika and K. Mohanty, *Bioresour. Technol.*, 2022, **366**.
53. H. Y. Luo, J. D. Lewis and Y. Román-Leshkov, *Annual Review of Chemical and Biomolecular Engineering*, 2016, **7**, 663-692.
54. Q. Zhang, S. Gao and J. Yu, *Chem Rev*, 2023, **123**, 6039-6106.
55. A. Palčić and V. Valtchev, *Applied Catalysis A: General*, 2020, **606**.
56. D. H. Dompas, W. J. Mortier, O. C. H. Kenter, M. J. G. Janssen and J. P. Verduijn, *Journal of Catalysis*, 1991, **129**, 19-24.
57. W. J. Mortier, *Journal of Catalysis*, 1978, **55**, 138-145.
58. A. Chatterjee, T. Iwasaki, T. Ebina and A. Miyamoto, *Microporous and Mesoporous Materials*, 1998, **21**, 421-428.
59. S. Liu, Y. He, H. Zhang, Z. Chen, E. Lv, J. Ren, Y. Yun, X. Wen and Y.-W. Li, *Catalysis Science & Technology*, 2019, **9**, 2812-2827.

60. M. Trachta, O. Bludský, J. Vaculík, R. Bulánek and M. Rubeš, *Scientific Reports*, 2023, **13**.
61. A. J. Jones, R. T. Carr, S. I. Zones and E. Iglesia, *Journal of Catalysis*, 2014, **312**, 58-68.
62. G. Li, C. Liu, R. Rohling, E. J. M. Hensen and E. A. Pidko, in *Modelling and Simulation in the Science of Micro- and Meso-Porous Materials*, 2018, ch. 7, p. 231.
63. S. M. Csicsery, *Zeolites*, 1984, **4**, 202-213.
64. F. G. Dwyer and T. F. Degnan, in *Fluid Catalytic Cracking: Science and Technology*, Elsevier Science Publishers B.V., 1993, pp. 499-530.
65. M. E. Davis, *Industrial & Engineering Chemistry Research*, 1991, **30**, 1675-1683.
66. T. F. Degnan, *Journal of Catalysis*, 2003, **216**, 32-46.
67. R. M. Barrer, *Zeolites*, 1981, **1**, 130-140.
68. J. Weitkamp and L. Puppe, *Catalysis and Zeolites*, 1999.
69. C. S. Cundy and P. A. Cox, *Microporous and Mesoporous Materials*, 2005, **82**, 1-78.
70. J. Grand, H. Awala and S. Mintova, *CrystEngComm*, 2016, **18**, 650-664.
71. H.-Y. Chen, Z. Wei, M. Kollar, F. Gao, Y. Wang, J. Szanyi and C. H. F. Peden, *Journal of Catalysis*, 2015, **329**, 490-498.
72. J. H. Kwak, R. G. Tonkyn, D. H. Kim, J. Szanyi and C. H. F. Peden, *Journal of Catalysis*, 2010, **275**, 187-190.
73. J. H. Kwak, D. Tran, S. D. Burton, J. Szanyi, J. H. Lee and C. H. F. Peden, *Journal of Catalysis*, 2012, **287**, 203-209.
74. Y. Shan, X. Shi, G. He, K. Liu, Z. Yan, Y. Yu and H. He, *The Journal of Physical Chemistry C*, 2018, **122**, 25948-25953.
75. Y. Luo, Y. Zhu, J. Pan and X. Chen, *Green Chemistry*, 2020, **22**, 1681-1697.
76. D. Wang, L. Zhang, K. Kamasamudram and W. S. Epling, *ACS Catalysis*, 2013, **3**, 871-881.
77. Zones, Chevron USA Inc, Zeolite SSZ-13 and its method of preparation, US, US4544538A, 1983
78. M. Kumar, H. Luo, Y. Roman-Leshkov and J. D. Rimer, *J Am Chem Soc*, 2015, **137**, 13007-13017.
79. F. Gao, Y. Zheng, R. K. Kukkadapu, Y. Wang, E. D. Walter, B. Schwenzer, J. Szanyi and C. H. F. Peden, *ACS Catalysis*, 2016, **6**, 2939-2954.
80. F. Gao, M. Kollár, R. K. Kukkadapu, N. M. Washton, Y. Wang, J. Szanyi and C. H. F. Peden, *Applied Catalysis B: Environmental*, 2015, **164**, 407-419.
81. H. Robson, *Verified synthesis of zeolitic materials*, Gulf Professional Publishing, 2001.
82. S. I. Zones, Google Patents, Zeolite SSZ-13 and its method of preparation, 1985
83. S. I. Zones, *Microporous and Mesoporous Materials*, 2011, **144**, 1-8.
84. Y. Miller, Preparation of zeolites using novel structure directing agents, US, US7597874B1, 2008
85. M. Itakura, T. Inoue, A. Takahashi, T. Fujitani, Y. Oumi and T. Sano, *Chem. Lett.*, 2008, **37**, 908-909.
86. N. Martin, M. Moliner and A. Corma, *Chem. Commun*, 2015, **51**, 9965-9968.
87. R. Xu, R. Zhang, N. Liu, B. Chen and S. Zhang Qiao, *ChemCatChem*, 2015, **7**, 3842-3847.
88. B. Chen, R. Xu, R. Zhang and N. Liu, *Environmental Science & Technology*, 2014, **48**, 13909-13916.
89. L. Wu, V. Degirmenci, P. C. M. M. Magusin, N. J. H. G. M. Lousberg and E. J. M. Hensen, *Journal of Catalysis*, 2013, **298**, 27-40.
90. L. Xie, F. Liu, L. Ren, X. Shi, F.-S. Xiao and H. He, *Environmental Science & Technology*, 2013, **48**, 566-572.
91. L. Ren, L. Zhu, C. Yang, Y. Chen, Q. Sun, H. Zhang, C. Li, F. Nawaz, X. Meng and F. S. Xiao, *Chem. Commun.*, 2011, **47**, 9789-9791.

92. J. Wang, Z. Peng, H. Qiao, L. Han, W. Bao, L. Chang, G. Feng and W. Liu, *RSC Adv.*, 2014, **4**, 42403-42411.
93. X. Wang, Q. Wu, C. Chen, S. Pan, W. Zhang, X. Meng, S. Maurer, M. Feyen, U. Müller and F.-S. Xiao, *Chemical Communications*, 2015, **51**, 16920-16923.
94. Y. Ji, M. A. Deimund, Y. Bhawe and M. E. Davis, *ACS Catalysis*, 2015, **5**, 4456-4465.
95. L. Van Tendeloo, E. Gobechiya, E. Breynaert, J. A. Martens and C. E. A. Kirschhock, *Chem. Commun.*, 2013, **49**.
96. S. I. Zones and R. A. Van Nordstrand, *Zeolites*, 1988, **8**, 166-174.
97. M. Itakura, I. Goto, A. Takahashi, T. Fujitani, Y. Ide, M. Sadakane and T. Sano, *Microporous and Mesoporous Materials*, 2011, **144**, 91-96.
98. T. Takata, N. Tsunoji, Y. Takamitsu, M. Sadakane and T. Sano, *Microporous and Mesoporous Materials*, 2016, **225**, 524-533.
99. I. Goto, M. Itakura, S. Shibata, K. Honda, Y. Ide, M. Sadakane and T. Sano, *Microporous and Mesoporous Materials*, 2012, **158**, 117-122.
100. M. Dusselier and M. E. Davis, *Chem Rev*, 2018, **118**, 5265-5329.
101. L. Tang, K.-G. Haw, Y. Zhang, Q. Fang, S. Qiu and V. Valtchev, *Microporous and Mesoporous Materials*, 2019, **280**, 306-314.
102. H. Geng, G. Li, D. Liu and C. Liu, *Journal of Solid State Chemistry*, 2018, **265**, 193-199.
103. N. Kosinov, C. Liu, E. J. M. Hensen and E. A. Pidko, *Chem Mater*, 2018, **30**, 3177-3198.
104. A. Primo and H. Garcia, *Chem Soc Rev*, 2014, **43**, 7548-7561.
105. C. Perego, V. Calemma and P. Pollesel, in *Zeolites and Catalysis*, 2010, ch. 19, pp. 585-621.
106. G. Caeiro, R. H. Carvalho, X. Wang, M. A. N. D. A. Lemos, F. Lemos, M. Guisnet and F. Ramôa Ribeiro, *J. Mol. Catal. A: Chem.*, 2006, **255**, 131-158.
107. Z. R. Ismagilov, E. V. Matus and L. T. Tsikoza, *Energy & Environmental Science*, 2008, **1**.
108. B. Han, Y. Yang, Y. Xu, U. J. Etim, K. Qiao, B. Xu and Z. Yan, *Chinese Journal of Catalysis*, 2016, **37**, 1206-1215.
109. E. Taarning, C. M. Osmundsen, X. Yang, B. Voss, S. I. Andersen and C. H. Christensen, *Energy Environ. Sci.*, 2011, **4**, 793-804.
110. S. Brandenberger, O. Kröcher, A. Tissler and R. Althoff, *Catalysis Reviews*, 2008, **50**, 492-531.
111. L. Zhang, Y. Peng, J. Zhang, L. Chen, X. Meng and F.-S. Xiao, *Chinese Journal of Catalysis*, 2016, **37**, 800-809.
112. D. Shahidi, R. Roy and A. Azzouz, *Applied Catalysis B: Environmental*, 2015, **174-175**, 277-292.
113. G. Centi and S. Perathoner, in *Zeolites and Catalysis*, 2010, ch. 24, pp. 745-774.
114. S. Sartipi, M. Makkee, F. Kapteijn and J. Gascon, *Catal. Sci. Technol.*, 2014, **4**, 893-907.
115. C. Perego, A. Carati, P. Ingallina, M. A. Mantegazza and G. Bellussi, *Applied Catalysis A: General*, 2001, **221**, 63-72.
116. S. Fukuzumi and K. Ohkubo, *Asian Journal of Organic Chemistry*, 2015, **4**, 836-845.
117. E. Nordell, *Journal (American Water Works Association)*, 1936, **28**, 1480-1487.
118. G. I. Panov, G. A. Sheveleva, A. S. Kharitonov, V. N. Romannikov and L. A. Vostrikova, *Applied Catalysis A: General*, 1992, **82**, 31-36.
119. J. Wang, J. N. Park, X. Y. Wei and C. W. Lee, *Chemical Communications*, 2003, 628-629.
120. R. Gonzalez-Olmos, U. Roland, H. Toufar, F. D. Kopinke and A. Georgi, *Applied Catalysis B: Environmental*, 2009, **89**, 356-364.
121. N. Herron, *J. Coord. Chem.*, 1988, **19**, 25-38.

122. K. T. Dinh, M. M. Sullivan, P. Serna, R. J. Meyer, M. Dincă and Y. Román-Leshkov, *ACS Catalysis*, 2018, **8**, 8306-8313.
123. P. P. Knops-Gerrits and W. A. Goddard, *J. Mol. Catal. A: Chem.*, 2001, **166**, 135-145.
124. K. A. Dubkov, V. I. Sobolev, E. P. Talsi, M. A. Rodkin, N. H. Watkins, A. A. Shteinman and G. I. Panov, *J. Mol. Catal. A: Chem.*, 1997, **123**, 155-161.
125. C. He, Y. Wang, Y. Cheng, C. K. Lambert and R. T. Yang, *Applied Catalysis A: General*, 2009, **368**, 121-126.
126. X. Feng and W. Keith Hall, *Journal of Catalysis*, 1997, **166**, 368-376.
127. F. Gao, *Catalysts*, 2020, **10**, 1-33.
128. S. Brandenberger, O. Kröcher, A. Tissler and R. Althoff, *Applied Catalysis B: Environmental*, 2010, **95**, 348-357.
129. J. A. Morice and L. V. C. Rees, *Trans. Faraday Soc.*, 1968, **64**, 1388-1395.
130. R. Dallabetta, *Journal of Catalysis*, 1976, **41**, 40-45.
131. K. Lázár, O. Pozdnyakova, A. Wootsch and P. Fejes, *Hyperfine Interact.*, 2006, **167**, 779-784.
132. J. Zhang, X. Tang, H. Yi, Q. Yu, Y. Zhang, J. Wei and Y. Yuan, *Applied Catalysis A: General*, 2022, **630**.
133. Y. Lai and G. Veser, *Catalysis Science & Technology*, 2016, **6**, 5440-5452.
134. V. J. Inglezakis and M. D. Loizidou, *Desalination*, 2007, **211**, 238-248.
135. E. Tabor, M. Lemishka, Z. Sobalik, K. Mlekodaj, P. C. Andrikopoulos, J. Dedecek and S. Sklenak, *Communications Chemistry*, 2019, **2**.
136. A. Raj, *Journal of Catalysis*, 1992, **138**, 518-524.
137. G. Wu, F. Hei, N. Guan and L. Li, *Catalysis Science & Technology*, 2013, **3**.
138. L. Li, Q. Shen, J. Li, Z. Hao, Z. P. Xu and G. Q. M. Lu, *Applied Catalysis A: General*, 2008, **344**, 131-141.
139. S. Chaliha and K. G. Bhattacharyya, *Catal. Today*, 2009, **141**, 225-233.
140. S. Haukka, E. L. Lakomaa and T. Suntola, in *Adsorption and its Applications in Industry and Environmental Protection - Vol.I: Applications in Industry*, 1999, ch. 9, pp. 715-750.
141. J. R. A. Sietsma, A. Jos van Dillen, P. E. de Jongh and K. P. de Jong, in *Scientific Bases for the Preparation of Heterogeneous Catalysts*, 2006, ch. 5, pp. 95-102.
142. Y. Ma, S. Han, Q. Wu, L. Zhu, H. Luan, X. Meng and F.-S. Xiao, *Catal. Today*, 2021, **371**, 64-68.
143. R. Martínez-Franco, M. Moliner, J. R. Thogersen and A. Corma, *ChemCatChem*, 2013, **5**, 3316-3323.
144. Y. Yue, H. Liu, P. Yuan, C. Yu and X. Bao, *Scientific Reports*, 2015, **5**.
145. N. Martín, P. N. R. Vennestrøm, J. R. Thøgersen, M. Moliner and A. Corma, *ChemCatChem*, 2017, **9**, 1754-1757.
146. N. Martín, P. N. R. Vennestrøm, J. R. Thøgersen, M. Moliner and A. Corma, *Chemistry - A European Journal*, 2017, **23**, 13404-13414.
147. S. Andonova, S. Tamm, C. Montreuil, C. Lambert and L. Olsson, *Applied Catalysis B: Environmental*, 2016, **180**, 775-787.
148. K. Niu, G. Li, J. Liu and Y. Wei, *Journal of Solid State Chemistry*, 2020, **287**.
149. R. Martínez-Franco, M. Moliner and A. Corma, *Journal of Catalysis*, 2014, **319**, 36-43.
150. R. Martínez-Franco, M. Moliner, C. Franch, A. Kustov and A. Corma, *Applied Catalysis B: Environmental*, 2012, **127**, 273-280.
151. R. Martínez-Franco, M. Moliner, P. Concepcion, J. R. Thogersen and A. Corma, *Journal of Catalysis*, 2014, **314**, 73-82.
152. L. Ren, L. Zhu, C. Yang, Y. Chen, Q. Sun, H. Zhang, C. Li, F. Nawaz, X. Meng and F.-S. Xiao, *Chemical Communications*, 2011, **47**.

153. R. F. Lobo, M. Tsapatsis, C. C. Freyhardt, S. Khodabandeh, P. Wagner, C.-Y. Chen, K. J. Balkus, S. I. Zones and M. E. Davis, *Journal of the American Chemical Society*, 1997, **119**, 8474-8484.
154. E. Yuan, G. Wu, W. Dai, N. Guan and L. Li, *Catalysis Science & Technology*, 2017, **7**, 3036-3044.
155. D. Wierzbicki, A. H. Clark, O. Kröcher, D. Ferri and M. Nachtegaal, *The Journal of Physical Chemistry C*, 2022, **126**, 17510-17519.
156. M. Agote-Arán, I. Lezcano-González, A. G. Greenaway, S. Hayama, S. Díaz-Moreno, A. B. Kroner and A. M. Beale, *Applied Catalysis A: General*, 2019, **570**, 283-291.
157. *Proceedings of the Royal Society of London. Series A, Containing Papers of a Mathematical and Physical Character*, 1997, **88**, 428-438.
158. Y. M. Mos, A. C. Vermeulen, C. J. N. Buisman and J. Weijma, *Geomicrobiol. J.*, 2018, **35**, 511-517.
159. H. P. Klug and L. E. Alexander, John Wiley & Sons, Inc, 2nd ed edn., 1954, pp. 493–494.
160. M. Ma, Y. Zhang, W. Yu, H.-y. Shen, H.-q. Zhang and N. Gu, *Colloids and Surfaces A: Physicochemical and Engineering Aspects*, 2003, **212**, 219-226.
161. J. W. Jermyn, T. J. Johnson, E. F. Vansant and J. H. Lunsford, *The Journal of Physical Chemistry*, 2002, **77**, 2964-2969.
162. G. Berlier, G. Spoto, S. Bordiga, G. Ricchiardi, P. Fisicaro, A. Zecchina, I. Rossetti, E. Selli, L. Forni, E. Giamello and C. Lamberti, *Journal of Catalysis*, 2002, **208**, 64-82.
163. G. Berlier, *Journal of Catalysis*, 2003, **215**, 264-270.
164. G. Mul, J. Pérez-Ramírez, F. Kapteijn and J. A. Moulijn, *Catal. Lett.*, 2002, **80**, 129-138.
165. L. J. Lobree, I.-C. Hwang, J. A. Reimer and A. T. Bell, *Journal of Catalysis*, 1999, **186**, 242-253.
166. G. Mul, M. W. Zandbergen, F. Kapteijn, J. A. Moulijn and J. Pérez-Ramírez, *Catal. Lett.*, 2004, **93**, 113-120.
167. D. A. Bulushev, A. Renken and L. Kiwi-Minsker, *The Journal of Physical Chemistry B*, 2005, **110**, 305-312.
168. D. A. Bulushev, A. Renken and L. Kiwi-Minsker, *The Journal of Physical Chemistry B*, 2006, **110**, 10691-10700.
169. H. Y. Chen, E.-M. El-Malki, X. Wang, R. A. van Santen and W. M. H. Sachtler, *J. Mol. Catal. A: Chem.*, 2000, **162**, 159-174.
170. A. Zecchina, M. Rivallan, G. Berlier, C. Lamberti and G. Ricchiardi, *Phys. Chem. Chem. Phys.*, 2007, **9**, 3483-3499.
171. J. Perezramirez, *Journal of Catalysis*, 2003, **214**, 33-45.
172. A. M. Ferretti, C. Oliva, L. Forni, G. Berlier, A. Zecchina and C. Lamberti, *Journal of Catalysis*, 2002, **208**, 83-88.
173. M.-T. Nechita, G. Berlier, G. Ricchiardi, S. Bordiga and A. Zecchina, *Catal. Lett.*, 2005, **103**, 33-41.
174. K. Miyake, Y. Hirota, K. Ono, Y. Uchida, M. Miyamoto and N. Nishiyama, *New J. Chem.*, 2017, **41**, 2235-2240.
175. J. P. Blitz, John Wiley & Sons New York, 1998, vol. 14, pp. 185-219.
176. S. Dzwigaj, L. Stievano, F. E. Wagner and M. Che, *J. Phys. Chem. Solids*, 2007, **68**, 1885-1891.
177. S. Bordiga, R. Buzzoni, F. Geobaldo, C. Lamberti, E. Giamello, A. Zecchina, G. Leofanti, G. Petrini, G. Tozzola and G. Vlaic, *Journal of Catalysis*, 1996, **158**, 486-501.
178. P. Wu, T. Komatsu and T. Yashima, *Microporous and Mesoporous Materials*, 1998, **20**, 139-147.

179. L. Čapek, V. Kreibich, J. Dědeček, T. Grygar, B. Wichterlová, Z. Sobalík, J. A. Martens, R. Brosius and V. Tokarová, *Microporous and Mesoporous Materials*, 2005, **80**, 279-289.
180. J. Zeng, Y. Wang, F. Diao, L. Qiu and H. Chang, *Catalysis Surveys from Asia*, 2020, **25**, 58-67.
181. M. M. Roessler and E. Salvadori, *Chem Soc Rev*, 2018, **47**, 2534-2553.
182. M. S. Kumar, M. Schwidder, W. Grünert and A. Brückner, *Journal of Catalysis*, 2004, **227**, 384-397.
183. A. Ribera, I. W. C. E. Arends, S. de Vries, J. Pérez-Ramírez and R. A. Sheldon, *Journal of Catalysis*, 2000, **195**, 287-297.
184. P. Gütlich, *Z. Anorg. Allg. Chem.*, 2012, **638**, 15-43.
185. M. H. Engelhard, T. C. Droubay and Y. Du, in *Encyclopedia of Spectroscopy and Spectrometry*, 2017, vol. 4, pp. 716-724.
186. J. Gurgul, K. Łątka, I. Hnat, J. Rynkowski and S. Dzwigaj, *Microporous and Mesoporous Materials*, 2013, **168**, 1-6.
187. T. Yamashita and P. Hayes, *Appl. Surf. Sci.*, 2008, **254**, 2441-2449.
188. T.-C. Lin, G. Seshadri and J. A. Kelber, *Appl. Surf. Sci.*, 1997, **119**, 83-92.
189. M. Descostes, F. Mercier, N. Thromat, C. Beaucaire and M. Gautier-Soyer, *Appl. Surf. Sci.*, 2000, **165**, 288-302.
190. P. C. J. Graat and M. A. J. Somers, *Appl. Surf. Sci.*, 1996, **100-101**, 36-40.
191. T. Schedel-Niedrig, W. Weiss and R. Schlögl, *Physical Review B*, 1995, **52**, 17449-17460.
192. T. Fischer, Iron X-ray photoelectron spectra, iron electron configuration, and other elemental information, https://www.thermofisher.com/uk/en/home/materials-science/learning-center/periodic-table/transition-metal/iron.html).
193. A. Guzmanvargas, *Applied Catalysis B: Environmental*, 2003, **42**, 369-379.
194. I. L. Bull, DE), Xue, Wen-mei (Dayton, NJ, US), Burk, Patrick (Freehold, NJ, US), Boorse, Samuel R. (Skillman, NJ, US), Jaglowski, William M. (West Orange, NJ, US), Koermer, Gerald S. (Basking Ridge, NJ, US), Moini, Ahmad (Princeton, NJ, US), Patchett, Joseph A. (Basking Ridge, NJ, US), Dettling, Joseph C. (Howell, NJ, US), Caudle, Matthew T. (Hamilton, NJ, US), BASF Catalysts LLC (Florham Park, NJ, US), Copper CHA zeolite catalysts, United States, 7601662, 2009
195. J. Han, A. Wang, G. Isapour, H. Härelind, M. Skoglundh, D. Creaser and L. Olsson, *Industrial & Engineering Chemistry Research*, 2021, **60**, 17826-17839.
196. J. Andersen, J. Bailie, J. Casci, H. Chen, J. Fedeyko, R. Foo and R. Rajaram, *International Patent, 2008*, WO/2008/132452.
197. A. M. Beale, F. Gao, I. Lezcano-Gonzalez, C. H. F. Peden and J. Szanyi, *Chem. Soc. Rev.*, 2015, **44**, 7371-7405.
198. F. Gao, J. H. Kwak, J. Szanyi and C. H. F. Peden, *Top. Catal.*, 2013, **56**, 1441-1459.
199. D. E. Doronkin, A. Y. Stakheev, A. V. Kucherov, N. N. Tolkachev, M. Kustova, M. Høj, G. N. Baeva, G. O. Bragina, P. Gabrielsson, I. Gekas and S. Dahl, *Top. Catal.*, 2009, **52**, 1728-1733.
200. M. Høj, M. J. Beier, J.-D. Grunwaldt and S. Dahl, *Applied Catalysis B: Environmental*, 2009, **93**, 166-176.
201. L. Ma, H. Chang, S. Yang, L. Chen, L. Fu and J. Li, *Chem. Eng. J.*, 2012, **209**, 652-660.
202. H. Liu, J. Wang, T. Yu, S. Fan and M. Shen, *Catal. Sci. Technol.*, 2014, **4**, 1350-1356.
203. M. Devadas, O. Krocher, M. Elsener, A. Wokaun, N. Soger, M. Pfeifer, Y. Demel and L. Mussmann, *Applied Catalysis B: Environmental*, 2006, **67**, 187-196.
204. R. Villamaina, I. Nova, E. Tronconi, T. Maunula and M. Keenan, *Emission Control Science and Technology*, 2019, **5**, 290-296.

205. L. Olsson, B. Westerberg, H. Persson, E. Fridell, M. Skoglundh and B. Andersson, *The Journal of Physical Chemistry B*, 1999, **103**, 10433-10439.
206. P. S. Metkar, N. Salazar, R. Muncrief, V. Balakotaiah and M. P. Harold, *Applied Catalysis B: Environmental*, 2011, **104**, 110-126.
207. A. Grossale, I. Nova, E. Tronconi, D. Chatterjee and M. Weibel, *Journal of Catalysis*, 2008, **256**, 312-322.
208. M. P. Ruggeri, T. Selleri, M. Colombo, I. Nova and E. Tronconi, *Journal of Catalysis*, 2015, **328**, 258-269.
209. R. Schmidt, M. D. Amiridis, J. A. Dumesic, L. M. Zelewski and W. S. Millman, *The Journal of Physical Chemistry*, 2002, **96**, 8142-8149.
210. G. Centi and S. Perathoner, *Catal. Today*, 1996, **29**, 117-122.
211. J. H. Kwak, J. H. Lee, S. D. Burton, A. S. Lipton, C. H. F. Peden and J. Szanyi, *Angewandte Chemie International Edition*, 2013, **52**, 9985-9989.
212. M. Iwasaki, K. Yamazaki and H. Shinjoh, *Applied Catalysis A: General*, 2009, **366**, 84-92.
213. A. Grossale, I. Nova and E. Tronconi, *Journal of Catalysis*, 2009, **265**, 141-147.
214. G. Delahay, M. Mauvezin, B. Coq and S. Kieger, *Journal of Catalysis*, 2001, **202**, 156-162.
215. T. C. Brüggemann and F. J. Keil, *The Journal of Physical Chemistry C*, 2011, **115**, 23854-23870.
216. N. Apostolescu, B. Geiger, K. Hizbullah, M. Jan, S. Kureti, D. Reichert, F. Schott and W. Weisweiler, *Applied Catalysis B: Environmental*, 2006, **62**, 104-114.
217. A. Boubnov, H. W. Carvalho, D. E. Doronkin, T. Gunter, E. Gallo, A. J. Atkins, C. R. Jacob and J. D. Grunwaldt, *J Am Chem Soc*, 2014, **136**, 13006-13015.
218. F. Gao, Y. Wang, M. Kollár, N. M. Washton, J. Szanyi and C. H. F. Peden, *Catal. Today*, 2015, **258**, 347-358.
219. R. Q. Long and R. T. Yang, *Catal. Lett.*, 2001, **74**, 201-205.
220. C. Hauser and J. Lindsay, *The Journal of Organic Chemistry*, 1956, **21**, 382-383.

Chapter 2 . Synthesis of Fe-SSZ-13 using a ferrocene-based structure directing agent.

2.1 Introduction

The earliest literature references for Fe-SSZ-13 date back to 2012 when Yang et al.[1] used Fe-SSZ-13 to compare against Cu counterparts for SCR light-off tests. Later that year Narula et al.[2] also studied the SCR performance of both Cu/Fe-SSZ-13 as well as bimetallic MCu-SSZ-13 (M is either Fe, Sc, La or In). In addition to SCR performance, spectroscopic studies of the catalysts were also performed, they concluded that CuFe-SSZ-13 performed best in fresh and hydrothermally aged samples. Gao et al. later studied Fe-SSZ-13 more extensively, investigating Fe loading effect,[3, 4] hydrothermal aging effects[5-7] and also conducted kinetic comparisons of Cu-SSZ-13 against Fe-SSZ-13.[8] In these examples Fe-SSZ-13 was prepared by ion exchange as well as impregnation and one-pot hydrothermal methods. These methods generally resulted in a material with a wide distribution of Fe species. In the case of ion-exchange the wide distribution of species formed is due to Fe reactivity in aqueous solutions. Fe favours the formation of large bulky species in solutions such as FeOOH,[9, 10] these species cannot diffuse easily into small pore zeolites with pore openings of around 0.4 nm,[11] resulting in the formation of surface Fe_XO_Y. The ion-exchange method can be refined to favour monomeric Fe^{2+} species by using Fe^{2+} salts and performing the ion exchange at low pH ~ 3.0 at elevated temperature ~ 80 °C, under a flow of N_2 however it does not completely prevent the formation of other species.[3] Yin et al.[12] compared ion exchanged, impregnated and one pot Fe-SSZ-13, they showed the impregnated sample performed the best. However, the impregnation method produced a heterogenous distribution of Fe species.

For one-pot methods that use Fe salts directly in the synthesis, aluminium and silicon precursors require highly basic conditions to form aluminosilicates, under these conditions Fe will form $Fe(OH)_3$ and likely lead to the presence of Fe_xO_y species once the zeolite is activated.[13] The order of addition when making the zeolite gel with Fe salts has been shown to improve the number of active iron species in the final material.[13] An alternative one-pot method is to use metal complexes as template for the zeolite and a method of introducing an active metal ion in the zeolite. Metal complexes have been used on their own or with an

SDA in a dual template approach. There are few examples in the literature of using Fe complexes as templates for Fe-SSZ-13 synthesis. This is due to the lower stability constants for Fe^{2+} and Fe^{3+} ions with ligands that could be used as templates.[14] According to the Irving-Williams, series divalent first row transition metals increase in stability in the following sequence Mn(II) < Fe(II) < Co(II) < Ni(II) < Cu(II) > Zn(II). There are three main explanations for the series: 1) decrease in ionic radius from Mn to Zn, 2) crystal field stabilisation energy increasing from Mn to Zn and 3) Jahn-Teller effects in complexes.[15] This low complex stability and highly basic conditions make the use of Fe complexes as templates very difficult. Fe-EDTA has been previously used to synthesise Fe-ZSM5[16] and Fe polyamine complexes have been successfully used for the synthesis of silico-alumino-posphate (SAPO). Fe-SAPO-34 has the same CHA topology as SSZ-13 and was prepared using a range of linear polyamines,[17] however these are formed under neutral or weak acidic conditions that stabilised the Fe complex. To the best of my knowledge, there has been no reported literature of using an Fe complex as structure directing agent in Fe-SSZ-13 synthesis.

This work will detail the work done in synthesising Fe-SSZ-13 made using the FMTMA structure directing agent. The chapter will detail how the route was developed and the characterisation methods used to determine whether the FMTMA OSDA is directing the synthesis.

2.2 Experimental methods

Materials

(Ferrocenylmethyl)trimethylammonium iodide (FMTMA I^-) (99+% purity), AmberSep 900 (OH^-), Iron (II) chloride anhydrous ($FeCl_2$) (99.5 % purity) were purchased from Thermo Fischer, Zeolite USY (CBV 500) sodium form was purchased from Zeolyst, Sodium silicate (Crystal 0079) was purchased from Grace, Sodium hydroxide (NaOH) (99+% purity), Potassium hydroxide (KOH) (85 %) were purchased from Fischer Scientific, N,N,N-trimethyl-1-1-adamantammonium hydroxide (TMAda OH^-) (25.5 wt%) was purchased from a large scale OSDA provider, Tetraethylammonium hydroxide (TEA OH^-) (35 % w/v) was purchased from large scale OSDA provider. Reagents were used as received without any further purification and modification. (Ferrocenylmethyl)trimethylammonium hydroxide (FMTMA OH-) (20 % w/v) was prepared according to the procedure below.

Template ion exchange and concentration

Fresh FMTMA OH was prepared prior to zeolite synthesis. FMTMA I^- (15 g) was dissolved in deionised water (600 mL) at 60 °C. The dissolved solution was mixed with AmberSep 900 (OH^-), shielded from light and left to mix overnight. The liquid was filtered from the AmberSep 900 (OH^-) and concentrated using rotary evaporation (again this whole process was shielded from light). The solution was titrated with hydrochloric acid (0.1 M) to determine concentration. The concentrated solution was titrated periodically, once the solution was determined to be sufficiently concentrated (~ 20 % w/v), rotary evaporation was stopped, and the liquid was stored shielded from light at room temperature.

Zeolite hydrothermal synthesis

Zeolites were prepared using various recipes. In general, a zeolite gel was first prepared by dissolving a base in a given quantity of water, the structure directing agent was added to the basic solution and homogenised under magnetic stirring. Next, aluminium source was added to the solution and mixed until homogenous. Finally, the silica source was added slowly to the mixture, and once more, mixed until the mixture was homogenous. The gel was transferred to a Teflon liner and placed into a stainless-steel autoclave. The autoclave was rotated at 30 rpm, for 48 hours at 150 °C. The solid product was washed by centrifugation at 3800 rpm in 5 min cycles until the supernatant liquid reached a conductivity of below 500 µS, to ensure excess cations are washed from the zeolite. The solid was then dried overnight at 110 °C.

Zeolite calcination

Synthesised zeolites were calcined in either air or nitrogen under the following procedure: zeolites were ground with a mortar and pestle prior to calcination. The temperature of the calcination oven was increased from room temperature to 110 ^oC at 2 ^oC/min, heated to 450 ^oC at 5 ^oC/min and hold at 450 ^oC for 16 h. Next, it was further heated to 550 ^oC at 5 ^oC/min and hold at 550 ^oC for 16 h then the sample was cooled down. For nitrogen calcination the same temperature program was used as for the air, N_2 flow was set to 200 ml/min and the oven was purged with N_2 for 30 mins prior to starting the heating procedure.

2.3 Characterisation and testing

Powder X-Ray diffraction (pXRD)

pXRD data were collected in reflection geometry using a Bruker D2 Cu Kα radiation (λ = 1.5406 Å) over the 5 < 2θ < 50 ° range in 0.02 ° steps. Rietveld refinement of the structure was performed using Topas.[18]

Thermo gravimetric analysis (TGA)

TGA experiments were conducted on an TA Instruments SDT Q600 or Q650 TGA system. The samples were held in an alumina pan, the temperature was increased from room temperature to 900 °C at a heating rate of 10 °C/min under a continuous air flow of 100 mL/min.

Solid state nuclear magnetic resonance (ssNMR)

ssNMR spectra were acquired at a static magnetic field strength of 9.4 T ($\nu_0(^1H)$ = 400 MHz) on a Bruker Avance III console using TopSpin 3.1 software. For ^{13}C, the probe was tuned to 100.64 MHz and referenced to alanine CH_3 at 20.5 ppm. Powdered samples were packed into magic angle spinning (MAS) rotors, with before and after weighing providing the sample mass. The rotors were spun using room-temperature purified compressed air. The total experiment time to acquire these spectra was 59 hours. ssNMR spectra were acquired by Dr Jonathan Bradley at Johnson Matthey's technology centre in Sonning Common.

Ultraviolet visible (UV-Vis) spectroscopy

UV-Vis measurements of the Fe-SSZ-13 samples were performed with an Avantes Avaspec 2048 spectrometer in diffuse reflectance (DR) mode. The samples were measured as powders at ambient conditions in a sample cup of 10 mm diameter and 3 mm depth. The DR UV/Vis spectra are presented in form of the Kubelka-Munk function being defined as F(R) = (1 - R)2/(2 · R) with R = Rs/Rr, where Rs is the reflectance of the sample and Rr is the reflectance of H-SSZ-13. DR-VIS spectra of solid samples were acquired by Dr Veselina Georgieva at Johnson Matthey's technology centre in Sonning Common.

Scanning electron microscopy (SEM)

The samples were analysed using a Zeiss ultra 55 Field emission electron microscope equipped with in-lens Secondary electron and backscattered detectors. Samples were dusted directly onto carbon tape stuck to SEM Stubs. Compositional analysis and low-resolution imaging were conducted at an accelerating voltage of 20 kV, aperture of 30 micron, working distance of 7-8 mm and using standard Secondary electron and standard backscattered electron detectors. High-resolution low-accelerating voltage imaging was conducted at an accelerating voltage of 5 kV, aperture of 20-30 micron, working distance of 3-5 mm and using In-lens Secondary electron and In-lens backscattered electron detectors. SEM images were taken by Dr Emily Brooke at Johnson Matthey's technology centre in Sonning Common.

2.4 Results

The initial strategy used to synthesise chabazite using the FMTMA OSDA was to adapt a known chabazite recipe. The known recipe used the following molar gel composition SiO_2 : 68.0, Al_2O_3 : 1.5, Na_2O : 21.0, OSDA : 3.0, H_2O : 580.0. CBV 500 was used as the aluminium source, the crystallisation conditions were 150 °C for 48 hours and a bomb rotation of 30 rpm. This recipe was progressively modified to develop a viable recipe. The synthesis work progressed through three main iterations: i) direct use of FMTMA I^-/OH^-; ii) K^+ based synthesis with FMTMA OH^-; iii) finally dual template approach. The experiments were generally conducted in groups of four and are named as ZEO(X) A,B,C or D e.g. ZEO1 A. A table of all the synthesis experiments done can be found in the appendix (Appendix i).

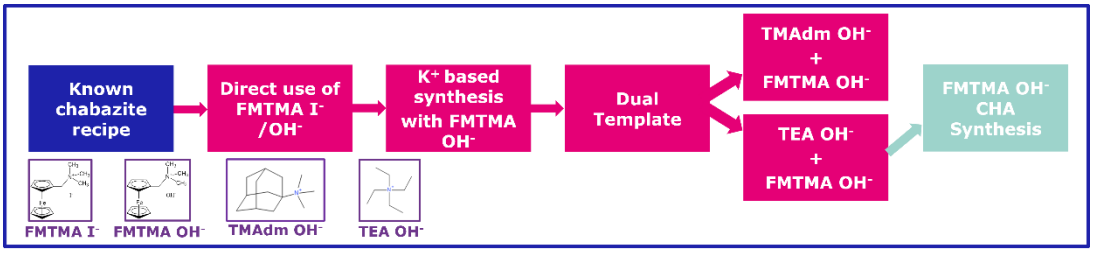

Figure 2-1. Schematic overview of the synthesis approach

2.4.1 Direct use of FMTMA I^-/OH^-

Direct replacement of TMAdmA OH^- in the original gel recipe with either FMTMA I^- or OH^- is the simplest method of using the OSDA. Figure 2-2 shows the pXRD pattern for the product synthesised using either FMTMA I^- or FMTMA OH^- on their own, both synthesis resulted in an impure material. FMTMA OH^- only produces a mixture of mordenite (MOR) and chabazite (CHA) while FMTAM I^- produces a mixture of CHA and gismondine (GIS).

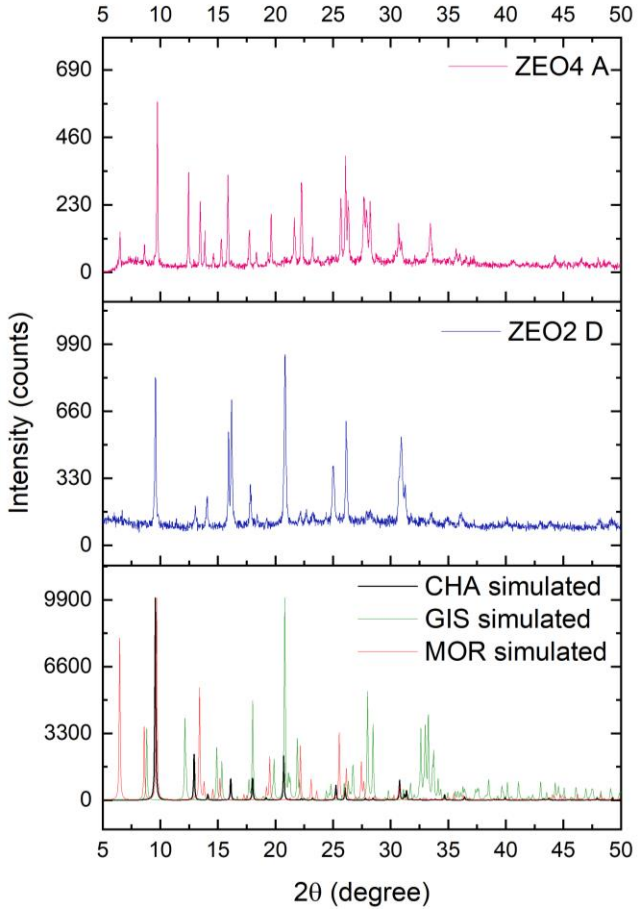

Figure 2-2. pXRD patterns of zeolites samples made using only FMTMA I^- or FMTMA OH^-

The gel composition was altered by increasing the amount of water in the synthesis in an attempt to improve the phase purity at higher ratios of FMTMA OH^- (Figure 2-3). However,

this did not improve the synthesis and using only FMTMA OH^- resulted in a mixture of GIS and MOR.

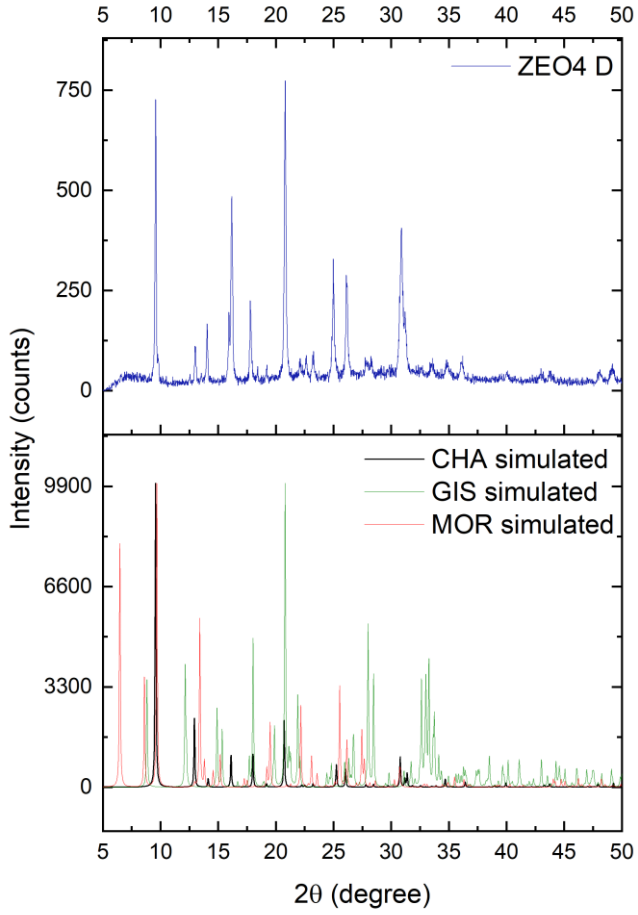

Figure 2-3. pXRD patterns of zeolites sample made using only FMTMA OH^- with increase water content in zeolite gel

Table 2-1. Gel compositions of experiments done using FMTMA I^-/OH^- directly

	Mol							
Sample name	**SiO_2**	**Al_2O_3**	**Na_2O**	**K_2O**	**FMTMA I^- / OH^-**	**H_2O**	**TMAdmA OH^-**	**Products**
ZEO2 D	68.0	1.5	21.0	0.0	**3.0**	580.0	0.0	CHA,GIS
ZEO4 A	68.0	1.5	21.0	0.0	**3.0**	580.0	0.0	CHA,MOR
ZEO4 D	68.0	1.5	21.0	0.0	**3.0**	870.0	0.0	CHA,MOR

Further tests with FMTMA I^- only were not performed due to the poor solubility of the iodide salt in aqueous conditions. Iodide is generally not favoured as a counter ion for OSDAs in zeolite synthesis as it can affect the rate of crystallisation[19, 20] and can even prevent the crystallisation of zeolites according to the Hofmeister Anion Effect.[21]

2.4.1.1 FMTMA OH^- observation

Visible precipitation could be seen in the supply of FMTMA OH^- purchased from the supplier. Subsequent analysis of a filtered sample showed only 1.21 wt % of Fe was present in the sample, much lower than the 10 wt % that was expected. Due to the degradation of FMTMA OH^- further tests used fresh FMTMA OH^- made by the ion exchange of FMTMA I^- with an OH^- ion exchange resin. While producing the fresh FMTMA OH^- it was discovered that FMTMA is photosensitive and when exposed to light and degrades rapidly darkening in colour and forming a visible precipitate (Figure 2-4). Therefore, attempts were made to shield FMTMA OH^- from lights at all times during the ion-exchange process and later zeolite synthesis. The photodecomposition of ferrocene derivatives has previously been studied,[22-24] while the mechanism will vary depending on the derivative the initial step is the dissociation of the Fe^{2+} and the cyclopentadienyl rings. These cyclopentadienyl rings will then react further depending on the starting derivative.

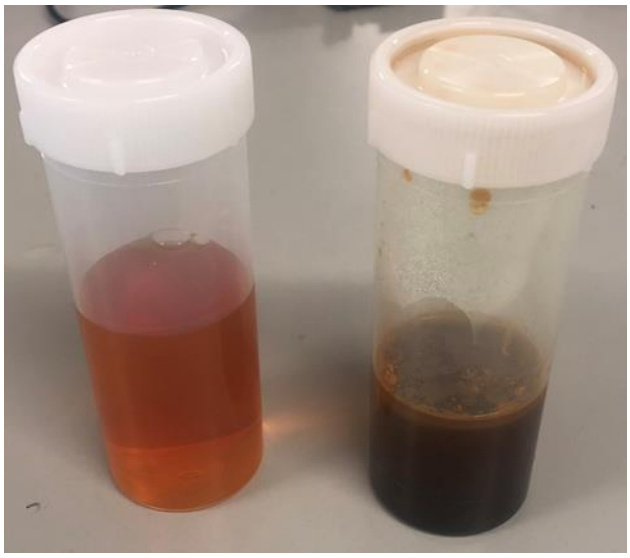

Figure 2-4. Samples of freshly made FMTMA OH^- that were either shielded from light (left) or exposed to light (right). Both samples used the same starting fresh FMTMA OH^- and were examined after 30 mins

2.4.2 K^+ based synthesis with FMTMA OH^-

Partial and complete replacement of sodium with potassium cations in the synthesis gel has been shown to aid in the formation of CHA.[25] With this in consideration, using FMTMA OH^- with only potassium in the gel was attempted as it should prevent the formation of competing phases when high concentrations of FMTMA OH^- are used. Freshly made FMTMA OH^- that was shielded from light was used for the next set of experiments. Initially, dilute solutions of FMTMA OH^- were used while a method to concentrate the solution shielded from light was developed, hence why the H_2O ratio in the gel is much higher than desired.

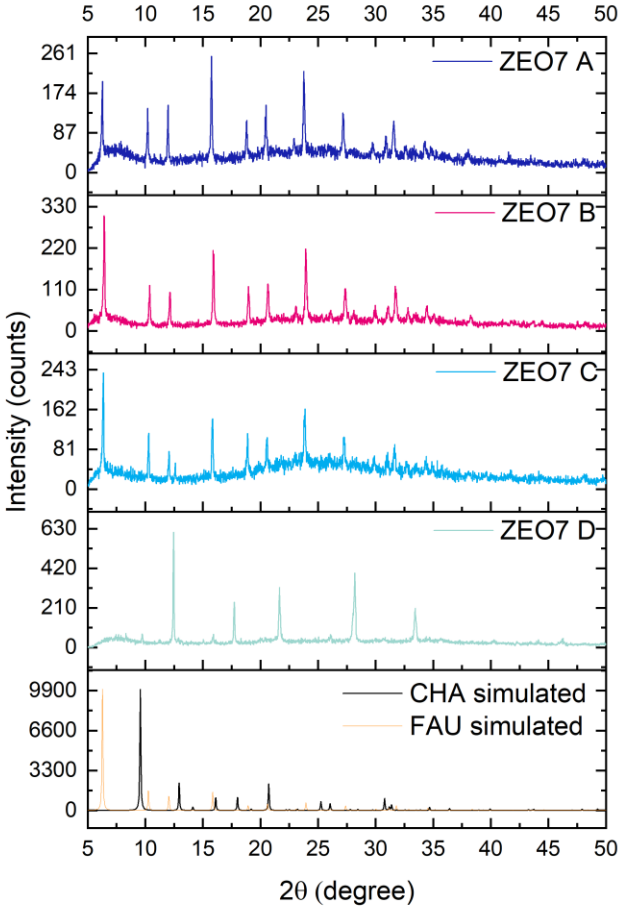

Figure 2-5. pXRD patterns of zeolites samples made with varying ratios of fresh FMTAM OH^- and K_2O

The ZEO7 (Figure 2-5) series of samples used a dilute solution of FMTMA OH^- (~0.8 wt%) and various ratios of Na and K, the molar gel compositions can be seen in Table 2-2. Samples A, B and C were made with KOH, the pXRD of these samples show unconverted FAU indicating the amount of KOH used is not enough to dissolve the starting FAU. Sample D was made with NaOH only and produced an unknown phase.

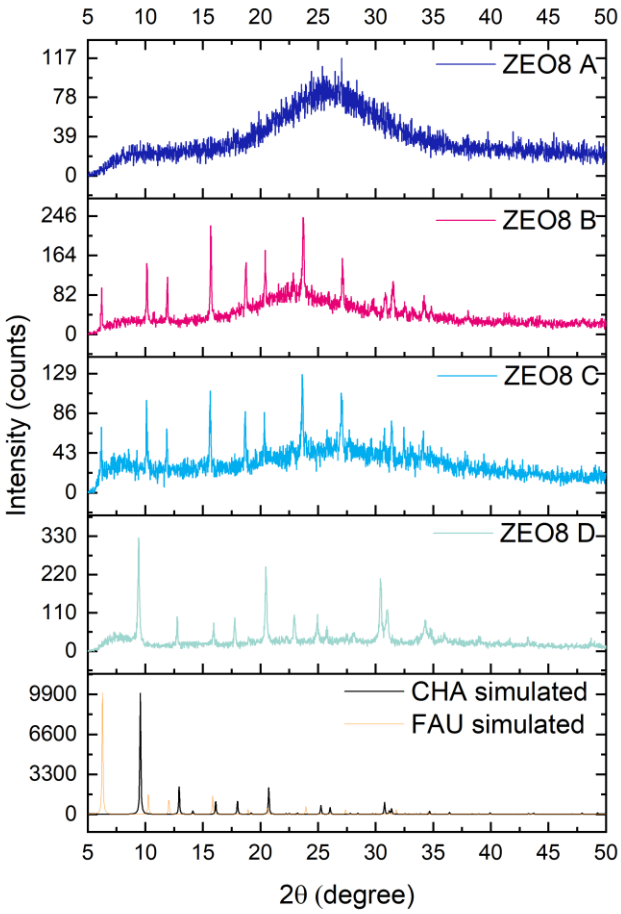

Figure 2-6. pXRD patterns of zeolites samples made with varying ratios of fresh FMTAM OH^- and K_2O

The previous set of samples showed the amount of KOH used was not sufficient to dissolve the starting FAU. For the ZEO8 (Figure 2-6) series of experiment, the quantity of KOH was increased to aid the dissolution of the starting FAU, gel compositions can be seen in Table 2-2. Samples A to D were synthesised with increasing amounts of KOH, pXRD patterns show sample A is completely amorphous while unconverted FAU and an amorphous component is seen in samples B and C. It is not clear why sample A was amorphous if it contained the lowest amount of KOH, however the conditions are very dilute so a longer crystallisation time may result in a crystalline product. Sample D with the highest quantity of KOH used in the

synthesis resulted in a pXRD pattern consisting of CHA, however the sample was poorly crystalline.

Table 2-2. Gel compositions of K+ based synthesis with FMTMA OH^-

	Mol							
Sample name	**SiO_2**	**Al_2O_3**	**Na_2O**	**K_2O**	**FMTMA OH^-**	**H_2O**	**TMAdmA OH^-**	**Products**
ZEO7 A	68.0	1.5	0.0	21.0	**3.0**	6500.0	0.0	FAU
ZEO7 B	68.0	1.5	0.0	21.0	**1.5**	3600.0	1.5	FAU
ZEO7 C	68.0	1.5	0.0	21.0	**3.0**	6400.0	0.0	FAU
ZEO7 D	68.0	1.5	21.0	0.00	**3.0**	6500.0	0.0	Unknown
ZEO8 A	68.0	1.5	0.0	21.0	**3.0**	580.0	0.0	Amorphous
ZEO8 B	68.0	1.5	0.0	30.0	**3.0**	6400.0	0.0	Amorphous,FAU
ZEO8 C	68.0	1.5	0.0	40.0	**3.0**	6400.0	0.0	Amorphous,FAU
ZEO8 D	68.0	1.5	0.0	50.0	**3.0**	6400.0	0.0	Low crys CHA

Further compositional analysis by XRF of this sample (Table 2-3) showed a Si/Al ratio (SAR) of ~ 10 and a high Fe content of around ~ 12.6 wt %. The compositional data from this sample is unusual as it indicates the sample is not charge balanced, there are a lot more cations in the sample than can be accommodated by the Al present in the sample. It is not completely understood why this is the case, the samples were washed according to the procedure outlined in the method, so soluble species should have been washed away. Amorphous material or material deposited on the surface of the zeolite could account for the unusual result as observed by SEM Figure 2-8.

Table 2-3. XRF analysis of sample ZEO8 D

Sample	K (wt %)	Al (wt %)	Si (wt %)	Fe (wt %)
ZEO8 D	8.33	3.62	18.93	12.59

TGA (Figure 2-7) of this sample showed a 10 % weight loss between 200 °C to 400 °C associated with the FMTMA OH^-. SEM images (Figure 2-8) of the sample show small poorly defined crystals in addition to large particles.

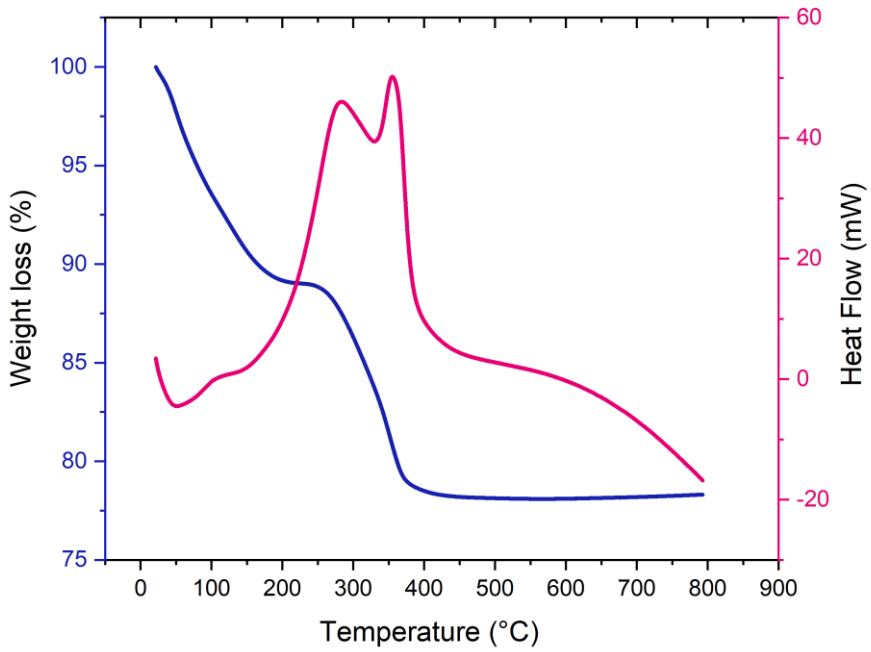

Figure 2-7. TGA of sample ZEO8 D

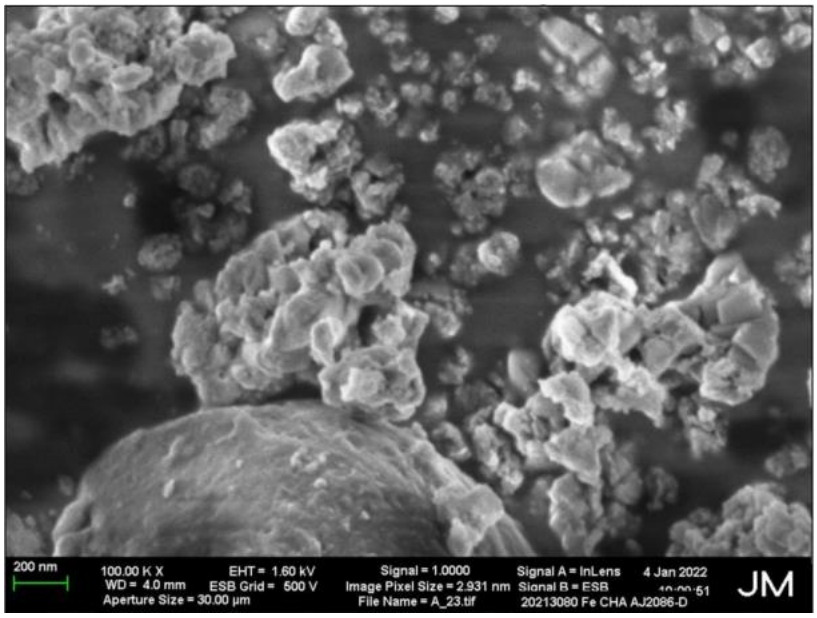

Figure 2-8. SEM image of sample ZEO8 D

Eleven attempts were made to repeat the synthesis and to increase the crystallinity of the sample by increasing the crystallisation time and refining the potassium content of the synthesis gel. However, these all failed to produce a chabazite and resulted in the synthesis of a potassium silicate phase (Appendix iii). A few pXRD examples of these results can be found in the Appendix (96 h crystallisation time - Appendix vii, direct repeat of ZEO8 D - Appendix viii and varied potassium content - Appendix ix)

2.4.3 Dual template approach

A dual template strategy was also adopted after FMTMA only synthesis did not produce a phase pure chabazite material. Experiments were conducted with TMAdmA OH^- or TEA OH^- as a co-template with FMTMA I^-/OH^- to aid the crystallisation of chabazite.

2.4.3.1 Dual template synthesis TMAdmA OH^- with FMTMA I^- or FMTMA OH^-

FMTMA I^-

Figure 2-9 shows the pXRD patterns of the attempted synthesis of chabazite using increasing ratio of FMTMA I^- with TMAdmA OH^-, the overall OSDA molar ratio was kept constant at 3.0, however the OH^- content is changing within the ZEO1 series of experiments. The pXRD pattern shows the dominate phase is CHA however additional reflection was seen relating to unconverted FAU as well as GIS and MOR. Higher ratios of FMTMA I and TMAdmA OH^- (Appendix ii) were also attempted however these also resulted in the same mixtures of phases.

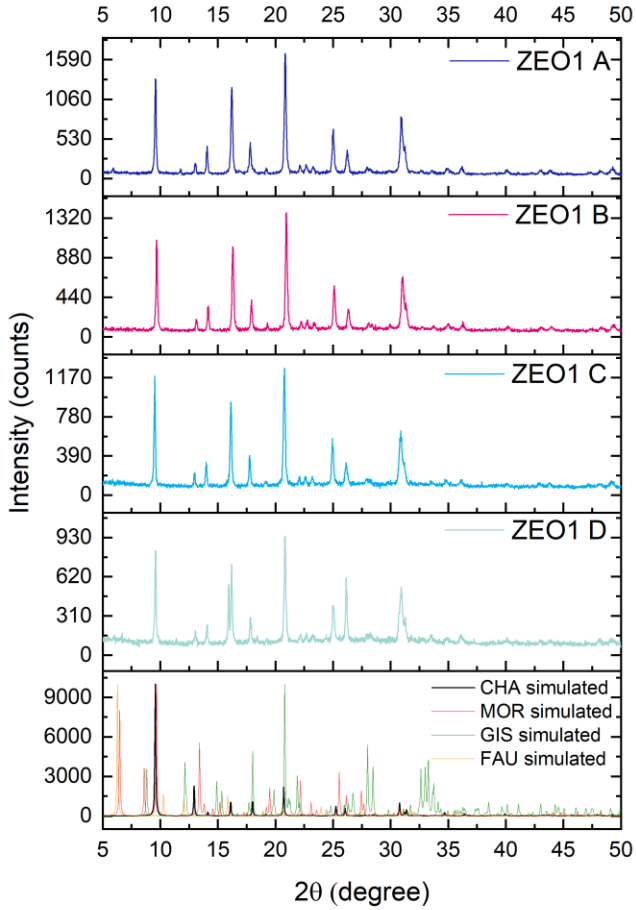

Figure 2-9 pXRD patterns of chabazite synthesis with varying ratios of TMAdaA OH^- and FMTAM I^-

Table 2-4. Molar gel compositions of ZEO1 series of experiments

	Mol							
Sample name	**SiO_2**	**Al_2O_3**	**Na_2O**	**K_2O**	**FMTMA I^-/ OH^-**	**H_2O**	**TMAdmA OH^-/TEA OH^-**	**Products**
ZEO1 A	68.0	1.5	21.0	0.0	**0.5**	580.0	2.5	FAU,CHA,GIS,MOR
ZEO1 B	68.0	1.5	21.0	0.0	**1.0**	580.0	2.0	FAU,CHA,GIS,MOR
ZEO1 C	68.0	1.5	21.0	0.0	**1.5**	580.0	1.5	FAU,CHA,GIS,MOR
ZEO1 D	68.0	1.5	21.0	0.0	**2.0**	580.0	1.0	FAU,CHA,GIS,MOR

FMTMA OH^-

Using the hydroxide salt instead the iodide of FMTMA could aid in the crystallisation and improve the dissolution of the starting FAU. pXRD spectra for these synthesis (Figure 2-10) show that with increasing ratios of FMTMA OH^- GIS and MOR are formed. While at lower ratios FMTMA OH^- to TMAda OH^- a pure CHA is formed, however it is likely that the TMAda OH^- is directing the phase in these synthesis. Compositional analysis by XRF for the ZEO3 series of samples showed a general increase in Fe content in line with the increasing amount of FMTMA OH^- used in the synthesis and all samples had a SAR of around 20.

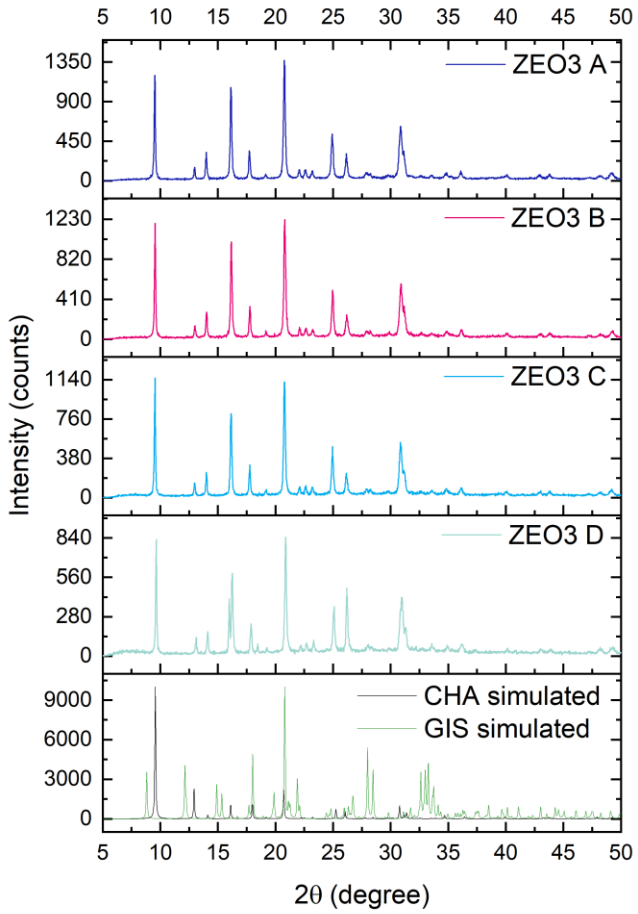

Figure 2-10 pXRD patterns of chabazite synthesis with varying ratios of TMAda and FMTAM OH^-

Table. 2-5. Molar gel compositions of ZEO3 series of experiments

	Mol							
Sample name	**SiO_2**	**Al_2O_3**	**Na_2O**	**K_2O**	**FMTMA I^-/ OH^-**	**H_2O**	**TMAdm OH^-**	**Products**

							/TEA OH^-	
ZEO3 A	68.0	1.5	21.0	0.0	**0.5**	580.0	2.5	CHA
ZEO3 B	68.0	1.5	21.0	0.0	**1.0**	580.0	2.0	CHA
ZEO3 C	68.0	1.5	21.0	0.0	**1.5**	580.0	1.5	CHA
ZEO3 D	68.0	1.5	21.0	0.0	**2.0**	580.0	1.0	CHA,GIS

Sample ZEO3 C was subjected to TGA as it was phase pure sample made with the highest quantity of FMTMA OH^-. TGA (Figure 2-11) of this sample showed an 8 % weight loss at 400 °C, typically a 20 % weight loss is expected from a zeolite made using an OSDA.

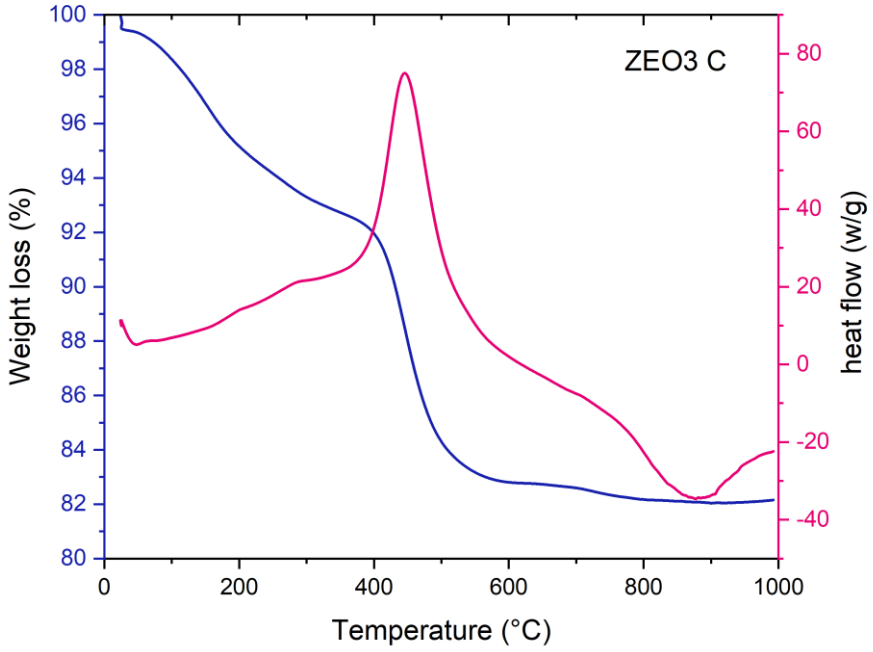

Figure 2-11 TGA of sample ZEO3 C

DR UV-Vis (Figure 2-12) showed a clean spectra with a main peak around 250 nm, this suggests isolated Fe species are present in the sample however, there does not appear to be any significant bands relating to FMTMA OH^- present in the samples. These initial results suggest the FMTMA molecule is not directing the synthesis towards the CHA structure under the conditions used and further development of the synthesis conditions are needed.

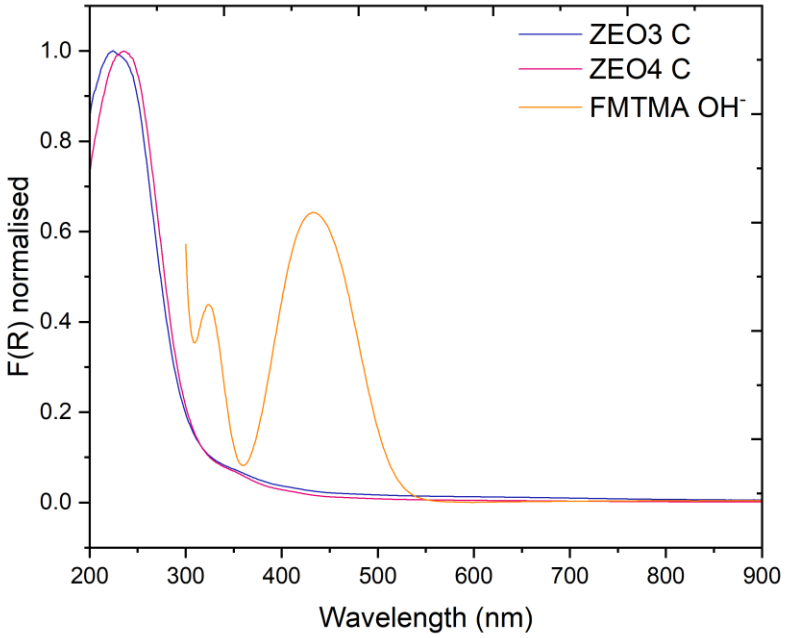

Figure 2-12 DR UV-Vis of sample ZEO3 C, ZEO4 C and UV-Vis of FMTMA OH^- spectra below 300 nm omitted due to noise

2.4.3.2 Dual template with K^+

As previously mentioned in section 2.4.2, partial or complete replacement of sodium with potassium cations has been shown to aid in the formation of CHA.[25] These experiments aimed to use high ratios of FMTMA OH^- to TMAdmA OH^- using KOH has the mineralising agent to prevent the formation of competing phases. Both partial and complete substitution of sodium with potassium was attempted using the existing crystallisation conditions, 150 °C for 48 hours and a bomb rotation of 30 rpm. However, in both cases the production of a phase pure chabazite using only the FMTAM OH^- was not successful.

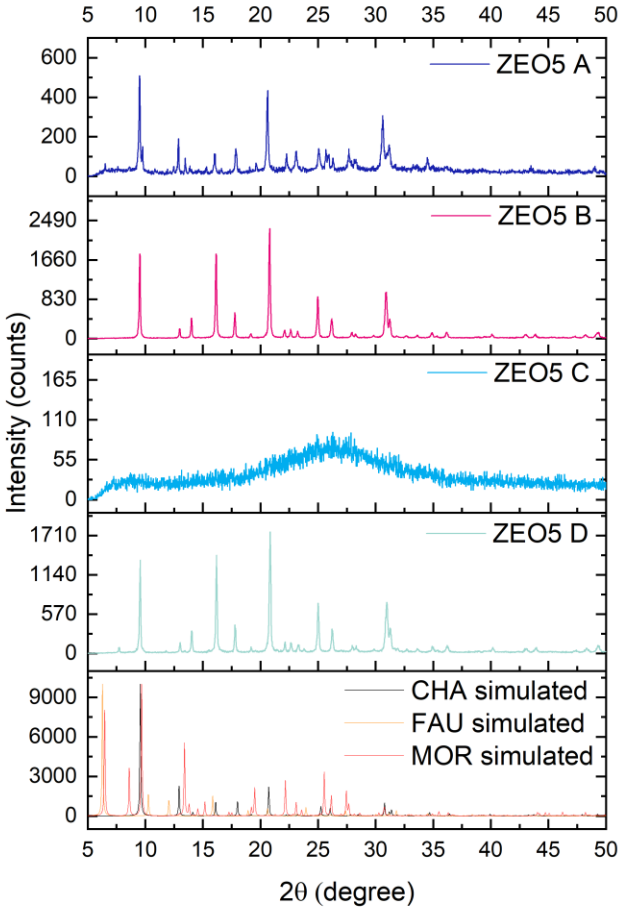

Figure 2-13. pXRD patterns of chabazite synthesis with varying ratios of FMTAM OH^- TMAdmA OH^- and K_2O

	Mol							
Sample name	**SiO_2**	**Al_2O_3**	**Na_2O**	**K_2O**	**FMTMA I^-/ OH^-**	**H_2O**	**TMAdm OH^- /TEA OH^-**	**Products**
ZEO5 A	68.0	1.5	6.0	15.0	**3.0**	870.0	0.0	FAU,CHA,MOR
ZEO5 B	68.0	1.5	6.0	15.0	**0.0**	870.0	3.0	CHA
ZEO5 C	68.0	1.5	0.0	21.0	**3.0**	870.0	0.0	Amorphous
ZEO5 D	68.0	1.5	0.0	21.0	**0.0**	870.0	3.0	CHA,FAU

Figure 2-13 shows the resulting pXRD patterns for the partial and complete replacement of Na with K with only FMTMA OH^- or only TMAdmA OH^-. TMAdmA OH^- only syntheses were also attempted in parallel to determine if the gel composition used was viable to produce phase pure chabazite. Samples ZEO5 A and B partially replace Na^+ with K^+, while C and D completely replace Na^+ with K^+. Samples A and B produced a mixed phase product containing

un-converted FAU, MOR and CHA for the FMTMA OH^- sample while phase pure CHA was produced for the TMAdmA OH^- sample. This indicates the FMTMA OH^- template itself is causing other phases to crystalise rather than other components of the gel.

Samples ZEO5 C and D were made with the total substitution of sodium with potassium by using a 40 wt% sodium free colloidal silica in the synthesis. A small MOR impurity can be seen in the TMAdmA OH^- only synthesis, yet the FMTMA OH^- only synthesis is amorphous. This suggests either the template is not directing the synthesis under these conditions or the kinetics of crystallisation is different and the crystallisation time should be increased . This suggests Na^+ ions are required to initiate crystallisation using FMTMA OH^- only as OSDA, again this is more evidence the FMTMA OH^- molecule is not a strong structure directing agent.

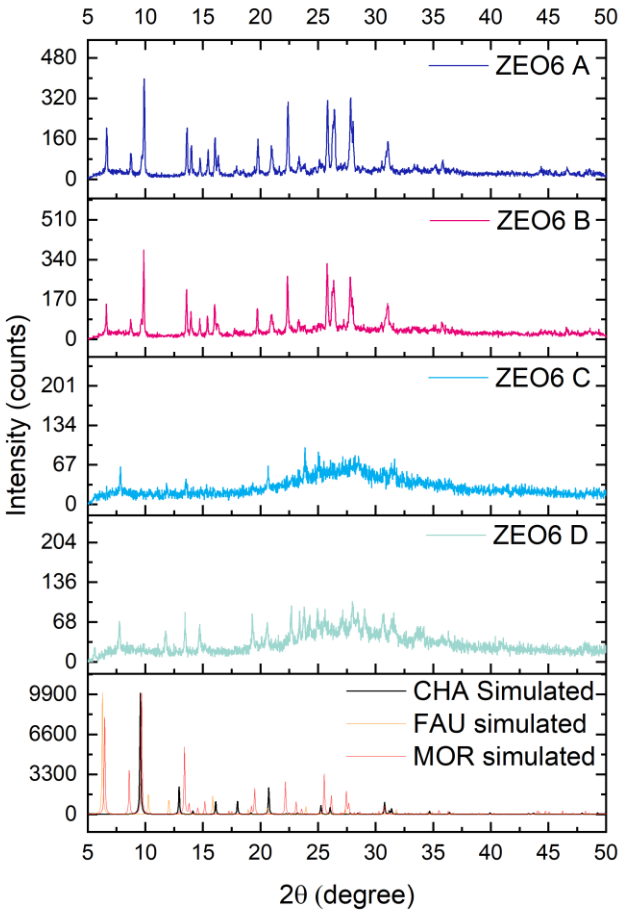

Figure 2-14 Chabazite synthesis with varying ratios of FMTAM OH^- and K_2O including 5 wt% as made CHA seeds

The ZEO5 series of synthesis were attempted again (ZEO6), this time including 5 wt% of as made CHA seeds to encourage the crystallisation of CHA. The inclusion of CHA seeds in the synthesis did not have the desired effect as MOR was produced in the samples (A and B) that partially replaced Na^+ with K^+ while the samples that completely replaced Na^+ with K^+ (C and D) were mostly amorphous with small amounts of mordenite.

2.4.4 TEA OH^- based synthesis with FMTMA OH^-

Previous experiments have indicated that FMTMA OH^- is not directing the synthesis when used with TMAdmA OH^- in the synthesis. TMAda OH^- is a very strong structure directing agent for the synthesis of SSZ-13 as it has a very strong host-guest interaction in the *cha* cage[11] and it is likely dominating the in directing to SSZ-13. TEA OH^- has also been shown to direct the formation of SSZ-13[26] a single TEA OH^- molecule has been shown to occupy the *cha* cage[27] however due to its flexibility it is likely that its host guest interaction is not as strong compared to TMAdmA OH^-. As TEA OH^- is less directing replacing TMAdmA OH^- with TEA OH^- could encourage the formation of SSZ-13 with FMTMA OH^-.

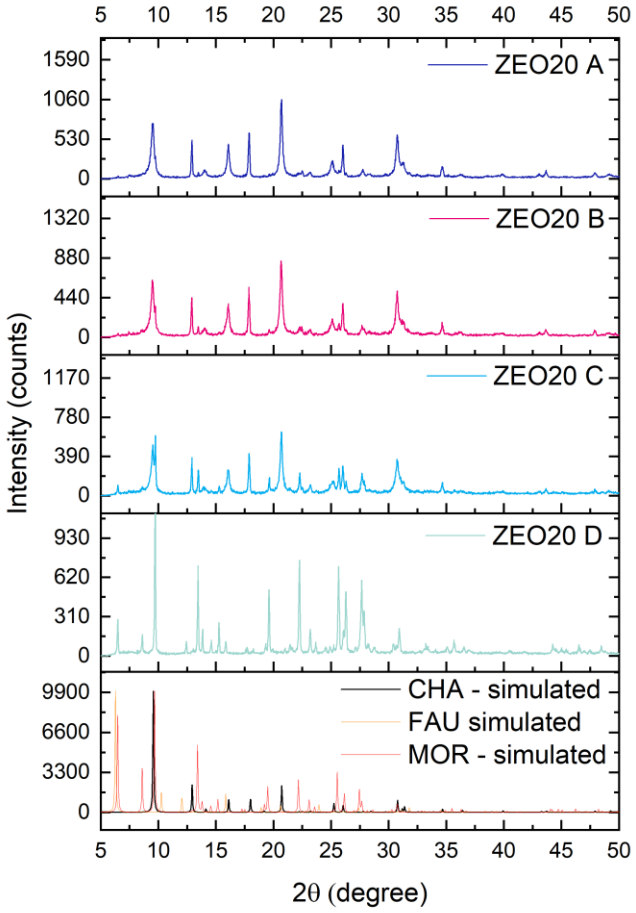

Figure 2-15. pXRD patterns of SSZ-13 synthesised with varying ratios of TEA OH^- and FMTMA OH^-

Table 2-6. Zeolite gel composition used for the synthesis in the ZEO20 series of samples.

	Mol							
Sample name	**SiO_2**	**Al_2O_3**	**Na_2O**	**K_2O**	**FMTMA OH^-**	**H_2O**	**TMAdm OH^- /TEA OH^-**	**Products**
ZEO20 A	68.0	1.5	21.0	0.0	0.5	660.0	**2.50**	FAU,CHA,MOR
ZEO20 B	68.0	1.5	21.0	0.0	1.0	815.0	**2.00**	CHA
ZEO20 C	68.0	1.5	21.0	0.0	1.5	970.0	**1.50**	Amorphous
ZEO20 D	68.0	1.5	21.0	0.0	2.5	1280.0	**0.50**	CHA,FAU

Experiments with TEA OH^- and FMTMA OH^- (Figure 2-15) show a trend toward the formation of MOR with increasing FMTMA OH^- and a trend towards CHA with increasing TEA OH^-. It is likely that MOR is favoured as these synthesis were Na^+ only synthesis, previous FAU to CHA interconversion studies have suggested K^+ can aid in the formation of CHA.[28] An initial K^+ based synthesis was attempted (Appendix xi) however, all of this series of samples produced the potassium silicate phase that was previously encountered. This is likely due to using a

much higher amount of K^+ than required, which subsequently favours the formation of the potassium silicate (Appendix xi)

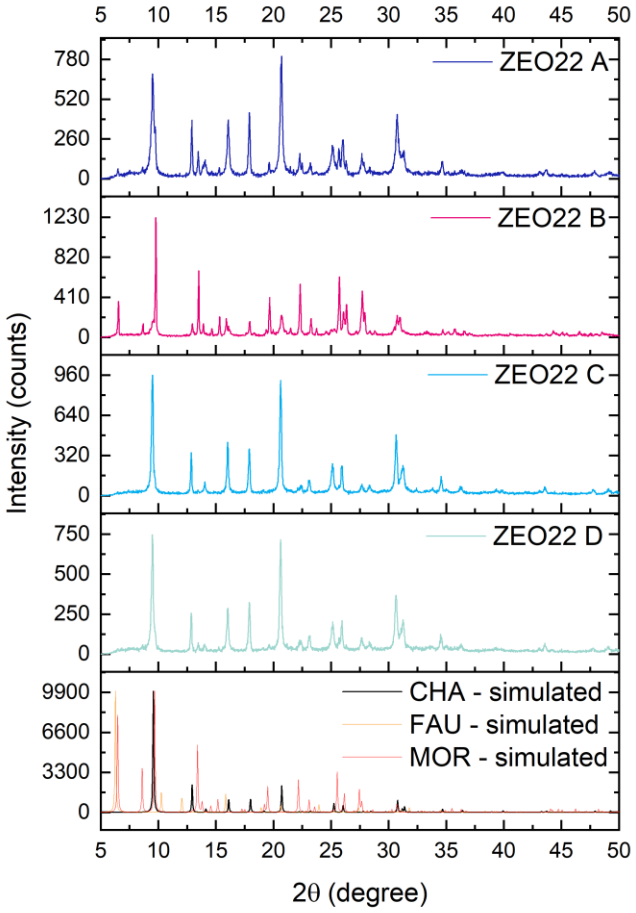

Figure 2-16. pXRD patterns of SSZ-13 synthesised with varying ratios of TEA OH^-, FMTMA OH^- and K^+

Table 2-7. Zeolite gel composition used for the synthesis in the ZEO22 series of samples

	Mol							
Sample name	**SiO_2**	**Al_2O_3**	**Na_2O**	**K_2O**	**FMTMA OH^-**	**H_2O**	**TMAdm OH^- /TEA OH^-**	**Products**
ZEO22 A	68.0	1.5	0.0	20.0	1.50	750.0	**1.5**	FAU,CHA,MOR
ZEO22 B	68.0	1.5	0.0	20.0	2.00	750.0	**1.0**	FAU,CHA,MOR
ZEO22 C	68.0	1.5	0.0	15.0	1.50	750.0	**1.5**	CHA,MOR
ZEO22 D	68.0	1.5	0.0	15.0	2.00	750.0	**1.0**	CHA,MOR

Figure 2-16 shows the pXRD patterns for the synthesis with TEA OH^- and FMTMA OH^- using lower amounts of K^+. These results show that CHA is formed when lower amounts of FMTMA

OH^- are used and that the amount of K^+ should be limited in the synthesis as too much can cause the formation of impurities in the final material.

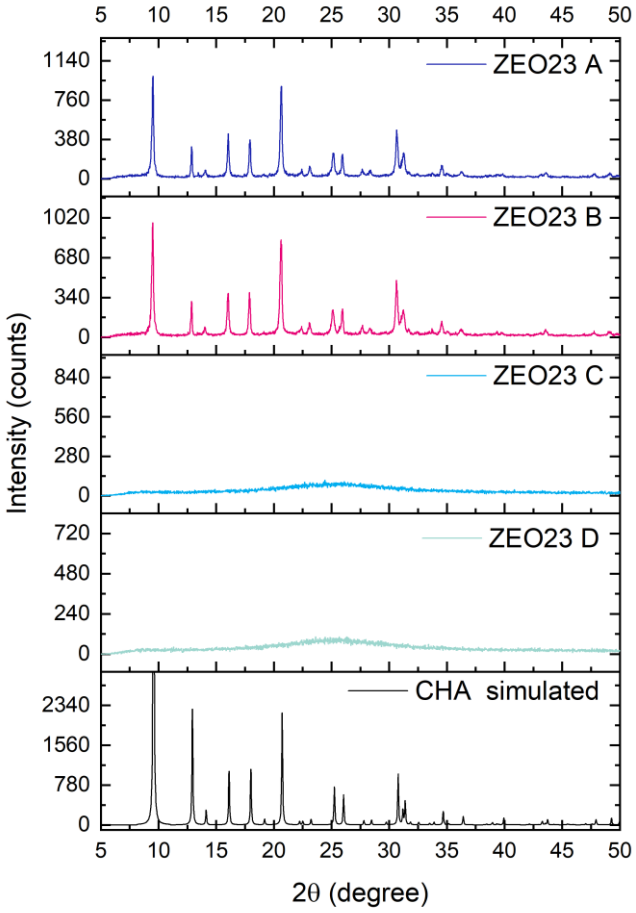

Figure 2-17. pXRD patterns of SSZ-13 synthesised with varying ratios of TEA OH^-, FMTMA OH^- and K+

Table 2-8. Zeolite gel composition used for the synthesis in the ZEO23 series of samples.

	Mol							
Sample name	**SiO_2**	**Al_2O_3**	**Na_2O**	**K_2O**	**FMTMA OH^-**	**H_2O**	**TMAdm OH^- /TEA OH^-**	**Products**
ZEO23 A	68.0	1.5	0.0	15.0	1.5	750.0	**1.5**	CHA,MOR
ZEO23 B	68.0	1.5	0.0	15.0	1.5	750.0	**1.5**	CHA, MOR
ZEO23 C	68.0	1.5	0.0	15.0	2.0	750.0	**1.0**	Amorphous
ZEO23 D	68.0	1.5	0.0	15.0	2.5	750.0	**0.5**	Amorphous

Building on the previous set of samples, the gel composition was refined to increase the amount of FMTMA OH^- used in the synthesis. Figure 2-17 shows that the gel composition of ZEO22 C is reproducible and can produce the CHA phase, while increasing the FMTMA OH^-

beyond 1.5 mol in the gel inhibits the crystallisation of any phase. An additional phase is seen in the pXRD pattern most evident in the peak at ~13.4°, this is consistent with mordenite, although it looks to be the minority phase within the sample.

Further tests were conducted to optimise the conditions, increasing the overall ratio of templates relative to alumina in the gel (Appendix xii), and reducing the temperature of the synthesis from 150 °C to 120 °C (Appendix xiv). However, both changes produced a material with more impurities than the previous experiments.

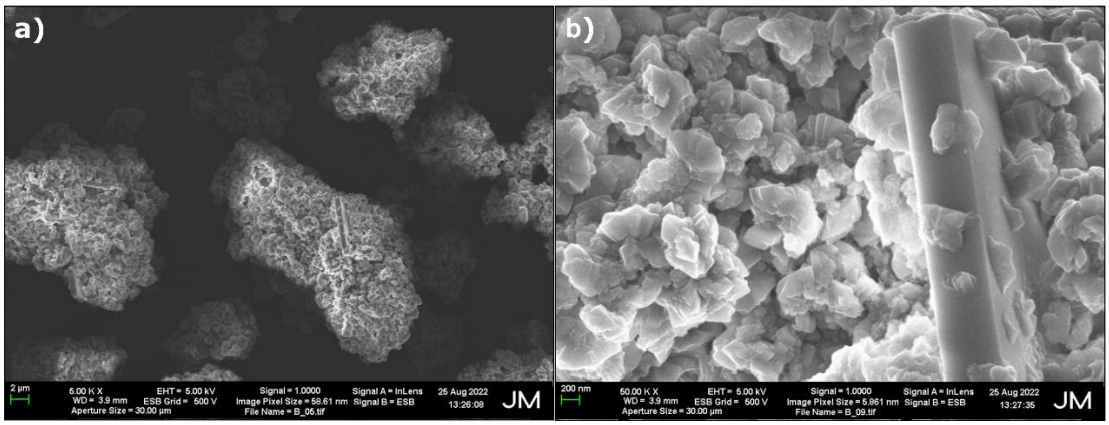

Figure 2-18. a) SEM image of sample ZEO23 A, b) magnified SEM image of ZEO23 A highlighting different crystal morphology.

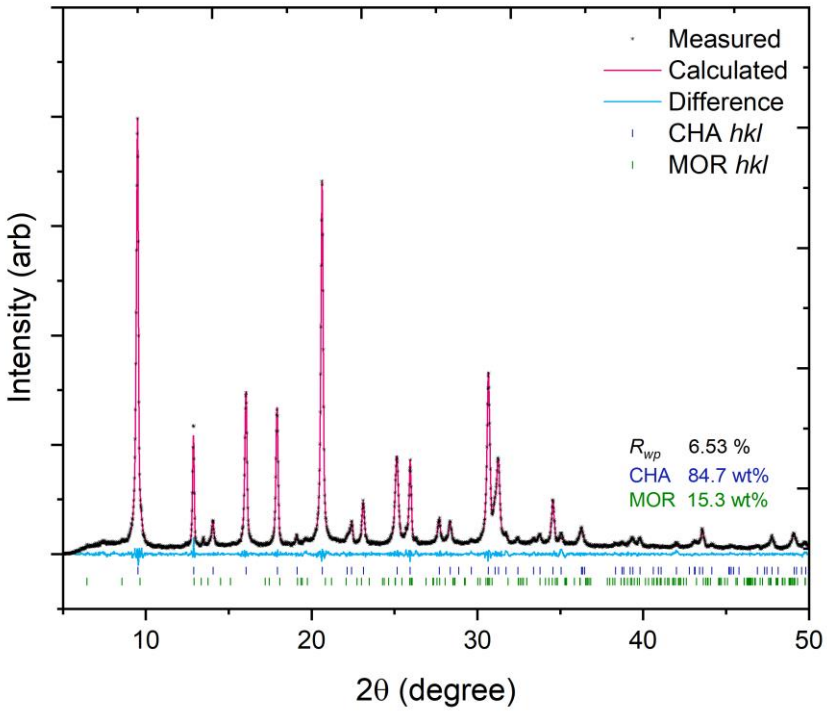

Figure 2-19. pXRD of sample ZEO23 A and subsequent Rietveld refinement.

While it is clear that samples ZEO23-A and B do have MOR impurities, Rietveld refinement of ZEO23 A calculates the MOR impurity to be the minor product at 15.3 wt% of the sample, Rietveld parameters for the calculation can be found in Appendix *xvi*, Fractional atomic coordinates, occupancies, multiplicities, and isotropic displacement parameters for CHA and MOR can be found in Appendix *xvii* and Appendix *xviii* respectively. Further work to refine the conditions did not result in a completely phase pure chabazite. SEM images (Figure 2-18 and Figure *2-19*) of sample ZEO23 A showed the MOR was not acicular in nature and was safe to use for further testing, therefor the gel composition was fixed and a larger quantity of this sample was synthesised for characterisation and catalytic testing.

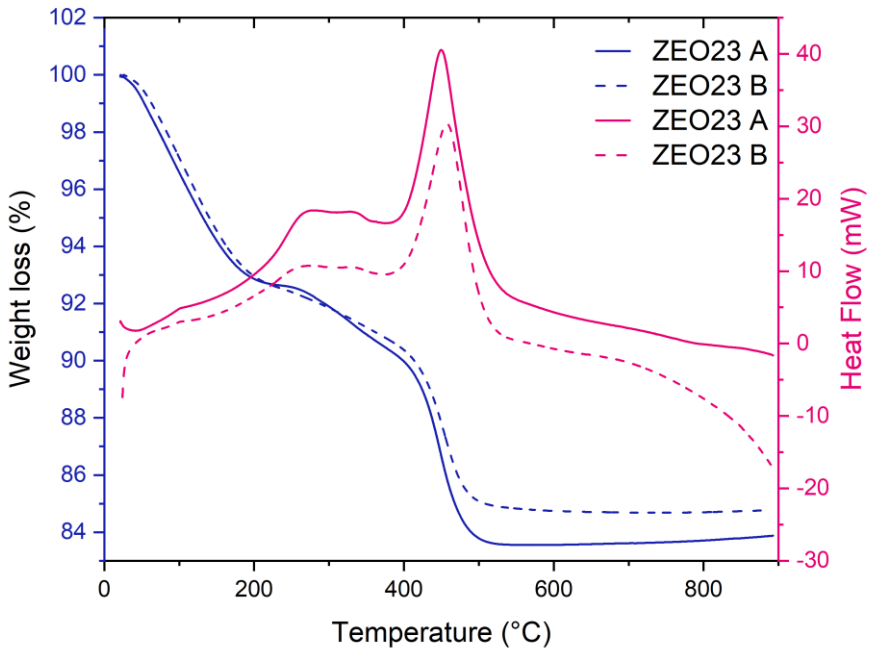

Figure 2-20. TGA-DSC of samples ZEO23 A and B

Table 2-9. Composition of samples ZEO23-A and B determined by XRF

		Na	Al	Si	K	Fe	H_2O/OSDA	SAR
ZEO23 A	Wt%	0.84	4.77	28.94	3.92	3.73	17.89	11.66
	Atomic	1.09	5.27	30.73	2.99	1.99		
	Unit Cell							
	Wt% Oxide	1.13	9.01	61.91	4.72	5.33		
	Oxide	0.54	2.64	30.73	1.49	1.00		
	Unit Cell							
ZEO23 B	Wt%	1.26	4.95	28.73	3.93	3.70	17.43	11.15
	Atomic	1.64	5.47	30.53	3.00	2.82		
	Unit Cell							
	Wt% Oxide	1.70	9.35	61.46	4.73	5.29		
	Oxide	0.82	2.74	30.53	1.50	1.41		
	Unit Cell							

Table 2-10. Table showing the molar composition of samples ZEO23 A and B

	Na	Al	K	Fe	OSDA TGA	Difference assuming 1:1 Al to Fe	Difference assuming 2:1 Al to Fe
ZEO23 A Wt %	0.840	4.770	3.920	3.730	7.000		
ZEO23 A mol	0.037	0.177	0.100	0.067	0.048	-0.074	-0.041
ZEO23 B Wt %	1.260	4.950	3.930	3.700	7.000		
ZEO23 B mol	0.055	0.183	0.101	0.066	0.048	-0.086	-0.053

TGA-DSC analysis of sample ZEO23 A and B (Figure 2-20) shows an initial weight loss of around 8 % to 200 °C and a further 7 % weight loss at 450 °C with a large exotherm, resulting in a total weight loss of 15 %. The two-step weight loss is likely due to an initial loss of water at 200 °C then oxidation of the organic template at 450 °C as seen by the large exotherm at the same temperature. This low weight loss could indicate the crystallisation is not solely driven by the OSDA and the potassium could also be playing a role in templating the synthesis. Compositional analysis by XRF of the two samples (Table 2-9) shows the zeolites have a SAR of around 11.4 and an Fe loading of around 3.7 wt%. The combined water and OSDA wt% are calculated based on the oxide and are broadly in line with the total weight loss from TGA. The XRF data can also be used to calculate the charge balance of the zeolite, that is that all the AlO_3^- sites are counterbalanced by a cation. Assuming the sample has been thoroughly washed and the $FMTMA^+$ ion is intact within the structure, the molar ratio (Table 2-10) for these samples indicate there are more cations then can be counter balanced by AlO_4^- sites. This could indicate that the assumptions that $FMTMA^+$ ion stays intact are wrong and that a portion of the Fe seen by XRF is free Fe.

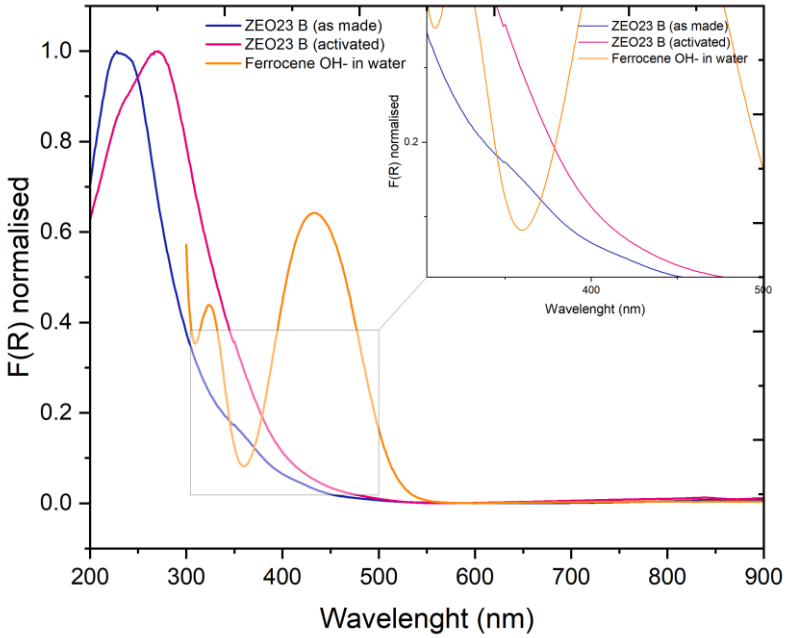

Figure 2-21. DR-UV-Vis of sample ZEO23 B as made and calcined, UV-Vis of FMTMA OH^- in water has also been included (spectra before 300 nm has been omitted due to noise)

DR-UV-Vis of ZEO23-B (as made) shows a single main peak at around 250 nm, although less evident a second signal can be seen at 350 nm which could correspond to FMTMA however this is not conclusive. The spectrum of the calcined sample, ZEO23-B (activated) shows the peak broadens and while the signal at 250 nm can still be seen it has reduced in intensity and a new peak is seen at slightly higher wavelengths around 270 nm. While DR-UV-Vis cannot distinguish Fe oxidation states it can indicate the coordination state of the Fe species in the zeolite. Features below 300 nm are assigned to monomeric Fe species, feature between 300 nm and 400 nm are assigned to oligomeric Fe species such as dimers and features above 400 nm are assigned to Fe_yO_x species.[3, 6, 29-31] Considering this, it is likely both samples contain mainly isolated Fe species while the calcined sample may have more oligomeric species however neither sample has features relating to Fe_yO_x species.

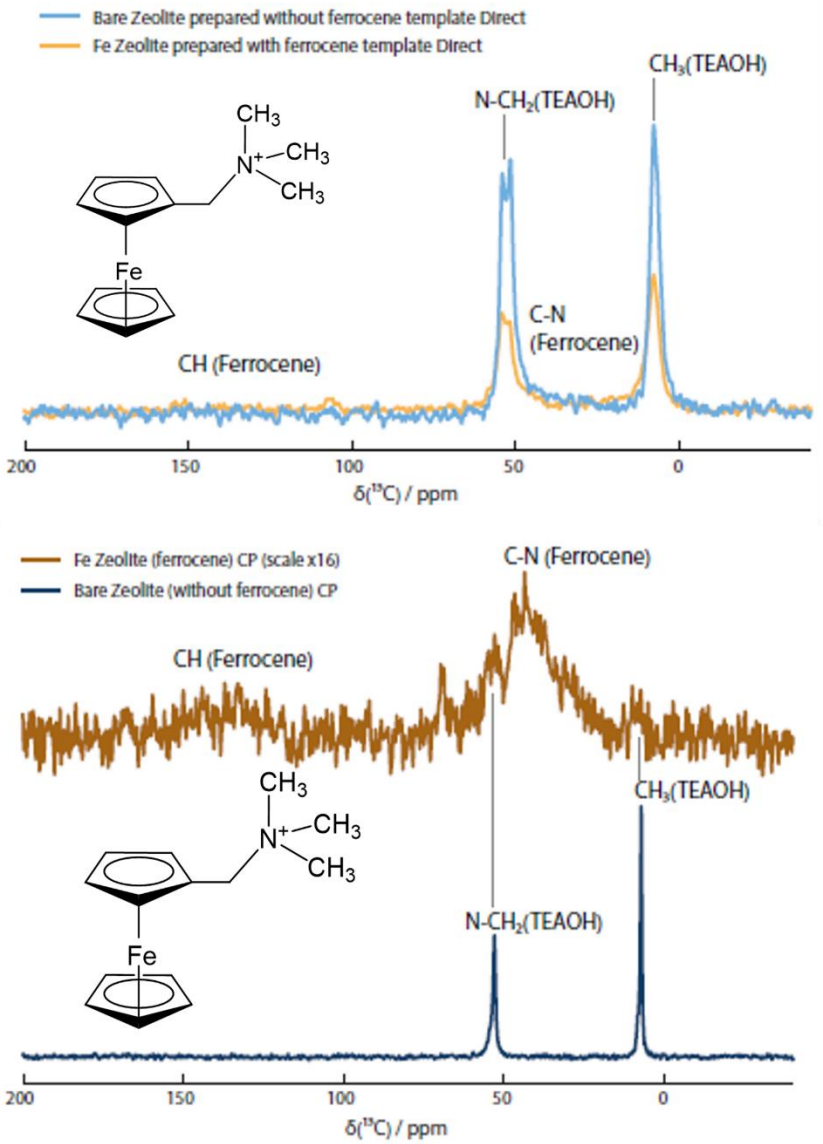

Figure 2-22 *top* Direct excitation *bottom* cross polarised, normalised ^{13}C solid-state MAS NMR spectra of ZEO23 B and equivalent material made without FMTMA

Solid-state ^{13}C MAS NMR spectra of the as made ZEO23 B sample and an equivalent material made without FMTMA are shown in Figure *2-22* . Spectra were acquired using two methods, direct excitation with a fast recycle delay to show signals from any ^{13}C coupled to paramagnetic iron, and cross polarisation (CP) which will enhance the signal for ^{13}C close to ^{1}H but will typically not show signal from paramagnetically coupled sites.

In the direct spectrum, despite the use of a short recycle delay expected to favour paramagnetically influenced sites, there is no signal from the ferrocene component in the

ZEO23 B spectrum and the TEAOH peaks are lower in intensity than those in the bare zeolite spectrum.

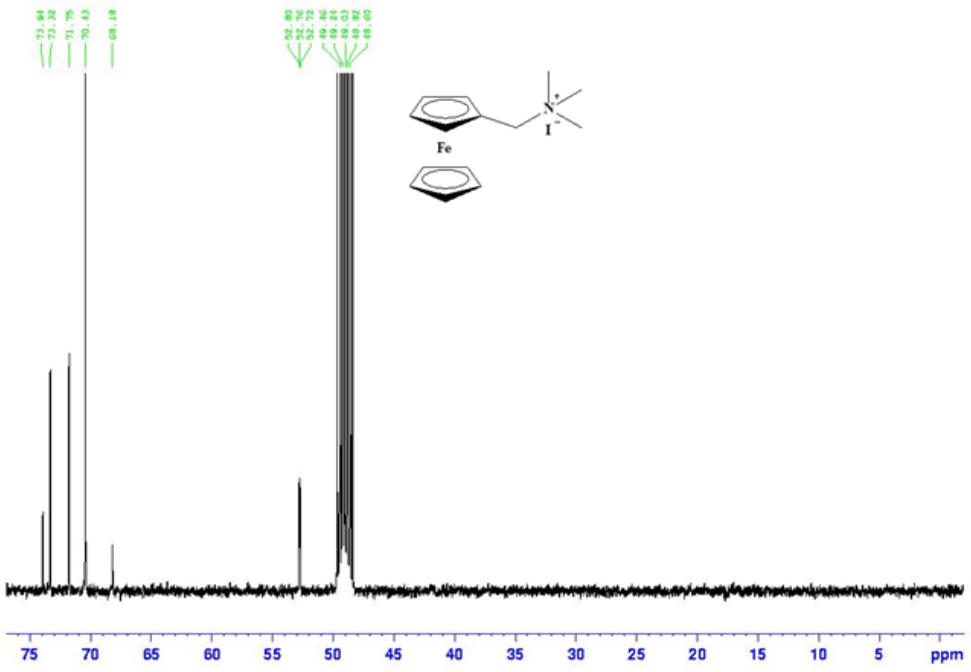

Figure 2-23 ^{13}C NMR spectrum of N,N,N-trimethyl-1-ferrocenylmethanaminium iodide. Reproduced with permission from ref[32]. Copyright 2017 Wiley-VCH

The CP spectra, show clear peaks from the TEAOH template in the non-ferrocene zeolite spectrum. These peaks are not clearly visible above the noise in the ZEO23 B spectrum, which also features very weak and broad signals in approximately the range for the CH and N−CH_3 and N−CH_2 peaks in the ferrocene component. A solution phase ^{13}C NMR spectrum of N,N,N-trimethyl-1-ferrocenylmethanaminium iodide is shown in Figure 2-23 as a comparison.

Although there is some weak evidence of the FMTMA molecule in the CP spectra it is more likely it does not remain intact during the synthesis.

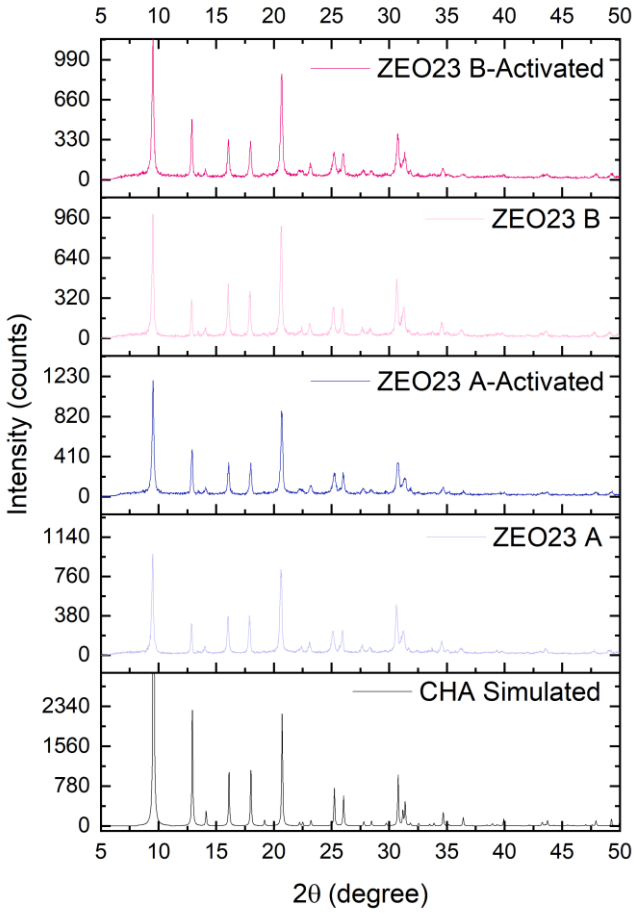

Figure 2-24. pXRD patterns of as made and activated ZEO23 A and B

Table 2-11. Composition of samples ZEO23-A before and after activation determined by XRF

		Na	Al	Si	Cl	K	Fe
ZEO23-A as made	wt %	1.48	4.96	26.92	<0.01	4.43	3.53
ZEO23-A Activated	wt %	0.04	6.30	28.84	<0.01	0.16	3.54

Samples ZEO23-A and B were activated; calcined in air to remove organic, ion-exchanged with ammonium chloride and calcined again in air to produce the proton form of the zeolite.

Iron content remains constant after activation as shown by the composition determined by XRF for ZEO23-A as made and ZEO23-A Activated (Table 2-11) pXRD patterns of the active samples (Figure 2-24) show the structure is retained after the process, meaning the zeolite is stable and suitable for catalytic testing.

2.5 Conclusions

Synthesis conditions to produce SSZ-13 using the FMTMA molecule as a template were developed. It was found that using only FMTMA in the synthesis did not produce a phase pure material. Using FMTMA I^- produced a material with more chabazite compared to FMTMA OH^- which produced a mostly mordenite phase, however the material was not phase pure. Iodide salts are typically not favoured in zeolite as iodide can affect the rate of zeolite crystallisation and they are poorly soluble in aqueous conditions, therefore limiting the amount of template that can be used in the synthesis.

FMTMA OH^- was found to be unstable, experiments have shown it is photosensitive and fresh template should be prepared by ion exchange and then concentrated in the absence of light prior to each synthesis.

Potassium based synthesis methods were also attempted. While one single experiment did produce a phase pure material this could not be repeated, most synthesis batches resulted in the formation of a potassium silicate phase likely due to the high potassium content of the gel.

A dual template approach was attempted using TMAdmA OH^- and FMTMA OH^-. Phase pure chabazite samples were produced only with high ratios of TMAdmA OH^- : FMTMA OH^-. At higher ratios of FMTMA OH^- mordenite and gismondine forms, this indicates TMAdmA OH^- is dominating in the synthesis.

TEA OH^- was also used in a dual template approach with FMTMA OH^-. Using TEA OH^- as a co-template with K^+ produced a sample that was predominantly a chabazite phase with a small mordenite impurity. In contrast to the synthesis with TMAdmA OH^- potassium was required to produce a chabazite with high crystallinity. A 50:50 molar ratio of FMTMA OH^- and TEA OH^- was found to be the limit as increasing FMTMA OH^- beyond this ratio produced mordenite. Unfortunately, further optimisation of the conditions could not produce a phase pure material.

SEM analysis of the material revealed a mixture of small not well defined chabazite crystals and very large rectangular mordenite crystals. TGA analysis indicated a template content of ~7 wt% and this is inline with XRF data which also showed the material has a SAR of ~11.5 and an Fe loading of ~3.7 wt%. The low template content could indicate that the $FMTMA^+$ ion is degrading during the synthesis and K^+ could be contributing to the templating to form chabazite.

DR-UV-Vis data showed mainly isolated Fe species in the as made sample, while in the calcined there was still a majority of isolated species however there was an increase in oligomeric Fe species, importantly no Fe_yO_x species were seen in either sample. The material will be characterised further to determine Fe oxidation states and catalytic activity for the NH_3-SCR reaction, this will be reported in chapter 3.

2.6 References

1. Q. Ye, L. Wang and R. T. Yang, *Applied Catalysis A: General*, 2012, **427-428**, 24-34.
2. X. Yang, Z. Wu, M. Moses-Debusk, D. R. Mullins, S. M. Mahurin, R. A. Geiger, M. Kidder and C. K. Narula, *The Journal of Physical Chemistry C*, 2012, **116**, 23322-23331.
3. F. Gao, Y. Zheng, R. K. Kukkadapu, Y. Wang, E. D. Walter, B. Schwenzer, J. Szanyi and C. H. F. Peden, *ACS Catalysis*, 2016, **6**, 2939-2954.
4. J. Szanyi, F. Gao, J. H. Kwak, M. Kollar, Y. Wang and C. H. Peden, *Phys. Chem. Chem. Phys.*, 2016, **18**, 10473-10485.
5. F. Gao, M. Kollár, R. K. Kukkadapu, N. M. Washton, Y. Wang, J. Szanyi and C. H. F. Peden, *Applied Catalysis B: Environmental*, 2015, **164**, 407-419.
6. F. Gao, J. Szanyi, Y. Wang, B. Schwenzer, M. Kollár and C. H. F. Peden, *Top. Catal.*, 2016, **59**, 882-886.
7. L. Kovarik, N. M. Washton, R. Kukkadapu, A. Devaraj, A. Wang, Y. Wang, J. Szanyi, C. H. F. Peden and F. Gao, *ACS Catalysis*, 2017, **7**, 2458-2470.
8. F. Gao, Y. Wang, M. Kollár, N. M. Washton, J. Szanyi and C. H. F. Peden, *Catal. Today*, 2015, **258**, 347-358.
9. W. K. Hall, X. Feng, J. Dumesic and R. Watwe, *Catal. Lett.*, 1998, **52**, 13-19.
10. J. Pieterse, *Applied Catalysis B: Environmental*, 2004, **51**, 215-228.
11. M. Dusselier and M. E. Davis, *Chem Rev*, 2018, **118**, 5265-5329.
12. C. Yin, P. Cheng, X. Li and R. T. Yang, *Catalysis Science & Technology*, 2016, **6**, 7561-7568.
13. K. Niu, G. Li, J. Liu and Y. Wei, *Journal of Solid State Chemistry*, 2020, **287**.
14. P. R. Varadwaj, A. Varadwaj and B. Y. Jin, *Phys. Chem. Chem. Phys.*, 2015, **17**, 805-811.
15. H. Irving and R. J. P. Williams, *J. Chem. Soc.*, 1953, 3192-3210.
16. E. Yuan, G. Wu, W. Dai, N. Guan and L. Li, *Catalysis Science & Technology*, 2017, **7**, 3036-3044.
17. A. Turrina, A. Iulian Dugulan, J. E. Collier, R. I. Walton, J. L. Casci and P. A. Wright, *Catalysis Science & Technology*, 2017, **7**, 4366-4374.

18. A. A. Coelho, *Journal of Applied Crystallography*, 2018, **51**, 210-218.
19. R. Kumar, A. Bhaumik, R. K. Ahedi and S. Ganapathy, *Nature*, 1996, **381**, 298-300.
20. C. W. Purnomo, C. Salim and H. Hinode, *Microporous and Mesoporous Materials*, 2012, **162**, 6-13.
21. A. V. Toktarev and G. V. Echevskii, in *Stud. Surf. Sci. Catal.*, eds. A. Gédéon, P. Massiani and F. Babonneau, Elsevier, 2008, vol. 174, ch. 3, pp. 167-172.
22. A. M. Tarr and D. M. Wiles, *Can. J. Chem.*, 1968, **46**, 2725-2731.
23. L. Zhang, X. Gao, L. Yang, P. Yu and L. Mao, *ACS Appl Mater Interfaces*, 2013, **5**, 8120-8124.
24. L. H. Ali, A. Cox and T. J. Kemp, *J. Chem. Soc,. Dalton Trans.*, 1973, 1468-1475.
25. L. Van Tendeloo, E. Gobechiya, E. Breynaert, J. A. Martens and C. E. A. Kirschhock, *Chem. Commun.*, 2013, **49**.
26. N. Martin, M. Moliner and A. Corma, *Chem. Commun*, 2015, **51**, 9965-9968.
27. J. E. Schmidt, D. Fu, M. W. Deem and B. M. Weckhuysen, *Angew Chem Int Ed Engl*, 2016, **55**, 16044-16048.
28. S. Goel, S. I. Zones and E. Iglesia, *Chemistry of Materials*, 2015, **27**, 2056-2066.
29. M. Schwidder, M. Santhosh Kumar, U. Bentrup, J. Pérez-Ramírez, A. Brückner and W. Grünert, *Microporous and Mesoporous Materials*, 2008, **111**, 124-133.
30. M. S. Kumar, M. Schwidder, W. Grünert and A. Brückner, *Journal of Catalysis*, 2004, **227**, 384-397.
31. J. Zhang, X. Tang, H. Yi, Q. Yu, Y. Zhang, J. Wei and Y. Yuan, *Applied Catalysis A: General*, 2022, **630**.
32. S. N. P. Ndlovu, H. Ibrahim and M. D. Bala, *J. Heterocycl. Chem.*, 2017, **54**, 3646-3655.

Chapter 3 . Selective catalytic reduction testing of ferrocene chabazite

3.1 Introduction

Fe zeolites have been examined for the SCR reaction for many years, Fe-ZSM5 was first shown to be active for hydrocarbon and NH_3 SCR in the 1990's outperforming existing V_2O_5/WO_3-TiO_2 catalysts.[1, 2] One of the key features of Fe zeolites over Cu counterparts is their higher NO_x conversion at higher temperatures, and it is thought this is due to a slower NH_3 oxidation side reaction occurring on Fe zeolites.[3]

Ye et al.[4] first used Fe-SSZ-13 to compare against Cu counterparts, they found Fe-SSZ-13 exhibited lower NO conversion at low temperatures below 350 °C, while activities increased at higher temperatures between 350 °C and 550 °C. The poor activity at low temperature was attributed to ammonia inhibition,[5-7] this is when NH_3 dominates the competitive adsorption between NOx and NH_3 at low temperatures. Gao et al. showed Fe-SSZ-13 could be used as a highly active SCR catalyst itself.[8-10] Fe-SSZ-13 has been shown to be active at high temperature for both standard SCR ($4NO + 4NH_3 + O_2 \rightarrow 4N_2 + 6H_2O$) and fast SCR ($NO + NO_2 + 2NH_3 \rightarrow 2N_2 + 3H_2O$).[11]

Gao et al. conducted spectroscopic analysis of Fe loaded SSZ-13 to determine the structure function relations of the catalyst for standard SCR.[8] The study identified two key active centres in their catalyst, an isolated $[Fe(OH)_2]^+$ and a dimeric $[HO\text{-}Fe\text{-}O\text{-}Fe\text{-}OH]^{2+}$, both in charge-balancing ion-exchange positions. They claim isolated $[Fe(OH)_2]^+$ sites are the major low-temperature (<300 °C) active centres for standard SCR, whereas $[HO\text{-}Fe\text{-}O\text{-}Fe\text{-}OH]^{2+}$ sites are responsible for high-temperature (≥300 °C) SCR activity and side reactions such as parasitic NH_3 oxidation. The catalyst Gao et al. produced also contained small amounts of isolated Fe^{2+} sites and Fe-oxide clusters and particles. Gao et al. determined isolated Fe^{2+} sites are spectators for SCR as reoxidation of Fe^{2+} to Fe^{3+} is difficult by O_2.[12] Fe-oxide clusters and particles may be considered as high-temperature SCR active phases. However, because these are minority sites, and they catalyse NH_3 oxidation by O_2 at temperatures above 300 °C they are not key contributors in Fe-SSZ-13 SCR catalysts.

While Gao et al. state they identified the two key active centres in the Fe-SSZ-13, they could not produce a catalyst with only these active sites, and therefore synergistic effects of different Fe sites cannot be discounted. In the previous chapter it was shown an Fe-SSZ-13 can be made with predominantly isolated homogenous species by using FMTMA as a

templating agent in the synthesis. In this study, Fe-SSZ-13 made using the FMTMA template (Fc-SSZ-13) is tested under standard NH_3-SCR reaction conditions and compared against an equivalent Fe-SSZ-13 made using a standard incipient wetness impregnation method. The catalyst is compared both fresh and hydrothermally aged and spent catalysts are spectroscopically analysed to determine deactivation mechanisms.

3.2 Experimental methods

3.2.1 Materials

3.2.1.1 Activated Fc-SSZ-13

A larger batch of the Fc-SSZ-13 was produced by scaling out the procedure for ZEO23 -A outlined in Chapter 2, all samples were analysed separately prior to combining into a large batch. This larger batch of the as made material was divided into two and activated by two different methods, either in air or in N_2 outlined in the procedures below.

As made zeolites were calcined in either a flow of air or nitrogen under the following procedure: zeolites were ground with a mortar and pestle prior to calcination. Samples were heated in a calcination oven, air flow was set to 200 ml/min the oven was programmed to increase the temperature from room temperature to 110 ^oC at 2 ^oC/min to removed adsorbed water. Then the temperature was then increased further to 450 ^oC at 5 ^oC/min and held at 450 ^oC for 16 h. Next, the temperature was further increased again to 550 ^oC at 5 ^oC/min and held at 550 ^oC for 16 h. Finally, the heating was stopped, and the sample was left to cool down. For nitrogen calcination the same temperature program was used as for the air, N_2 flow was set to 200 ml/min and the oven was purged with N_2 for 30 mins prior to starting the heating procedure.

The calcined zeolites were ion exchanged with ammonium chloride. An aqueous ammonium chloride solution (1 M) was mixed with dry zeolite for 1 hour (10 mL of solution per 1 g of calcined zeolite). The solid was collected by filtration and the ion exchange process was repeated a second time. After the second ion exchange the solid was filtered until the supernatant liquid reached a conductivity of below 50 µS to ensure exchanged cations have been washed away. The solid was then dried overnight at 110 °C.

The dried ion exchanged zeolite was activated to produce the proton form of the zeolite. Zeolites were activated in either a flow air or nitrogen under the following procedure:

Zeolites were ground to a fine powder with a mortar and pestle prior to activation. Samples were heated in a calcination oven, air flow was set to 200 ml/min the oven was programmed to increase the temperature from room temperature to 150 °C at 2 °C/min and held at 150 °C for 10 h. The temperature was then increased further to 450 °C at 5 °C/min and held at 450 °C for 16 h. Finally, heating was stopped, and the sample was left to cool down. For nitrogen calcination the same temperature program was used as for the air, N_2 flow was set to 200 ml/min and the oven was purged with N_2 for 30 mins prior to starting the heating procedure.

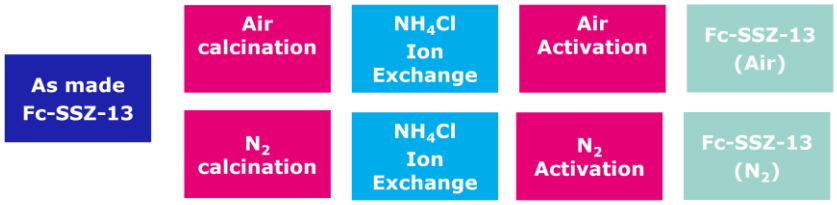

Figure 3-1. Schematic of the calcination, ion exchange and activation procedure

3.2.1.2 Benchmark Fe-SSZ-13

Benchmark material was prepared by the incipient wetness impregnation of an SSZ-13 with solutions of $FeCl_2$. The SSZ-13 used was an equivalent to the Fc-SSZ-13 produced without the ferrocene template, synthesis details are outlined below.

The SSZ-13 was prepared by hydrothermal synthesis, a zeolite gel was first prepared by dissolving 1.86 g of KOH (85 %) (Fischer Scientific) in 25.51 g of deionised water, 5.15g of TEAOH (purchased from large scale OSDA provider) was added slowly to the basic solution. Then 3.52 g of CBV500 (Zeolyst) was added to the basic solution and stirred until homogenous. Finally, 57.35 g of sodium silicate (Grace Crysal 0079) was added slowly to the mixture and stirred until homogenous. The total gel was 62.5 mL and total mass was 87.63 g was transferred to a 150 mL Teflon liner and placed into a stainless-steel autoclave. The autoclave was rotated at 30 rpm, for 48 hours at 150 °C. The solid product was washed by centrifugation at 3800 rpm in 5 min cycles until the supernatant liquid reached a conductivity of below 500 µS, to ensure excess cations are washed from the zeolite. The solid was then dried overnight at 110 °C.

The moisture content of the zeolite was first calculated using a moisture balance. Then pore volume of the parent zeolite was calculated by gradually wetting 1 g of zeolite with water until a sand like consistency is achieved. The Fe was loaded by dissolving 1.41 g of $FeCl_2.4H_2O$

(Merck) in 5.2 mL of deionised water. The Fe solution was then added dropwise to the zeolite and thoroughly mixed until a sand like consistency is achieved. The sample was then dried at 105 °C for 30 mins and homogenised with a mortar and pestle. Finally, the sample was calcined to 500 °C at a rate of 10 °C/min for 2 hours under a N_2 atmosphere.

Table 3-1. Samples prepared for testing

Sample	Activation Treatment	SAR	Fe concentration [wt %]
Fc-SSZ-13 (As made)	n/a	10.72	3.53
Fc-SSZ-13 (Air)	Air	10.82	3.54
Fc-SSZ-13 (N_2)	N_2	10.93	3.55
H-SSZ-13	Air	11.51	n/a
Fe-SSZ-13	N_2	11.56	3.18

3.2.2 NH_3-SCR activity testing

Catalytic testing was performed on calcined samples. Samples were pelletised using an 8 mm die under 0.4 ton of force then crushed and sieved to give a fraction between 255 and 350 microns. The powder samples were loaded into a proprietary reactor designed inhouse at Johnson Matthey Sonning and tested using the following synthetic diesel exhaust gas mixture (at inlet) including ammonia: 350 ppm NO, 385 ppm NH_3, 12% O_2, 4.5% H_2O, 4.5% CO_2, 200 ppm CO, balance N_2, at a space velocity of 330 L per gram of powder per hour. The samples were heated from 150 to 550 °C at 5 °C min^{-1} and the effluent gases were analysed by an FTIR analyser, the FTIR analyser was calibrated externally. To determine the hydrothermal stability of the catalyst a set of pelletised samples were aged by heating them to 650 °C (heating rate of 10 °C min^{-1}) for 1 h in a flow reactor with a gas containing 4.5% H_2O in air at a flow rate of 1.3 L $min^{-1,}$ these samples were later tested under the same conditions as the fresh sample.

3.2.3 Ar adsorption

Samples were subjected to analysis by Ar physisorption measurements. Absorption and desorption isotherms were collected on a Micromeritics 3500 3Flex instrument. Experiments

were conducted at 87 K for Ar isotherms. Prior to measurement, the samples were heated under vacuum at 623 K for 16 h to remove physisorbed water. Isotherms were subject to BET analysis for surface area calculation.

3.2.4 X-Ray Absorption spectroscopy near edge structure (XANES)

Experiments were conducted on the EasyXAFS300+ laboratory-scale spectrometer (easyXAFS, WA), which uses a Rowland circle optical geometry.[13, 14] Samples were prepared by mixing a known mass of sample (shown in Table 3-2) with cellulose (Avicel® PH-101) and the diluted sample was pressed into 13 mm diameter pellet under 0.8 ton of force using a die cast and a hydrolytic press (both supplied by Specac) Fe K-edge XAFS were acquired using a Ge (620) spherically bent crystal analyser (SBCA) and an Ag anode X-ray tube at 40 kV. The X-ray current was varied between 6 to 15 mA (240 – 600 W), depending on the sample to maintain a collection deadtime of < 30 %. 5 consecutive scans were performed for all samples, collecting the intensity of the transmitted beam (It) for each sample, and incident beam only (I_0), with the total times shown in Table 3-1. Scan parameters used are shown below in Table 3-2.

Table 3-2. Sample details for XANES spectra

Sample	Edge and experiment	Amount used /mg	Time per sample*
Fe-SSZ-13 aged 650 °C	Fe K-edge XANES	70 mg	1h 23m
Fc-SSZ-13 (Air)	Fe K-edge XANES	65 mg	1h 23m
Fc-SSZ-13 (Air) Spent 550 °C	Fe K-edge XANES	65 mg	1h 23m
Fc-SSZ-13 (Air) Aged 650 °C	Fe K-edge XANES	65 mg	1h 23m
Fc-SSZ-13 (N_2)	Fe K-edge XANES	68 mg	1h 23m
Fc-SSZ-13 (N_2) Spent 550 °C	Fe K-edge XANES	68 mg	1h 23m
Fc-SSZ-13 (N_2) Aged 650 °C	Fe K-edge XANES	68 mg	1h 23m
Fc-SSZ-13 (As made)	Fe K-edge XANES	68 mg	1h 23m
FMTMA I^-	Fe K-edge XANES	18 mg	1h 23m
Fe_Foil	Fe K-edge XANES	n/a	1h 23m

*Time does not include the collection of the incident beam (I_0) scan. I_0 scan was conducted, taking 1 hours and 23 min for the Fe K-edge, using the same X-ray source at 40 kV and 6 mA.

Table 3-3. Scanning parameters used for Fe K-edge XAFS experiment

Energy range /eV	Step size / eV step^{-1}	Duration per step /s
7072 – 7097	2	1.5
7097 – 7152	0.25	3
7152 – 7292	2	3

3.2.5 Mößbauer

Transmission 57Fe Mössbauer spectra were collected at 300 K with conventional constant-acceleration or sinusoidal velocity spectrometers using a 57Co(Rh) source. Velocity calibration was carried out using an α-Fe foil. The source and the absorbing samples were kept at the same temperature during the measurements. The Mössbauer spectra were fitted using the Mosswinn 4.0 program.[15]

3.2.6 X-Ray photoelectron spectroscopy

The study was carried out with a Thermo Escalab 250. Samples were used as received. For analysis samples were dusted onto carbon tape and thereby attached to a sample plate. The radiation used was monochromatised aluminium Kα radiation with a 650 µm spot size. Charge compensation was provided by the in-lens electron flood gun at a 2 eV setting and the "401" unit for "zero energy" argon ions.

3.3 Results and discussion

3.3.1 Catalytic activity

3.3.1.1 Fresh activity

The catalytic activity of the fresh Fe zeolites for NH_3-SCR are shown in Figure 3-2. The NO conversion of fresh Fc-SSZ-13 and Fe-SSZ-13 are shown in Figure 3-2, H-SSZ-13 is also included as a control for these tests. Fe-SSZ-13 performs the best of all the zeolites tested reaching complete conversion at around 315 °C, this conversion stays stable until around 470 °C where it starts to decrease. The two Fc-SSZ-13 samples performed poorer. The N_2 activated sample showed a similar activity to the Fe-SSZ-13 sample, although complete conversion was achieved at around 325 °C, 10 °C higher than the Fe-SSZ-13 sample.

Conversion started to decrease around 420 °C, ~50 °C lower than for the Fe-SSZ-13 sample. These differences may be due to presence of different Fe species and the stability of those species at higher temperatures. The air activated sample achieves maximum conversion of 95 % at ~355 °C, conversion drops quickly after reaching its maximum before gradually starting to rise again above 450 °C. The shape of this conversion curve is different to the other two iron SSZ-13 samples, the drop in NO conversion between 355 and 450 °C may be due to structural changes in the zeolite or Fe speciation changes during the reaction.

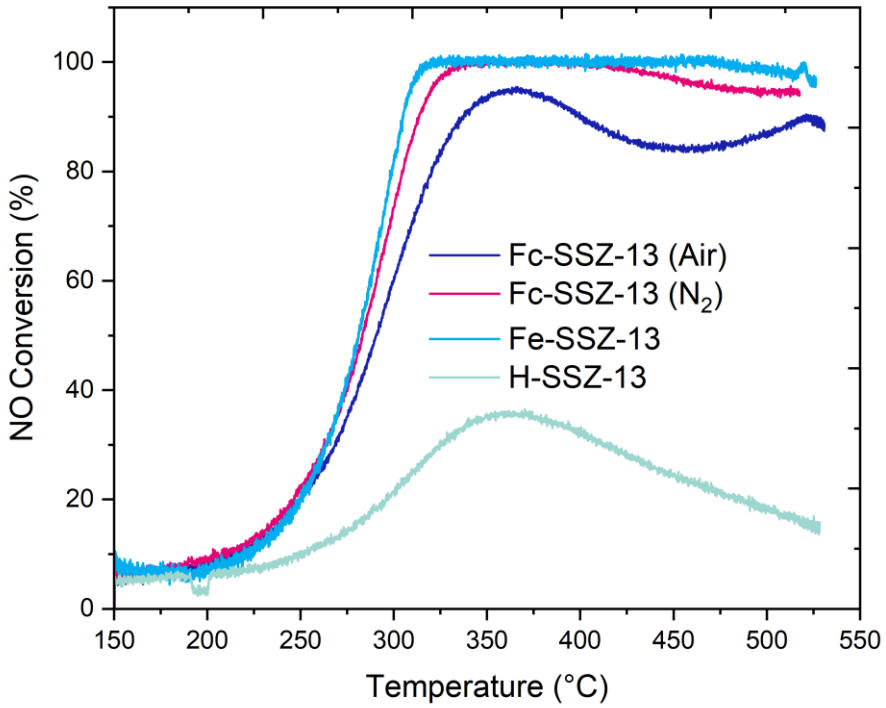

Figure 3-2. Conversion of NO in the NH_3-SCR reaction for fresh materials

3.3.1.2 Aged catalytic activity

The catalytic activity of hydrothermally aged zeolites for NH_3-SCR are show in Figure 3-3. Although there is a clear difference between fresh and aged, with the aged samples performing poorer across the board vs the fresh samples, as seen in the fresh activity test Fe-SSZ-13 performs the best of all the samples. Complete conversion is achieved at around 410 °C and starts to decrease at higher temperatures, this is almost 100 °C higher than for the fresh sample. The aged sample does show higher NO conversion at lower temperatures compared to the fresh sample; this may be due to speciation change during the ageing

process. Again, both Fc-SSZ-13 samples performed poorer than the Fe-SSZ-13 sample. The N_2 activated sample performed better than the air activated sample, however neither sample was able to achieve complete conversion. These aged catalytic activity tests indicate there are either structural or speciation changes occurring in during the aging process.

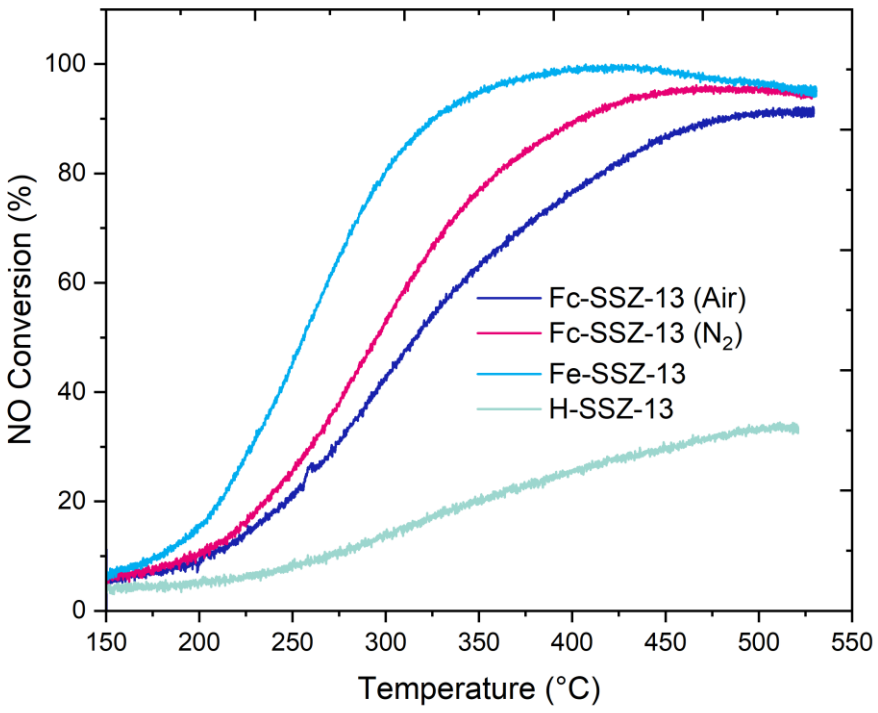

Figure 3-3. Conversion of NO in the NH_3-SCR reaction for hydrothermally aged materials (650 °C, 50 h)

3.3.2 Structural and imaging characterisation

3.3.2.1 Argon adsorption results

Argon adsorption results of the fresh samples are shown in Figure 3-4. The samples exhibited a type I isotherm when adsorbing Ar at 87 K. Surface area and pore volumes results (Table 3-4) show, while the surface area of all fresh samples are similar, the micropore volume of the Fc-SSZ-13 samples is lower than the Fe-SSZ-13 sample. This difference may be a feature of the ferrocene samples, as the FMTMA template may have affected the textural properties

of the samples. The mesopore volume is significantly higher for the Fc-SSZ-13 samples than for the Fe-SSZ-13 sample. This difference is not thought to be intra-crystal porosity but inter-crystal porosity, this higher value could be inflated by the large slab crystal present in the Fc-SSZ-13 samples, although the SEM may not be representative of the whole sample.

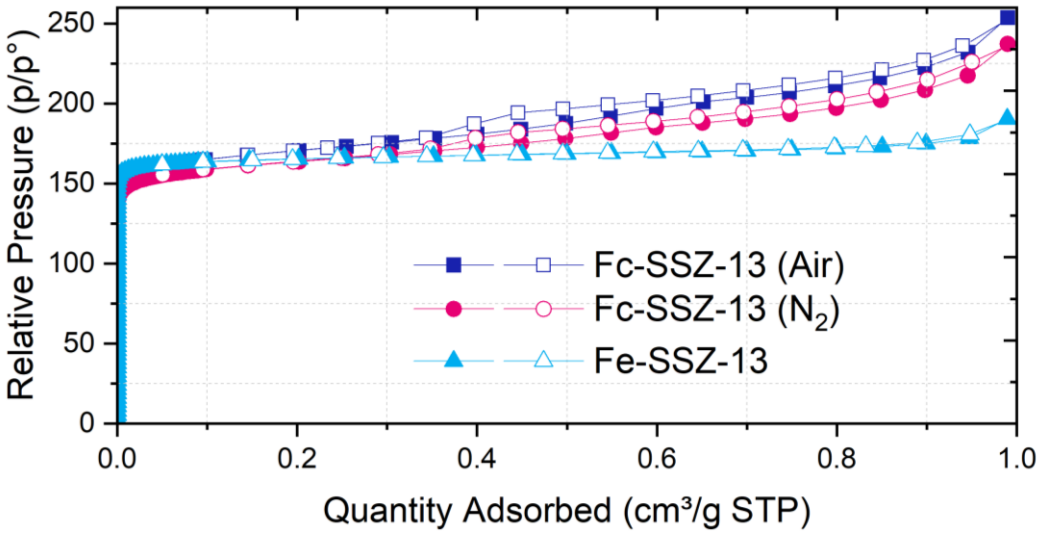

Figure 3-4 Ar adsorption (filled symbols) and desorption (hollow symbols) isotherms at 87 K

Table 3-4. BET surface area, micro and meso pore volume of Fc-SSZ-13 (Air) and (N_2) and Fe-SSZ-13

Ar Adsorption	Apparent BET area (m^2g^{-1})	Micro Pore Vol (cm^3g^{-1})	Meso Pore Vol (cm^3g^{-1})
Fc-SSZ-13 (Air)	593	0.174	0.150
Fc-SSZ-13 (N_2)	573	0.170	0.133
Fe-SSZ-13	603	0.207	0.036

3.3.2.2 SEM results

SEM and elemental distribution images are shown in Figure 3-5. The images show Fe is homogenously distributed throughout the zeolite samples and the Fe distribution is not affect by the calcination and activation procedure. The SEM image also appears to show Fe is absent from the large slab crystals in the catalyst sample. This is more clearly shown in Figure 3-6 which maps all the elements present in the sample. SEM images and elemental distribution of the Fe-SSZ-13 are shown in Figure 3-7. These images clearly show the Fe is not

homogenously distributed as in Fc-SSZ-13 samples and there are large areas with high concentrations of Fe.

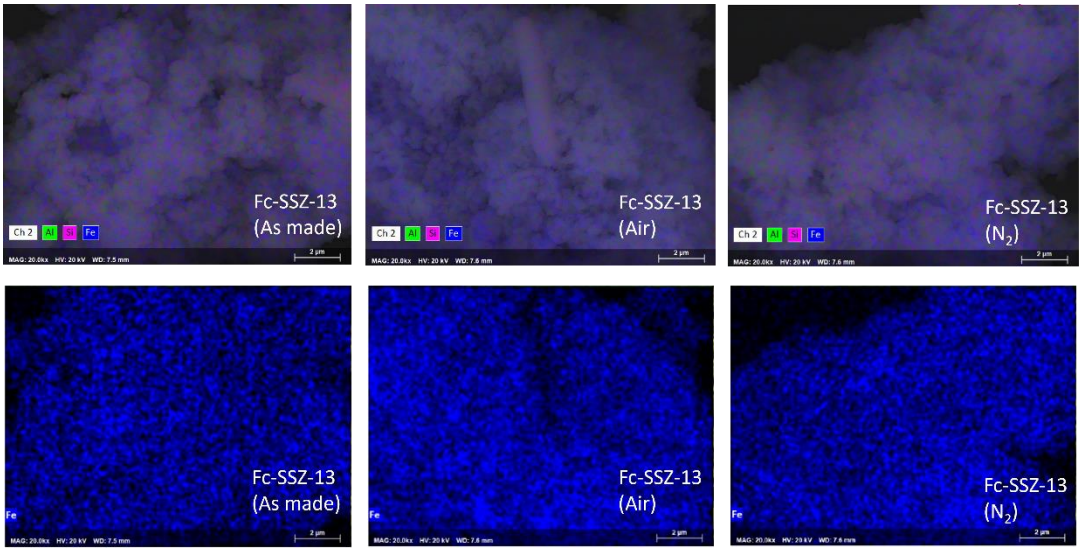

Figure 3-5. SEM and elemental distribution of Fc-SSZ-13 (as made), (air) and (N_2) samples

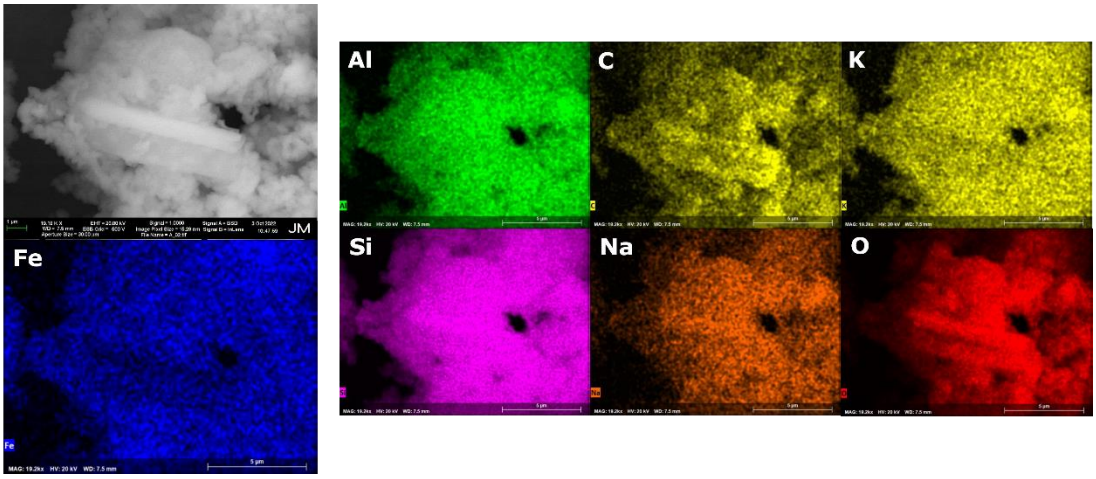

Figure 3-6 SEM and elemental distribution of a selected Fc-SSZ-13 sample highlighting the absence of Fe in the large slab crystals within the sample

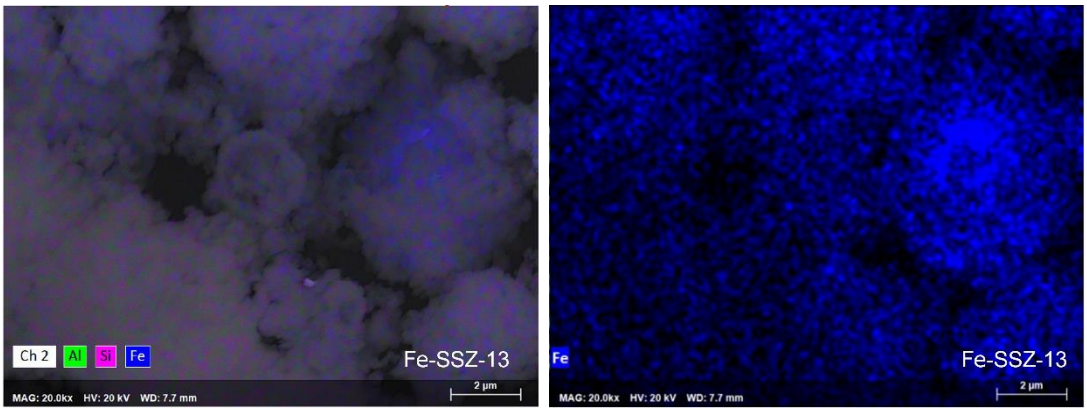

Figure 3-7 SEM and elemental distribution of Fe-SSZ-13

3.3.2.3 X-ray diffraction of spent and aged samples

pXRD patterns of fresh, spent and aged Fc-SSZ-13 samples are shown in Figure 3-8 and Figure 3-9. Spent samples are samples that have been tested under reaction conditions then re-tested under the same conditions. These patterns clearly show the increase in intensity of peaks at 6.5 °, 8.7 ° and 15.3 ° in both samples as the zeolite is subjected to harsher conditions. These peaks are constant with mordenite and the increase in intensity of these peaks relative to the CHA peaks is likely caused by the degradation of the chabazite structure in the Fc-SSZ-13 samples.

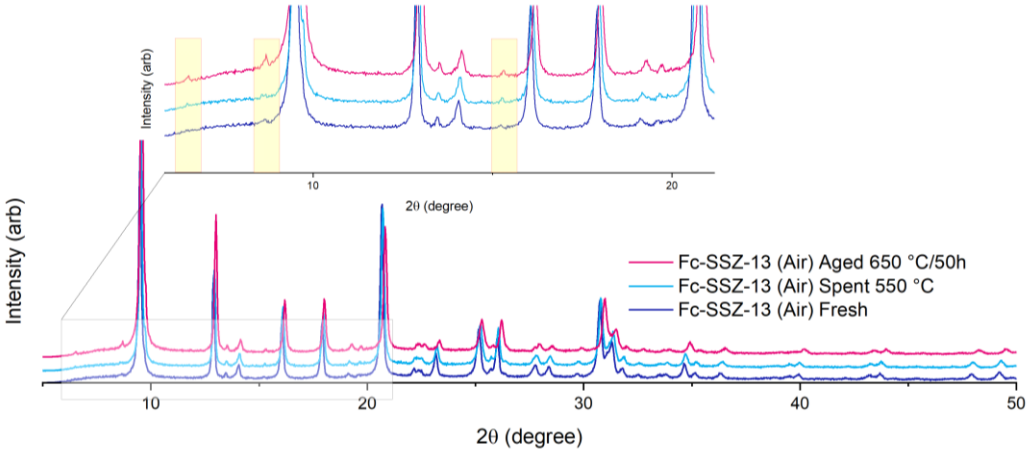

Figure 3-8. pXRD patterns of fresh, spent, and aged Fc-SSZ-13 (Air) samples. Changes in the pattern are highlighted in yellow within the magnified inset

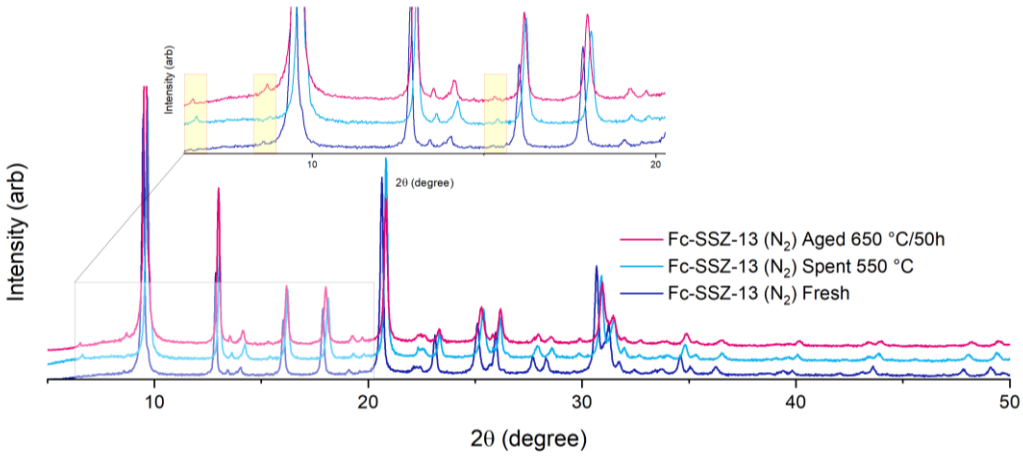

Figure 3-9. pXRD patterns of fresh, spent, and aged Fc-SSZ-13 (N_2) samples. Changes in the pattern are highlighted in yellow within the magnified inset

pXRD patterns of the fresh, spent, and aged Fe-SSZ-13 sample is shown in Figure 3-10. Like the Fc-SSZ-13 samples there is a slight increase in the intensity of the peaks relating to mordenite as the zeolite is subjected to harsher conditions however, the change is much less evident. These differences between Fc-SSZ-13 and Fe-SSZ-13 are likely due to the synthesis, it is likely the FMTMA template is causing the Fc-SSZ-13 to be less stable under harsher conditions. This could be due to the formation of siloxy defects as a results of the OSDA[16], characterisation techniques such as ^{1}H NMR, ^{29}Si NMR or FTIR could be used to determine these defects. This was not done for these samples and should be done in any further work. A slight peak shift can be seen between the fresh and aged samples, attributing this to any structural changes is difficult as instrumental effects and absorption effects can cause peaks to shift.

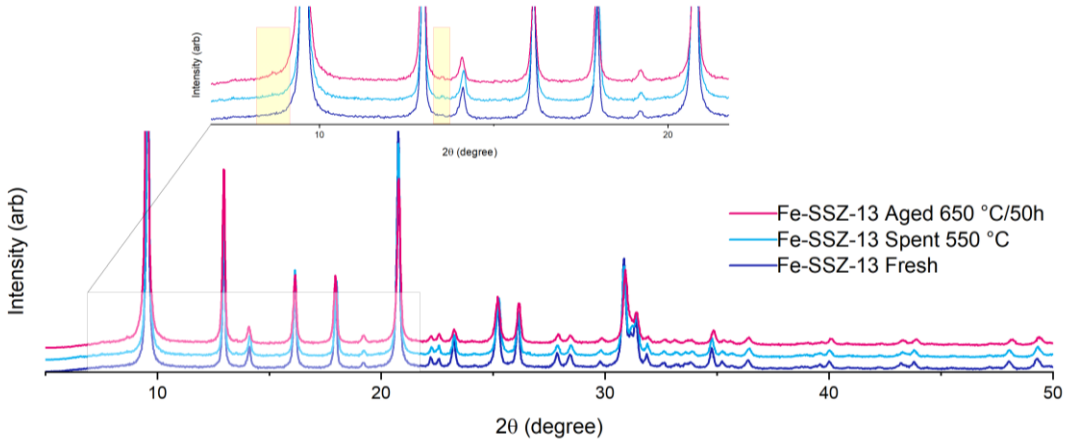

Figure 3-10. pXRD patterns of fresh, spent, and aged Fe-SSZ-13 samples. Changes in the pattern are highlighted in yellow within the magnified inset

3.3.3 Spectroscopic characterisation

3.3.3.1 X-Ray photoelectron spectroscopy results

Distinguishing between Fe^{2+} and Fe^{3+} is mostly based on the presence of satellite features in X-Ray photoelectron spectra, which especially in the case of Fe^{3+}can be weak and unclear. Fe3p signals can also be used to determine oxidation state[17], with Fe^{2+} appearing at ~53.5 eV and Fe^{3+} at ~55.5 eV. The Fe 3p spectra (Figure 3-11) for these samples has a main peak at ~56.5 eV and a shoulder at ~54.5 eV. It is therefore assumed that these are for Fe^{2+} and Fe^{3+} however these are shifted ~1 eV higher than reported in the literature. The noise in these samples makes it difficult to extract quantitative information however some differences can be seen in the spectra. The Fe-SSZ-13 sample is very noisy but does show a broad peak around 56.5 ev likely corresponding to a mixture of Fe^{2+} and Fe^{3+}. The Ferrocene sample are less noisy both the calcined samples are very similar with a main peak around 56.5 ev indication mostly Fe^{3+}, the as made sample shows an additional feature around 55.5 ev indicting the presence of Fe^{2+} in this sample.

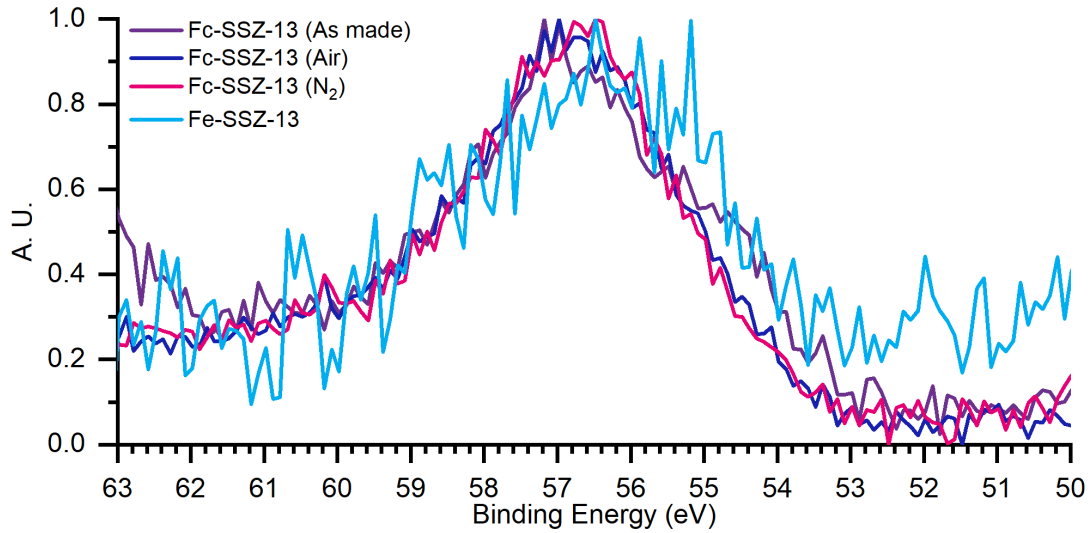

Figure 3-11 Iron 3p signals from the samples. Energy as recorded. Intensities normalised

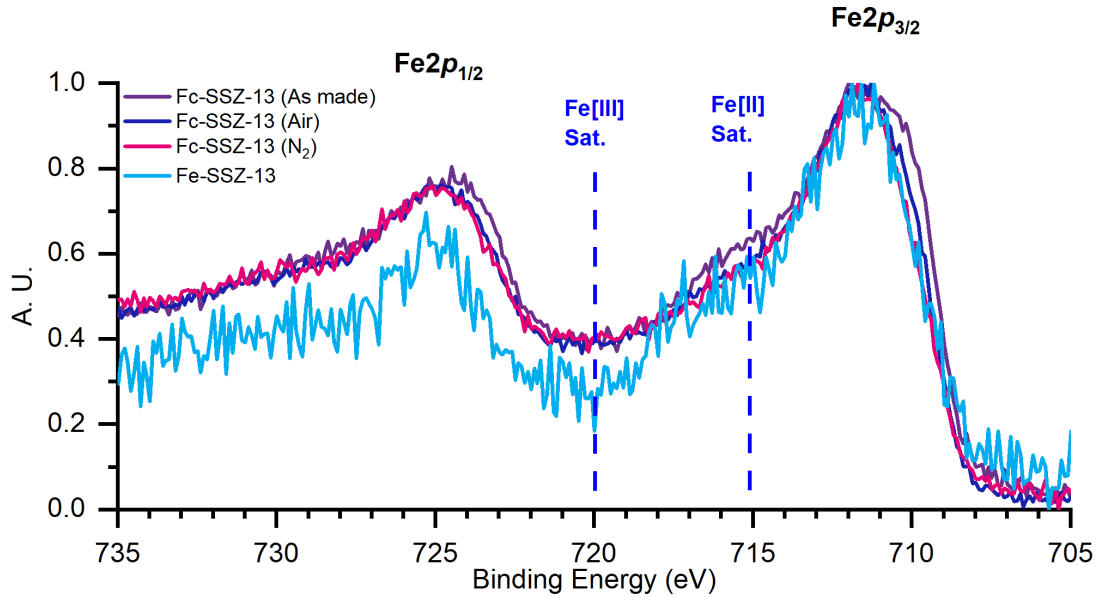

Figure 3-12 Iron 2p signals from the samples. Energy as recorded. Intensities normalised

As the Fe2p and Fe3p core lines are separated by ~700 eV, comparing both can give an indication of where the iron is located in terms of depth. The higher the binding energy (Fe2p), the lower the kinetic energy of the escaping photoelectron and therefore it has a lower inelastic mean free path and consequently has a shallower escape depth. The

comparison of the Fe2p and Fe3p atomic percentages calculated by relative intensities of the peak areas are shown in Table 3-5. These results indicate the Fe is located more towards the surface of the Ferrocene samples and the Fe is deeper in the material for the Fe-SSZ-13 material.

Table 3-5. Atomic percentages relating to the Fe2p and Fe3p core lines

At%	Fc-SSZ-13 (As made)	Fc-SSZ-13 (Air)	Fc-SSZ-13 (N_2)	Fe-SSZ-13
Fe2p	2.5	2.9	2.2	0.7
Fe3p	1.0	1.4	1.1	0.3

3.3.3.2 DR UV-Vis results

DR UV-Vis measurements of as made, air activated, N_2 activated Fc-SSZ-13 and Fe-SSZ-13 are shown in Figure 3-13. DR UV-Vis is not quantitative however it can indicate the different Fe species present in the sample. To illustrate the contribution of the different Fe species present in the sample the spectra have been fitted with Gaussian functions in OriginPro 2020. Blue peaks between 200-300 nm represent isolated species. Dark blue peaks below 250 nm can be attributed to isolated iron in a tetrahedral coordination geometry. Light blue peaks between 250-300 nm relate to isolated iron in octahedral coordination geometry. Pink peaks above 300 nm represent multi nuclear Fe species such as dimeric, oligomeric species and bulk iron oxide particles,[18-22] the darker the shade of pink the higher the nuclearity.

These results show that all samples contain primarily isolated Fe species. Dimeric and oligomeric contributions can also be seen in all samples, the contribution of these species is most evident in the Fe-SSZ-13 sample. This sample also has the largest contribution attributed to iron oxide particles.

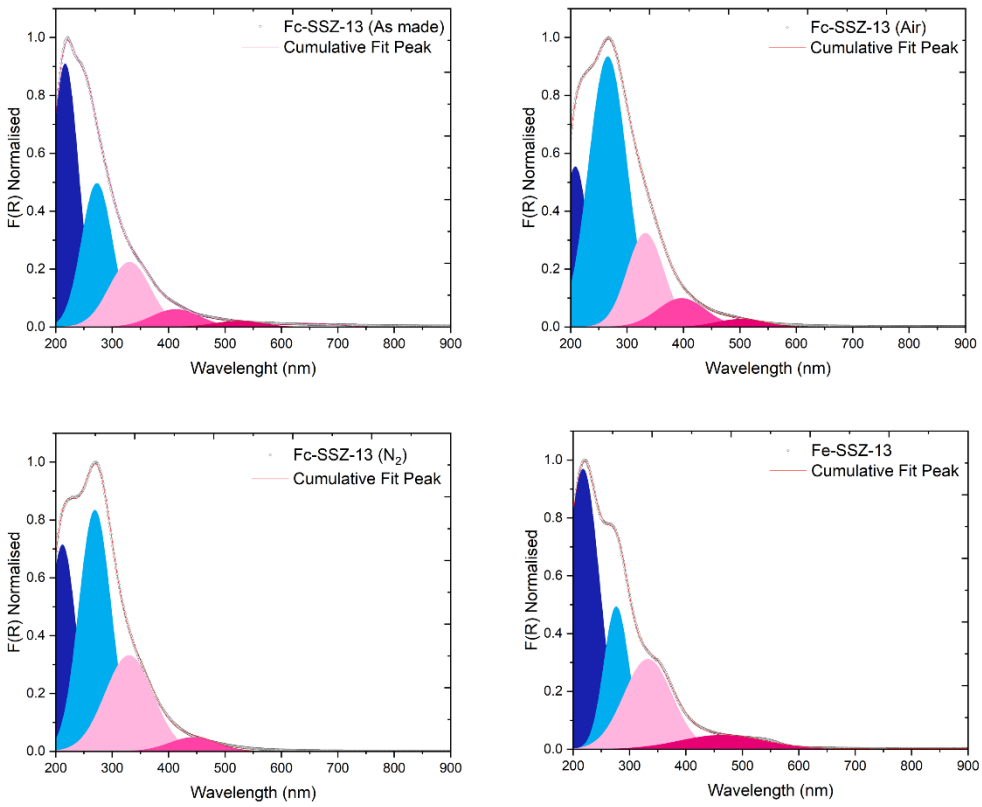

Figure 3-13. DR UV-Vis of Fc-SSZ-13 (As made), Fc-SSZ-13 (Air), Fc-SSZ-13 (N_2) and Fe-SSZ-13. Isolated Fe species are shown in blue, Fe_xO_y oligomers are shown in light pink and Fe_2O_3 clusters are shown in dark pink

A comparison between fresh and aged Fc-SSZ-13 samples is shown in Figure 3-14. These results show that in both the air and N_2 samples the peak around 260 nm decreases in intensity. It appears there is some sintering occurring during the ageing process. As, the contribution of species relating to octahedrally coordinated Fe seem to decrease while contribution the species relating to dimeric, oligomeric and Fe_xO_y species increases in the spectrum.

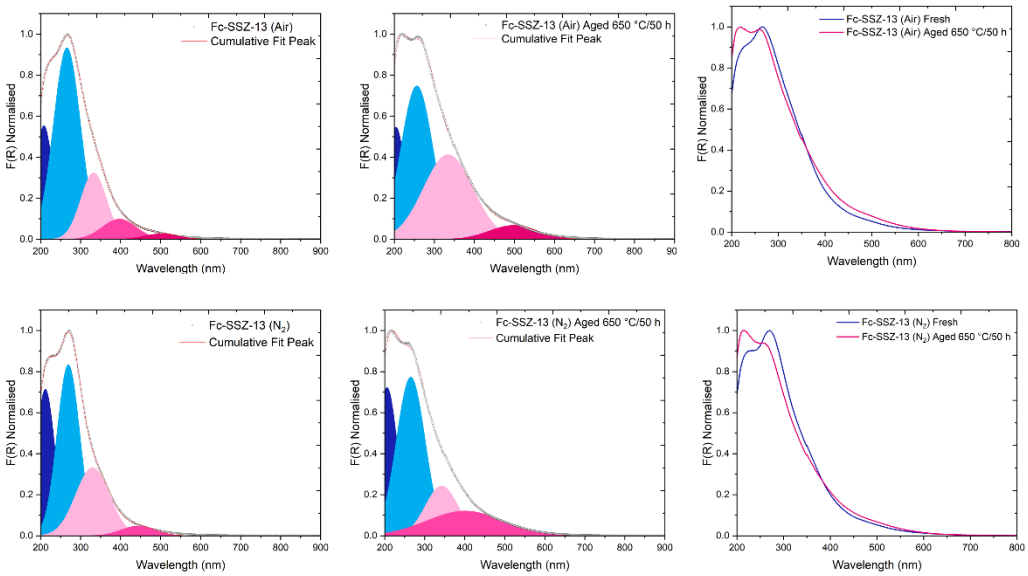

Figure 3-14. DR UV-Vis of (top row) Fc-SSZ-13 (Air) Fresh and Aged (bottom row) Fc-SSZ-13 (N_2) Fresh and Aged. Contributions of isolated Fe species are shown in blue, Fe_xO_y oligomers are shown in light pink and Fe_2O_3 clusters are shown in dark pink

A comparison between fresh and aged Fe-SSZ-13 sample is shown in Figure 3-15. In the aged spectrum the peak around 350 nm disappears and contribution of the peak at around 260 nm increases. This indicates there is a redistribution of Fe species with contribution of dimeric and oligomeric species decreasing and almost disappearing from the spectrum while, the contribution of isolated octahedral species increasing.

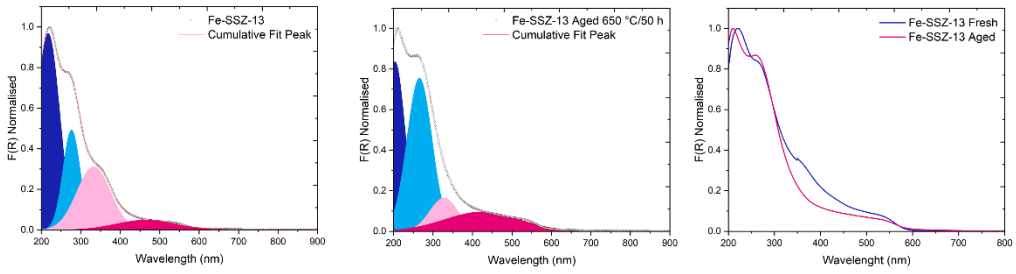

Figure 3-15. DR UV-Vis of Fe-SSZ-13 Fresh and Aged. Contributions of isolated Fe species are shown in blue, Fe_xO_y oligomers are shown in light pink and Fe_2O_3 clusters are shown in dark pink

3.3.3.3 Fe K-edge X-ray absorption near edge spectroscopy

Generally, XANES pre-edge features can elucidate the local electronic structure and local environment of a transition metal such as Fe. Pre-edge features between 7112 and 7114 eV relate to the electron transitions from the 1s→3d orbital and or for the 1s→4p transition.[23-25] Features above 7115 eV are related to extra transitions with 3d orbitals of distant Fe neighbours.[23, 26] However, as the XANES spectra in Figure 3-16 – 3-18 were taken using a bench top analyser the resolution of equipment is not high enough to elucidate between these small differences. As such, comparison spectra between known materials have been used to elucidate the Fe species in the spectra.

The Fe K edge spectra of the fresh and as made samples are shown in Figure 3-16, the spectra of FMTAM I^- has also been included for comparison. All samples show a similar K pre-edge feature at around 7115 eV. The three Fc-SSZ-13 samples are almost identical, indicating the Fe species are similar between the as made and air and N_2 activated samples. A clear difference can be seen in the pre-edge feature for the Fe-SSZ-13 sample, indicating the Fe speciation is different to the Fc-SSZ-13 samples. FMTMA I^- has been included as a comparison for the Fc-SSZ-13 (as made) sample, the pre-edge spectra are quite different although the edge feature is at the same energy. Comparing the spectra, it cannot be conclusively concluded that FMTMA is present in the zeolite.

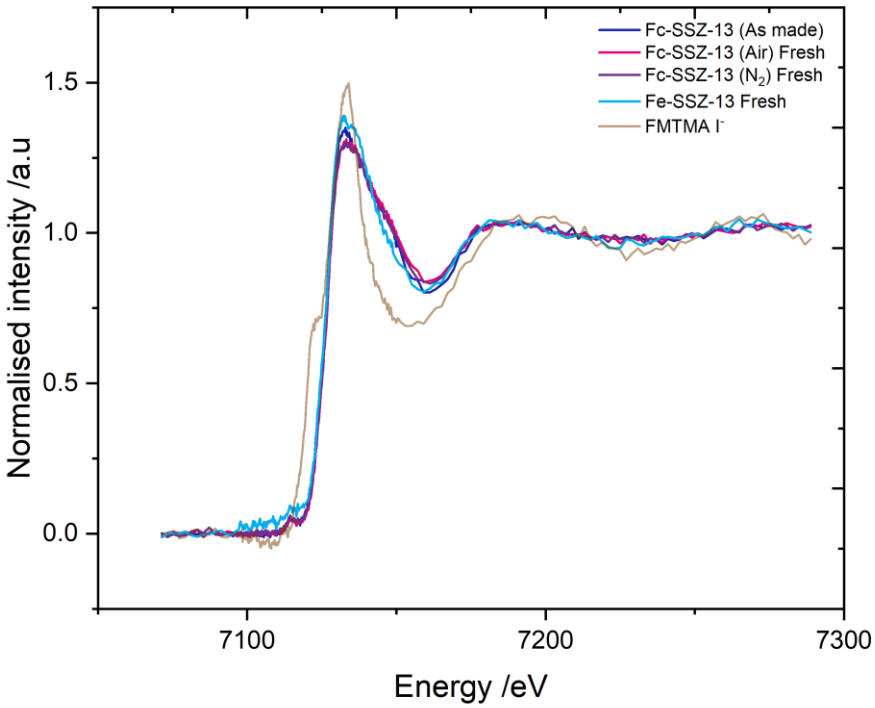

Figure 3-16. Fe K-edge XANES spectra of Fc-SSZ-13 (As made), Fc-SSZ-13 (Air), Fc-SSZ-13 (N_2) and Fe-SSZ-13. FMTMA I^- has been included as comparison

The Fe K edge of the spent and aged Fc-SSZ-13 samples are shown in Figure 3-18, Fe_2O and FeO have been included from the X-Ray Adsorption Library (XASLIB) website.[27] Very little difference can be seen between fresh, spent and aged samples in both the Fc-SSZ-13 (Air) and (N_2) samples. The pre-edge feature at 7115 eV is most like the Fe_2O_3 reference spectra. This suggest that a high contribution of the Fe present in samples are in a similar environment to what can be observed in Fe_2O_3 compared to FeO.

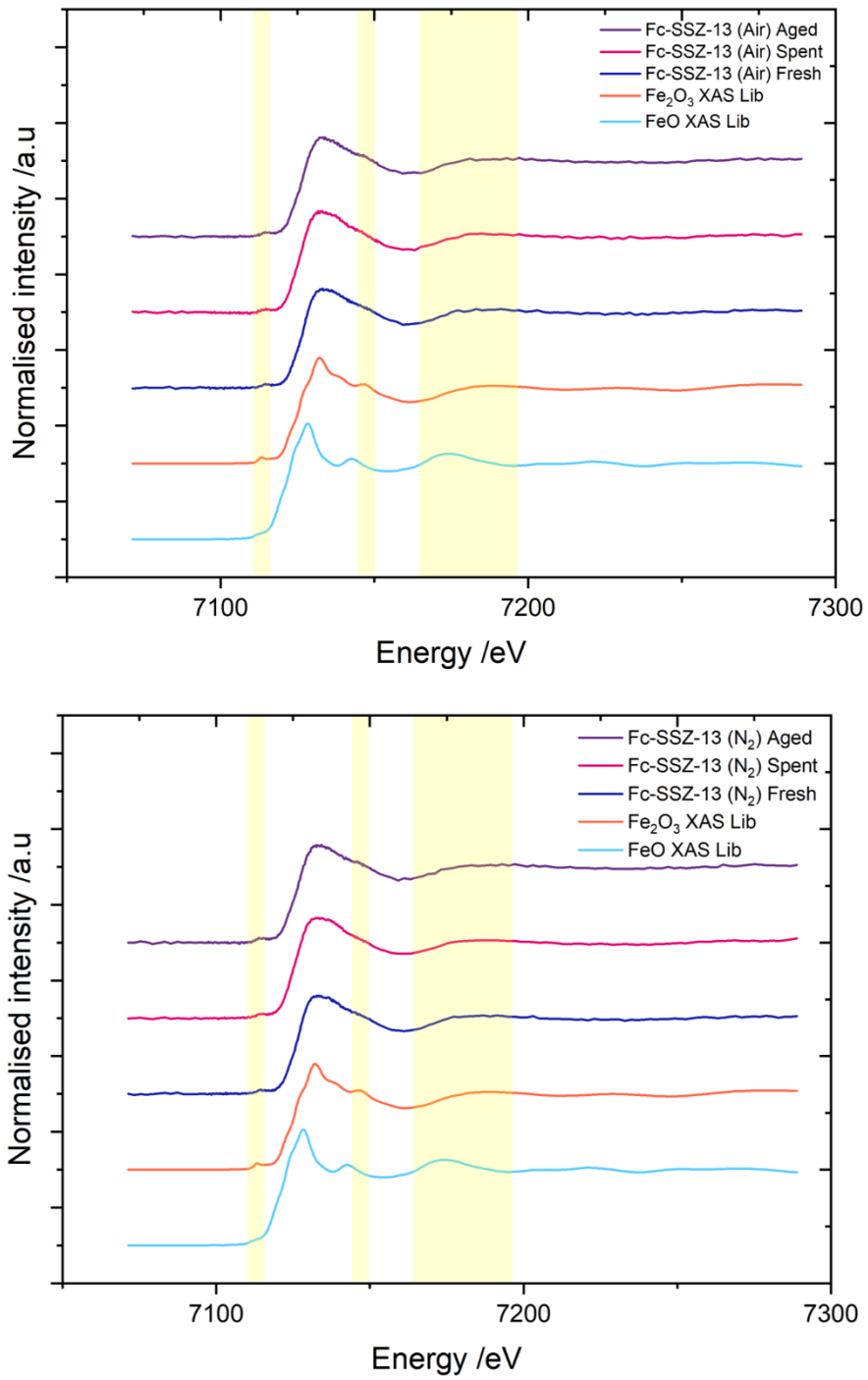

Figure 3-17. Stacked Fe K-edge XANES spectra of (*top*) Fc-SSZ-13 (Air) Fresh, Spent and Aged (*bottom*) Fc-SSZ-13 (N_2) Fresh, Spent and Aged. FeO and Fe_2O_3 from XAS Lib have been included as comparisons

Spectra from Fe-SSZ-13 series are shown in Figure 3-18, these show changes between the spectra, which includes the reduction in the feature at 7115 eV in the aged material, a more prevalent reduction is seen in fresh compared to the spent and aged samples. The features in the spent and aged samples are most similar to the Fe_2O_3 spectra. The features in the fresh sample are less clearly well-defined and can be attributed to both Fe_2O_3 and FeO as well as some other Fe species. Again, similarly to the UV-Vis results we see a redistribution of the Fe species in the Fe-SSZ-13 sample.

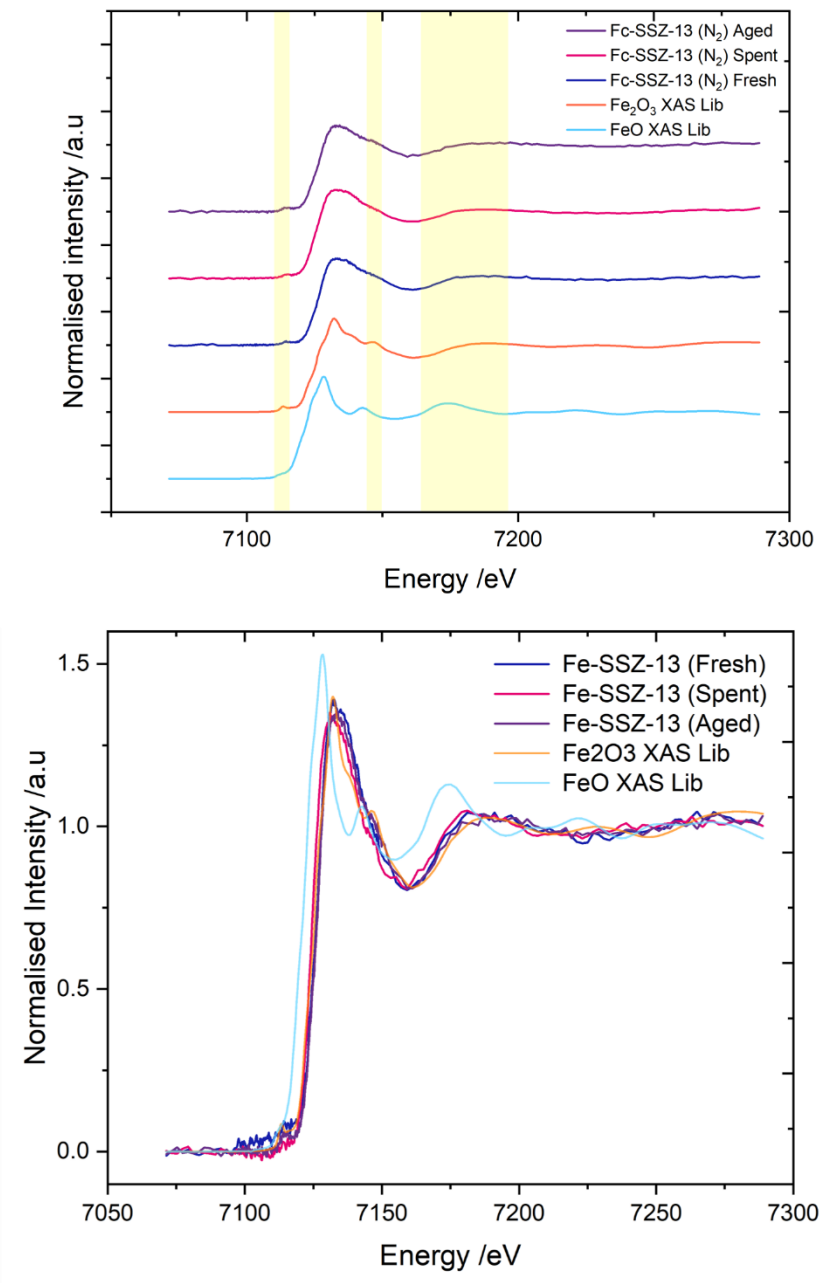

Figure 3-18. (*top*) Stacked Fe K-edge XANES spectra of Fe-SSZ-13 Fresh, Spent and Aged. (*bottom*) Overlayed Fe K-edge XANES spectra of Fe-SSZ-13 Fresh, spent and aged highlighting the changes in the pre-edge feature. FeO and Fe2O3 from XAS Lib have been included as comparisons

3.3.3.4 Mößbauer spectroscopy results

The Mößbauer adsorption spectra for fresh and as made samples are shown in Figure 3-19, simulated Mößbauer parameters and estimated Fe phase percentages are shown in Table 3-7. In the Fc-SSZ-13 samples, three components have been observed. A (super)paramagnetic Fe(III)-doublet designated as Fe(III)-D1 these are attributed to [HO-Fe-O-Fe-OH]$^{+2}$ species.[28] A (super)paramagnetic Fe(II)-doublet designated as Fe(II)-I, these are attributed as isolated high-spin paramagnetic Fe^{2+} ions. And, ferromagnetic and antiferromagnetic Fe(III), collectively designated as Fe(III)-R, which is assigned to either isolated Fe^{3+} species near each other or oligomeric iron oxide species. When two monomeric iron species that are sufficiently close (<15 Å), it leads to enhanced spin interactions which leads to a broad sextet contribution.[10, 28, 29] The low HF vale (< 40 T) suggests isolated Fe^{3+} species[19, 29, 30] however, due to the broad contribution it is difficult to definitively assign the component. These three components appear to be present in similar percentages in all the Fc-SSZ-13 samples, indicating the Fe species are stable and are not changing when calcined in either Air or N_2. The Fe-SSZ-13 contains both the Fe(III)-D1 and Fe(II)-I as in the Fc-SSZ-13 samples, plus two additional contributions from bulk Fe-oxide particles designated as Fe(III)-B and Fe_xO_y clusters designated as Fe(III)-C. Comparing the phase between the Fc-SSZ-13 and the Fe-SSZ-13 samples it is clear the use of the FMTMA SDA in the synthesis of the Fc-SSZ-13 is clearly producing a material with more isolated Fe species and these species are stable after calcination and activation.

Table 3-6. Key outlining the corresponding Mößbauer and Fe species

Mößbauer Phase	Fe species
Fe(II)-I	Isolated Fe^{2+}
Fe(III)-R	Isolated Fe^{3+} located in very close proximity to each other
Fe(III)-D1	[HO-Fe-O-Fe-OH]$^{+2}$
Fe(III)-D2	Dimeric species similar to [HO-Fe-O-Fe-OH]$^{+2}$
Fe(III)-C	Fe clusters
Fe(III)-B	Bulk Fe_xO_y

Table 3-7. Simulated key Mößbauer parameters and estimated percentages of various Fe components in Fc-SSZ-13 (As made), (Air), (N_2) and Fe-SSZ-13 samples

Sample/ Treatment	IS ($mm \cdot s^{-1}$)	QS ($mm \cdot s^{-1}$)	Hyperfine field (T)	Γ ($mm \cdot s^{-1}$)	Phase	Spectral contribution (%)
Fc-SSZ-13 (As made)	0.35	1.12	-	1.40	Fe(III)-D1	48
	1.10	2.90	-	0.60	Fe(II)-I	2
	0.36	-0.45	35.6*	1.46	Fe(III)-R	50
Fc-SSZ-13 (Air) Fresh	0.37	1.31	-	1.48	Fe(III)-D1	41
	1.27	3.36	-	0.58	Fe(II)-I	3
	0.34	0.04	38.9*	1.50	Fe(III)-R	56
Fc-SSZ-13 (N_2) Fresh	0.36	1.33	-	1.48	Fe(III)-D1	45
	1.27	3.36	-	0.58	Fe(II)-I	4
	0.49	0.02	38.1*	1.40	Fe(III)-R	51
Fe-SSZ-13 Fresh	0.32	0.41	54.2	0.61	Fe(III)-B	23
	0.41	0.91	-	0.71	Fe(III)-D1	24
	1.27	3.25	-	0.48	Fe(II)-I	7
	0.35	0.00	38.6*	1.24	Fe(III)-R	46

*Average magnetic field

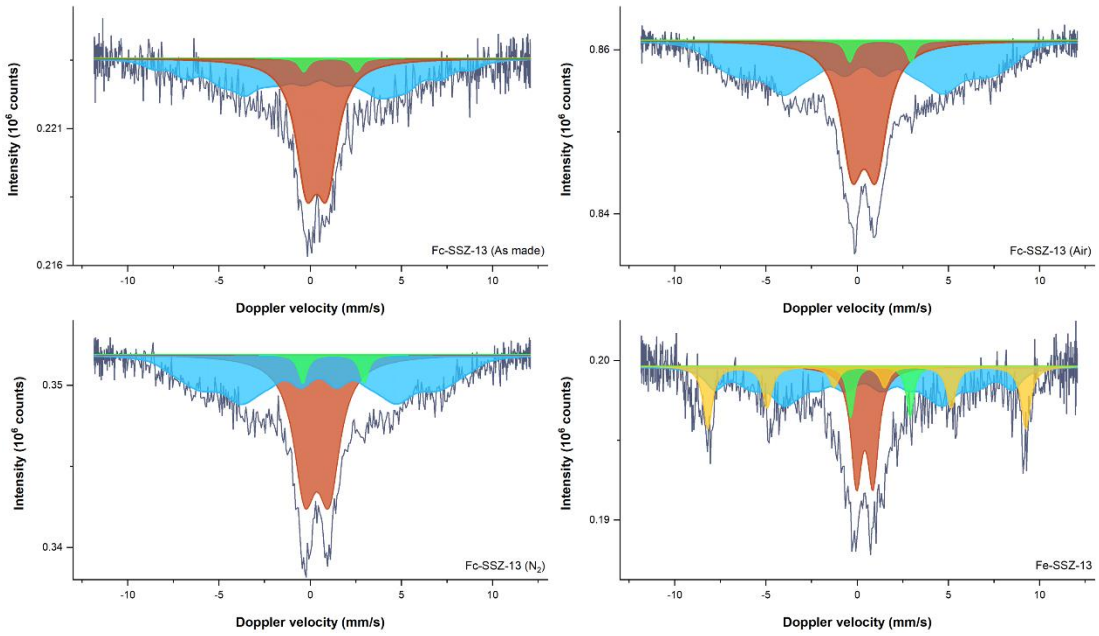

Figure 3-19. Mößbauer spectra with corresponding fits of Ferrcocene-SSZ-13 (As made), (Air), (N_2) and Fe-SSZ-13

The Mößbauer adsorption spectra for the fresh, spent and aged Fc-SSZ-13 samples are shown in Figure 3-20, simulated Mößbauer parameters and estimated Fe phase percentages are shown in Table 3-8. Both the Air and N_2 samples exhibit similar changes in the corresponding spent and aged samples. Comparing fresh and spent samples there is a clear

change in Fe speciation, the Fe(III)-D1 and Fe(III)-R convert to mainly Fe(III)-C species. This indicates the Fe is mobile as the $[HO\text{-}Fe\text{-}O\text{-}Fe\text{-}OH]^{+2}$ species and isolated Fe^{3+} species are sintering into larger Fe clusters. The spent samples also include another component designated as Fe(III)-D2 which has similar parameters as Fe(III)-D1 except it has a much larger quadrupole splitting (QS). This change in QS indicates a change in the electronic environment and therefore changes to the $[HO\text{-}Fe\text{-}O\text{-}Fe\text{-}OH]^{+2}$ complex. The spent samples also include isolated Fe^{2+} assigned as Fe(II)-I, the SCR reaction is likely reducing some of the isolated Fe^{3+} in the zeolites to Fe^{2+} although is only make up around 10% of the total Fe species in the sample. Comparing the fresh and aged samples, again, there is a clear change in Fe speciation with the Fe(III)-D1 and Fe(III)-R convert to Fe(III)-C species. Unlike in the spent samples, the aged samples do not contain isolated Fe^{2+} as indicted by the absence of Fe(II)-I, the ageing conditions are too oxidative and any Fe^{2+} present is oxidised.

Table 3-8. Simulated key Mößbauer parameters and estimated percentages of various Fe components in fresh spent and aged Fc-SSZ-13 (Air) and (N_2) samples

Sample/ Treatment	IS ($mm{\cdot}s^{-1}$)	QS ($mm{\cdot}s^{-1}$)	Hyperfine field (T)	Γ ($mm{\cdot}s^{-1}$)	Phase	Spectral contribution (%)
Fc-SSZ-13 (Air) Fresh	0.37	1.31	-	1.48	Fe(III)-D1	41
	1.27	3.36	-	0.58	Fe(II)-I	3
	0.34	0.04	38.9*	1.50	Fe(III)-R	56
Fc-SSZ-13 (Air) Spent	0.43	1.06	-	0.80	Fe(III)-D1	11
	0.30	2.60	-	0.80	Fe(III)-D2	7
	1.27	3.35	-	0.45	Fe(II)-I	9
	0.35	0.00	41.0*	1.40	Fe(III)-C	73
Fc-SSZ-13 (Air) Aged	0.32	0.96	-	0.80	Fe(III)-D1	16
	0.30	2.44	-	0.80	Fe(III)-D2	5
	0.35	0.00	45.4*	0.93	Fe(III)-C	79
Fc-SSZ-13 (N_2) Fresh	0.36	1.33	-	1.48	Fe(III)-D1	45
	1.27	3.36	-	0.58	Fe(II)-I	4
	0.49	0.02	38.1*	1.40	Fe(III)-R	51
Fc-SSZ-13 (N_2) Spent	0.40	1.01	-	0.80	Fe(III)-D1	7
	0.34	2.45	-	0.80	Fe(III)-D2	6
	1.28	3.33	-	0.45	Fe(II)-I	11
	0.35	0.00	41.1*	1.38	Fe(III)-C	76
Fc-SSZ-13 (N_2) Aged	0.31	0.95	-	0.80	Fe(III)-D1	14
	0.31	2.31	-	0.80	Fe(III)-D2	7
	0.35	0.00	45.1*	0.97	Fe(III)-C	79

*Average magnetic field

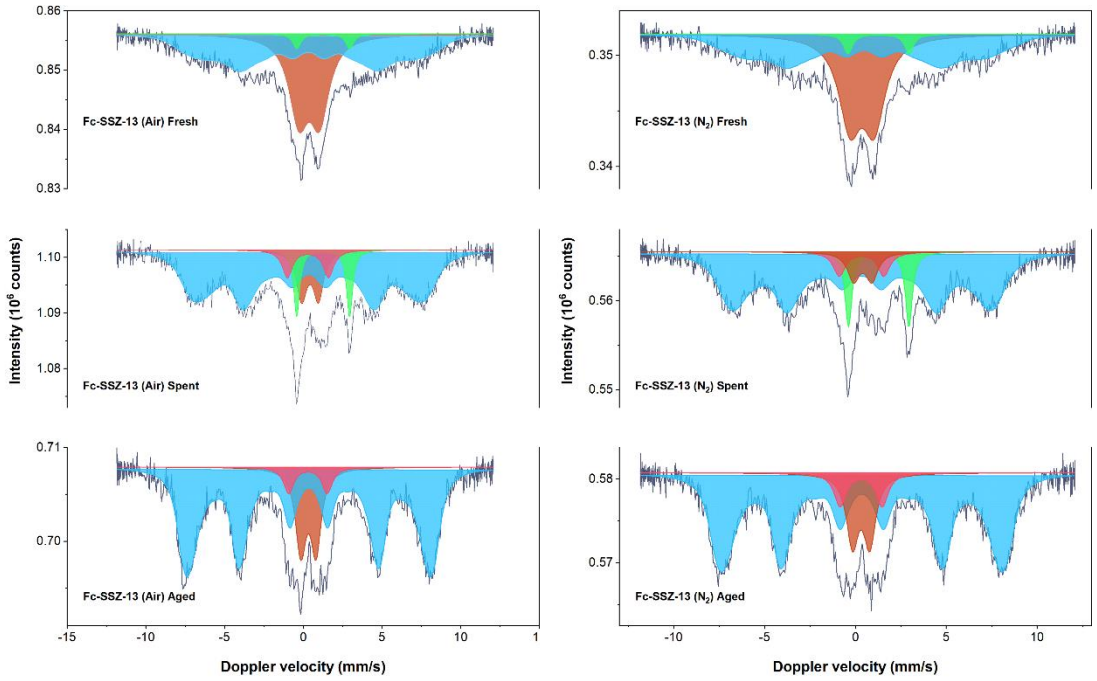

Figure 3-20. Mößbauer spectra of (left) Fc-SSZ-13 (Air) Fresh, Spent and Aged (right) Fc-SSZ-13 (N_2) Fresh, Spent and Aged

The Mößbauer adsorption spectra for the fresh, spent and aged Fe-SSZ-13 sample is shown in Figure 3-21, simulated Mößbauer parameters and estimated Fe phase percentages are shown in Table 3-9. A change in the speciation can be seen between the fresh and spent samples where some of the Fe(III)-R component is replaced by Fe(III)-C in the spent sample. Indicating the isolated Fe^{3+} species sintering into Fe clusters. The Fe(II)-I component also increases in the spent sample, likely caused be the reduction of the isolated Fe^{3+} species to isolated Fe^{2+} during the SCR reaction. The same species are present in the aged samples as in the spent sample however the ratio of these species is quite different. Again, the Fe(III)-R component is replaced by Fe(III)-C however unlike in the spent sample the amount of isolated Fe^{2+} is very low as indicted by Fe(II)-I and, instead, the amount of $[HO\text{-}Fe\text{-}O\text{-}Fe\text{-}OH]^{+2}$ indicated by Fe(III)-D1 has increased. The oxidising conditions of the aging process has prevented the reduction of isolated Fe^{3+} to Fe^{2+}. Unlike in the spent sample not all of the isolated species have converted to clusters some have converted to more $[HO\text{-}Fe\text{-}O\text{-}Fe\text{-}OH]^{+2}$ dimers. Bulk Fe oxide species (Fe(III)-B) do not change in either the spent or aged samples and likely do not contribute to the SCR reaction.

Table 3-9. Simulated key Mößbauer parameters and estimated percentages of various Fe components in fresh spent and aged Fe-SSZ-13 samples

Sample/ Treatment	IS ($mm \cdot s^{-1}$)	QS ($mm \cdot s^{-1}$)	Hyperfine field (T)	Γ ($mm \cdot s^{-1}$)	Phase	Spectral contribution (%)
Fe-SSZ-13 Fresh	0.32	0.41	54.2	0.61	Fe(III)-B	23
	0.41	0.91	-	0.71	Fe(III)-D1	24
	1.27	3.25	-	0.48	Fe(II)-I	7
	0.35	0.00	38.6*	1.24	Fe(III)-R	46
Fe-SSZ-13 Spent	0.37	0.36	54.2	0.36	Fe(III)-B	25
	0.40	0.96	-	0.82	Fe(III)-D1	17
	1.26	3.29	-	0.52	Fe(II)-I	31
	0.38	0.00	41.4*	1.39	Fe(III)-C	27
Fe-SSZ-13 Aged	0.36	0.41	54.3	0.34	Fe(III)-B	24
	0.33	1.00	-	0.76	Fe(III)-D1	43
	1.26	3.30	-	0.53	Fe(II)-I	3
	0.38	0.00	40.5*	0.78	Fe(III)-C	30

*Average magnetic field

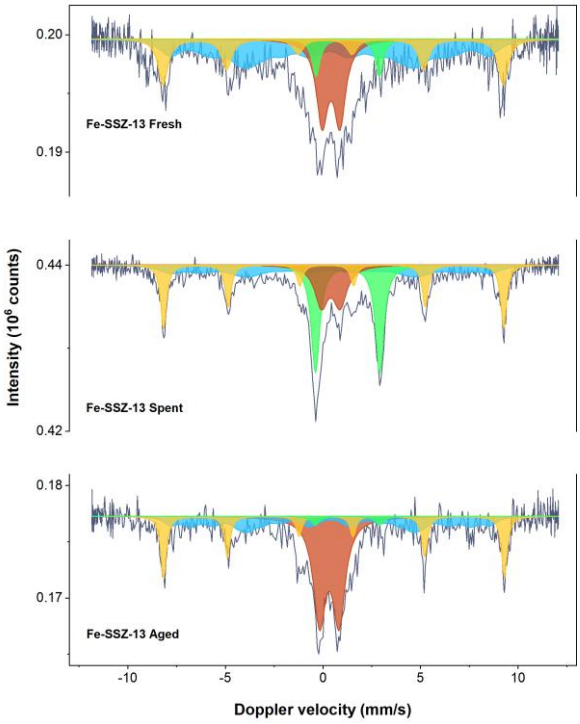

Figure 3-21. Mößbauer spectra of Fe-SSZ-13 Fresh, Spent and Aged

3.4 Conclusions

The Fc-SSZ-13 samples have been examined and compared to a benchmark Fe-SSZ-13 sample. Characterisation of the fresh samples shows the ferrocene samples produce a material with a mixture of isolated Fe^{3+} and dimeric $[HO\text{-}Fe\text{-}O\text{-}Fe\text{-}OH]^{+2}$ species with very few isolated Fe^{2+} species. Fe speciation does not change significantly upon calcination in either Air or N_2 this shows the species are formed during the synthesis and these species are stable under the calcination conditions. The fresh Fe-SSZ-13 sample contains a mixture of different dimers, isolated Fe^{3+} species and bulk iron oxide particles. These samples are prepared post calcination, so the stability of these species post calcination is not known. However, there is a much greater heterogenous distribution of Fe species in these samples compared to the Ferrocene samples.

NH_3 – SCR catalytic activity testing shows the Fe-SSZ-13 is the most active in both fresh and aged testing. Fc-SSZ-13 (N_2) showed comparable fresh activity with Fe-SSZ-13, while Fc-SSZ-13 (Air) had significantly lower fresh activity than both Fc-SSZ-13 (N_2) and Fe-SSZ-13. It is unclear why the air calcined sample was less active than the N_2 calcined as both show comparable fresh Fe speciation.

Clear differences were seen in the catalytic activity of the aged samples. Aged Fe-SSZ-13 had a significantly higher catalytic activity of the both the Fc-SSZ-13 samples, and, surprisingly, was more active than the fresh Fe-SSZ-13. This higher activity is due to a redistribution of the Fe species in the sample, confirmed by DR-UV-Vis, Fe K-edge XANES and Mößbauer spectroscopies. It was found that all the isolated Fe^{3+} species in the fresh sample convert to dimeric $[HO\text{-}Fe\text{-}O\text{-}Fe\text{-}OH]^{+2}$ species and Fe clusters. It is likely these dimeric $[HO\text{-}Fe\text{-}O\text{-}Fe\text{-}OH]^{+2}$ species are contributing to the increased activity.

Both aged Fc-SSZ-13 samples exhibited deactivation caused by the conversion of isolated and dimeric Fe species to clusters. Deactivation is thought to be caused by hydrothermal aging detaching isolated Fe^{3+} from ion-exchange positions leading to the formation of clusters.[31-35]

References

1. R. Q. Long and R. T. Yang, *Journal of the American Chemical Society*, 1999, **121**, 5595-5596.
2. R. Q. Long and R. T. Yang, *Journal of Catalysis*, 1999, **188**, 332-339.
3. M. Colombo, I. Nova and E. Tronconi, *Catal. Today*, 2010, **151**, 223-230.
4. Q. Ye, L. Wang and R. T. Yang, *Applied Catalysis A: General*, 2012, **427-428**, 24-34.
5. B. Coq, M. Mauvezin, G. Delahay, J.-B. Butet and S. Kieger, *Applied Catalysis B: Environmental*, 2000, **27**, 193-198.
6. M. Devadas, O. Krocher, M. Elsener, A. Wokaun, N. Soger, M. Pfeifer, Y. Demel and L. Mussmann, *Applied Catalysis B: Environmental*, 2006, **67**, 187-196.
7. S. A. Stevenson, J. C. Vartuli and C. F. Brooks, *Journal of Catalysis*, 2000, **190**, 228-239.
8. F. Gao, Y. Zheng, R. K. Kukkadapu, Y. Wang, E. D. Walter, B. Schwenzer, J. Szanyi and C. H. F. Peden, *ACS Catalysis*, 2016, **6**, 2939-2954.
9. F. Gao, J. Szanyi, Y. Wang, B. Schwenzer, M. Kollár and C. H. F. Peden, *Top. Catal.*, 2016, **59**, 882-886.
10. F. Gao, M. Kollár, R. K. Kukkadapu, N. M. Washton, Y. Wang, J. Szanyi and C. H. F. Peden, *Applied Catalysis B: Environmental*, 2015, **164**, 407-419.
11. K. Kamasamudram, N. Currier, T. Szailer and A. Yezerets, *SAE International Journal of Fuels and Lubricants*, 2010, **3**, 664-672.
12. J. Li and S. Li, *The Journal of Physical Chemistry C*, 2008, **112**, 16938-16944.
13. P. Zimmermann, S. Peredkov, P. M. Abdala, S. DeBeer, M. Tromp, C. Müller and J. A. van Bokhoven, *Coordination Chemistry Reviews*, 2020, **423**.
14. E. P. Jahrman, W. M. Holden, A. S. Ditter, D. R. Mortensen, G. T. Seidler, T. T. Fister, S. A. Kozimor, L. F. J. Piper, J. Rana, N. C. Hyatt and M. C. Stennett, *Rev. Sci. Instrum.*, 2019, **90**.
15. Z. Klencsár, *Nuclear Instruments and Methods in Physics Research Section B: Beam Interactions with Materials and Atoms*, 1997, **129**, 527-533.
16. Y. Román-Leshkov, M. Moliner and M. E. Davis, *The Journal of Physical Chemistry C*, 2010, **115**, 1096-1102.
17. P. S. Bagus, C. J. Nelin, C. R. Brundle, B. V. Crist, N. Lahiri and K. M. Rosso, *The Journal of Chemical Physics*, 2021, **154**.
18. L. Čapek, V. Kreibich, J. Dědeček, T. Grygar, B. Wichterlová, Z. Sobalík, J. A. Martens, R. Brosius and V. Tokarová, *Microporous and Mesoporous Materials*, 2005, **80**, 279-289.
19. S. Dzwigaj, L. Stievano, F. E. Wagner and M. Che, *J. Phys. Chem. Solids*, 2007, **68**, 1885-1891.
20. S. Bordiga, R. Buzzoni, F. Geobaldo, C. Lamberti, E. Giamello, A. Zecchina, G. Leofanti, G. Petrini, G. Tozzola and G. Vlaic, *Journal of Catalysis*, 1996, **158**, 486-501.
21. P. Wu, T. Komatsu and T. Yashima, *Microporous and Mesoporous Materials*, 1998, **20**, 139-147.
22. J. Zeng, Y. Wang, F. Diao, L. Qiu and H. Chang, *Catalysis Surveys from Asia*, 2020, **25**, 58-67.
23. G. Dräger, R. Frahm, G. Materlik and O. Brümmer, *physica status solidi (b)*, 2006, **146**, 287-294.
24. T. E. Westre, P. Kennepohl, J. G. DeWitt, B. Hedman, K. O. Hodgson and E. I. Solomon, *Journal of the American Chemical Society*, 1997, **119**, 6297-6314.
25. F. Requejo, *Applied Catalysis A: General*, 2004, **266**, 147-153.
26. A. Battiston, *Journal of Catalysis*, 2003, **213**, 251-271.
27. XASLIB: The X-ray Absorption Data Library https://docs.xrayabsorption.org/xaslib/index.html, (accessed 24/08, 2023).

28. L. Kovarik, N. M. Washton, R. Kukkadapu, A. Devaraj, A. Wang, Y. Wang, J. Szanyi, C. H. F. Peden and F. Gao, *ACS Catalysis*, 2017, **7**, 2458-2470.
29. J. A. Morice and L. V. C. Rees, *Trans. Faraday Soc.*, 1968, **64**, 1388-1395.
30. T. Zhang, Y. Qiu, G. Liu, J. Chen, Y. Peng, B. Liu and J. Li, *Journal of Catalysis*, 2020, **392**, 322-335.
31. F. Buttignol, D. Rentsch, I. Alxneit, A. Garbujo, P. Biasi, O. Kröcher and D. Ferri, *Catalysis Science & Technology*, 2022, **12**, 7308-7321.
32. S. Brandenberger, O. Kröcher, M. Casapu, A. Tissler and R. Althoff, *Applied Catalysis B: Environmental*, 2011, **101**, 649-659.
33. A. Wang, Y. Wang, E. D. Walter, N. M. Washton, Y. Guo, G. Lu, C. H. F. Peden and F. Gao, *Catal. Today*, 2019, **320**, 91-99.
34. A. Shishkin, H. Kannisto, P.-A. Carlsson, H. Härelind and M. Skoglundh, *Catal. Sci. Technol.*, 2014, **4**, 3917-3926.
35. S. Shwan, J. Jansson, J. Korsgren, L. Olsson and M. Skoglundh, *Catal. Today*, 2012, **197**, 24-37.

Chapter 4 . Summary

As stricter vehicle NO_x emission regulations come into force around the world, catalytic materials will need to be developed that are more selective, with higher activities and with increased stability. While Cu-exchanged zeolites have been preferred for NH_3-SCR as they are more active at lower temperatures and have excellent hydrothermal stability, Fe-exchanged zeolites show improved higher temperature SCR activity and are more selective to N_2 than Cu-exchange zeolites. Low temperature NH_3-SCR activity in Fe zeolites is generally thought to be catalysed by isolated monomeric Fe species. Producing monomeric Fe species in zeolites is a major challenge due to the reactivity of Fe. Therefore, developing a method to produce an Fe zeolite with isolated monomeric Fe was examined in this work.

The FMTMA complex was used to attempt to produce a well-defined Fe-SSZ-13. The use of FMTMA is not straight forward, during the development of the synthesis it was found the FMTMA OH^- complex is photoactive and rapidly degrades if not shielded from light. The FMTMA complex itself is also not a strong enough OSDA on its own and a second OSDA is needed to produce a SSZ-13 material. TEA OH^- was used in combination with FMTMA OH^- as TMAdmA OH^- was found to be too strong and dominating when used with FMTMA OH^-. The final material was not phase pure, Rietveld analysis of the pXRD pattern calculated the samples contained 15.3 wt% of MOR. Additionally, SEM images of sample revealed a mixture of small not well-defined crystals with large slab like crystals thought to be MOR. Fe distribution as seen by elemental mapping shows little Fe present in this large MOR crystals suggesting these crystals form after all the FMTMA has been consumed. Further optimisation of the synthesis conditions may be able to produce a phase pure product, however it is unlikely the FMTMA template can be used on its own in the synthesis of a Fe-SSZ-13.

The material synthesised was structurally stable after calcination. There is a suggestion in the ssNMR that some of the FMTMA template remains intact in the as-made material, however this is not supported by other characterisation techniques such as XANES or Mößbauer. Mößbauer spectroscopy of the as-made material indicates there is an approximate 50:50 ratio of isolated Fe^{3+} and dimeric $[HO\text{-}Fe\text{-}O\text{-}Fe\text{-}OH]^{+2}$ species, a very small amount of isolated Fe^{2+} is also seen in the samples however this is present in such low quantities it's not considered significant.

As no evidence of FMTMA is seen in the Mößbauer analysis of the as-made material it is likely the FMTMA molecule degrades during the synthesis. FMTMA may degrade to form some other complex that contains the Fe, as, in the as-made material the Fe is homogenously distributed with isolated and dimeric Fe species, free Fe would likely cluster and agglomerate. The speciation does not change substantially after calcination in either air or N_2 therefore, any future development work to change the speciation should in the first instance focus on the synthesis of the Fc-SSZ-13 rather than the calcination conditions.

Calcined Fc-SSZ-13 samples were activated and tested in the standard NH_3-SCR reaction along with a benchmark Fe-SSZ-13 sample that was synthesised using a traditional incipient wetness impregnation method. Mößbauer analysis of the benchmark sample shows the sample contains around 60 % isolated Fe species, 20 % dimeric species and 20 % bulk iron oxide, isolated species are split 50 % Fe^{3+} and 10% Fe^{2+}. The most active sample was the benchmark Fe-SSZ-13 sample followed closely by the Fc-SSZ-13 (N_2) the Fc-SSZ-13 (Air) sample was significantly poorer. The cause of the poorer activity for Fc-SSZ-13 (Air) is unknown considering it shares the same parent materials as Fc-SSZ-13 (N_2) and Mößbauer spectroscopy of the fresh and spent material showed very similar Fe speciation in both samples. The oxidative nature of the air calcination may have damaged the structure of the zeolite while pXRD does show an increase in the MOR phase based on the relative comparison of the CHA peak of the spent material the same increase is also seen in the N_2 sample. At this point the cause of the poorer performance of the air sample compared to the N_2 sample cannot be determined.

Fresh samples were hydrothermally aged at 650 °C and then tested for the standard NH_3-SCR reaction. Like the fresh samples, Fe-SSZ-13 was the most active and actually showed an increase in activity. This increase in activity is due to a redistribution of the Fe species in the sample. Mößbauer shows an increase in the active dimeric $[HO\text{-}Fe\text{-}O\text{-}Fe\text{-}OH]^{+2}$ species vs the fresh sample. Both Fc-SSZ-13 samples performed much worse than their fresh counter parts. Again, a distribution of the Fe species is seen in the sample, however for these samples more Fe clusters are formed which as much less active for NH_3-SCR.

Based on these results, the FMTMA template used in a one pot method does not produce a stable material that is suitable for the standard NH_3-SCR reaction. Further work should focus on optimising the conditions to prevent the degradation of the template during the synthesis of the zeolite. The materials produced using the conditions developed in this work should be

tested for other reactions such as fast SCR or methane oxidation to methanol as they did produce a homogenously distributed Fe Zeolite and may be more stable for those reactions.

Appendix

Appendix i. Table of experimental zeolite synthesis

	Mol							
Sample name	**SiO_2**	**Al_2O_3**	**Na_2O**	**K_2O**	**FMTMA I^-/ OH^-**	**H_2O**	**TMAdmA OH^-/TEA OH^-**	**Phases**
ZEO1 A	68.0	1.5	21.0	0.0	**0.5**	580.0	2.5	FAU,CHA,GIS,MOR
ZEO1 B	68.0	1.5	21.0	0.0	**1.0**	580.0	2.0	FAU,CHA,GIS,MOR
ZEO1 C	68.0	1.5	21.0	0.0	**1.5**	580.0	1.5	FAU,CHA,GIS,MOR
ZEO1 D	68.0	1.5	21.0	0.0	**2.0**	580.0	1.0	FAU,CHA,GIS,MOR
ZEO2 A	68.0	1.5	21.0	0.0	**2.5**	580.0	0.5	CHA,GIS,MOR
ZEO2 B	68.0	1.5	21.0	0.0	**3.0**	580.0	0.0	CHA,GIS
ZEO2 C	68.0	1.5	23.5	0.0	**2.5**	580.0	0.5	CHA,GIS
ZEO2 D	68.0	1.5	24.0	0.0	**3.0**	580.0	0.0	CHA,GIS
ZEO3 A	68.0	1.5	21.0	0.0	**0.5**	580.0	2.5	CHA
ZEO3 B	68.0	1.5	21.0	0.0	**1.0**	580.0	2.0	CHA
ZEO3 C	68.0	1.5	21.0	0.0	**1.5**	580.0	1.5	CHA
ZEO3 D	68.0	1.5	21.0	0.0	**2.0**	580.0	1.0	CHA,GIS
ZEO4 A	68.0	1.5	21.0	0.0	**3.0**	580.0	0.0	CHA,GIS,MOR
ZEO4 B	68.0	1.5	21.0	0.0	**2.0**	770.0	1.0	CHA,GIS,MOR
ZEO4 C	68.0	1.5	21.0	0.0	**2.0**	870.0	1.0	CHA,GIS,MOR
ZEO4 D	68.0	1.5	21.0	0.0	**3.0**	870.0	0.0	MOR
ZEO5 A	68.0	1.5	0.0	21.0	**3.0**	870.0	0.0	CHA,MOR
ZEO5 B	68.0	1.5	0.0	21.0	**0.0**	870.0	3.0	CHA
ZEO5 C	68.0	1.5	0.0	21.0	**3.0**	870.0	0.0	Amorphous
ZEO5 D	68.0	1.5	0.0	21.0	**0.0**	870.0	3.0	CHA,FAU
ZEO6 A	68.0	1.5	0.0	21.0	**3.0**	950.0	0.0	MOR
ZEO6 B	68.0	1.5	0.0	21.0	**3.0**	870.0	0.0	MOR
ZEO6 C	68.0	1.5	0.0	21.0	**3.0**	870.0	0.0	Amorphous
ZEO6 D	68.0	1.5	0.0	21.0	**3.0**	870.0	0.0	Amorphous
ZEO7 A	68.0	1.5	0.0	21.0	**3.0**	6500.0	0.0	FAU
ZEO7 B	68.0	1.5	0.0	21.0	**1.5**	3600.0	1.5	FAU
ZEO7 C	68.0	1.5	0.0	21.0	**3.0**	6400.0	0.0	FAU
ZEO7 D	68.0	1.5	21.0	0.00	**3.0**	6500.0	0.0	Unknown
ZEO8 A	68.0	1.5	0.0	21.0	**3.0**	580.0	0.0	Amorphous
ZEO8 B	68.0	1.5	0.0	30.0	**3.0**	6400.0	0.0	Amorphous,FAU
ZEO8 C	68.0	1.5	0.0	40.0	**3.0**	6400.0	0.0	Amorphous,FAU
ZEO8 D	68.0	1.5	0.0	50.0	**3.0**	6400.0	0.0	Low crys CHA
ZEO9 A	68.0	1.5	0.0	50.0	**3.0**	6700.0	0.0	Potassium silicate
ZEO9 B	68.0	1.5	0.0	50.0	**3.0**	6700.0	0.0	Potassium silicate
ZEO9 C	68.0	1.5	0.0	50.0	**3.0**	6700.0	0.0	Potassium silicate
ZEO9 D	68.0	1.5	0.0	50.0	**3.0**	6700.0	0.0	Potassium silicate
ZEO10 A	68.0	1.5	0.0	50.0	**3.0**	6400.0	0.0	Potassium silicate
ZEO10 B	68.0	1.5	0.0	50.0	**3.0**	6400.0	0.0	Potassium silicate
ZEO10 C	68.0	1.5	0.0	50.0	**3.0**	6400.0	0.0	Potassium silicate
ZEO10 D	68.0	1.5	0.0	50.0	**3.0**	6400.0	0.0	Potassium silicate
ZEO11 A	68.0	1.5	0.0	230.0	**3.0**	6400.0	0.0	Potassium silicate

ZEO11 B	68.0	1.5	0.0	230.0	**3.0**	6400.0	0.0	Potassium silicate
ZEO11 C	68.0	1.5	0.0	50.0	**3.0**	6400.0	0.0	Potassium silicate
ZEO11 D	68.0	1.5	0.0	50.0	**3.0**	6400.0	0.0	Potassium silicate
ZEO12 A	68.0	1.5	0.0	50.0	**3.0**	6400.0	0.0	Potassium silicate
ZEO12 B	68.0	1.5	0.0	80.0	**3.0**	6450.0	0.0	Potassium silicate
ZEO12 C	68.0	1.5	0.0	100.0	**3.0**	6500.0	0.0	Potassium silicate
ZEO12 D	68.0	1.5	0.0	150.0	**3.0**	6550.0	0.0	Potassium silicate
ZEO13 A	68.0	1.5	0.0	80.0	**3.0**	6450.0	0.0	Potassium silicate
ZEO13 B	68.0	1.5	0.0	80.0	**3.0**	6450.0	0.0	Potassium silicate
ZEO13 C	68.0	1.5	0.0	80.0	**3.0**	6450.0	0.0	Potassium silicate
ZEO13 D	68.0	1.5	0.0	80.0	**3.0**	6450.0	0.0	Potassium silicate
ZEO14 A	68.0	1.5	0.0	50.0	**3.0**	6450.0	0.0	Potassium silicate
ZEO14 B	68.0	1.5	0.0	55.0	**3.0**	6450.0	0.0	Potassium silicate
ZEO14 C	68.0	1.5	0.0	60.0	**3.0**	6450.0	0.0	Potassium silicate
ZEO14 D	68.0	1.5	0.0	70.0	**3.0**	6450.0	0.0	Potassium silicate
ZEO15 A	68.0	1.5	0.0	50.0	**3.0**	6450.0	0.0	Potassium silicate
ZEO15 B	68.0	1.5	0.0	55.0	**3.0**	6450.0	0.0	Potassium silicate
ZEO15 C	68.0	1.5	0.0	60.0	**3.0**	6450.0	0.0	Potassium silicate
ZEO15 D	68.0	1.5	0.0	70.0	**3.0**	6450.0	0.0	Potassium silicate
ZEO16 A	68.0	1.5	0.0	51.0	**3.0**	6450.0	0.0	Potassium silicate
ZEO16 B	68.0	1.5	0.0	52.0	**3.0**	6450.0	0.0	Potassium silicate
ZEO16 C	68.0	1.5	0.0	53.0	**3.0**	6450.0	0.0	Potassium silicate
ZEO16 D	68.0	1.5	0.0	54.0	**3.0**	6450.0	0.0	Potassium silicate
ZEO17 A	68.0	1.5	0.0	10.0	**3.0**	1600.0	0.0	Amorphous
ZEO17 B	68.0	1.5	0.0	15.0	**3.0**	1600.0	0.0	Amorphous
ZEO17 C	68.0	1.5	0.0	20.0	**3.0**	1600.0	0.0	Amorphous
ZEO17 D	68.0	1.5	0.0	30.0	**3.0**	1600.0	0.0	Unknown
ZEO18 A	68.0	1.5	0.0	30.0	**3.0**	1650.0	0.0	Potassium silicate
ZEO18 B	68.0	1.5	0.0	35.0	**3.0**	1650.0	0.0	Potassium silicate
ZEO18 C	68.0	1.5	0.0	30.0	**3.0**	1650.0	0.0	Potassium silicate
ZEO18 D	71.0	1.8	0.0	28.0	**3.0**	1650.0	0.0	Potassium silicate
ZEO19 A	68.0	1.5	21.0	0.0	3.0	1080.0	0.00	MOR
ZEO19 B	68.0	1.5	21.0	0.0	3.0	1100.0	0.00	MOR
ZEO19 C	68.0	1.5	21.0	0.0	3.0	1150.0	0.00	MOR
ZEO19 D	68.0	1.5	21.0	0.0	3.0	1200.0	0.00	MOR
ZEO20 A	68.0	1.5	21.0	0.0	**0.5**	580.0	**2.5**	CHA,MOR
ZEO20 B	68.0	1.5	21.0	0.0	**1.0**	580.0	**2.0**	CHA,MOR
ZEO20 C	68.0	1.5	21.0	0.0	**1.5**	580.0	**1.5**	CHA,MOR
ZEO20 D	68.0	1.5	21.0	0.0	**2.0**	580.0	**1.0**	MOR
ZEO21 A	68.00	1.50	0.0	30.00	**0.50**	675.00	**2.50**	Potassium silicate
ZEO21 B	68.00	1.50	0.0	30.00	**1.00**	825.00	**2.00**	Potassium silicate
ZEO21 C	68.00	1.50	0.0	30.00	**1.50**	980.00	**1.50**	Potassium silicate
ZEO21 D	68.00	1.50	0.0	30.00	**2.00**	1140.00	**1.00**	Potassium silicate
ZEO22 A	68.0	1.5	20.0	0.0	**1.5**	750.0	**1.5**	CHA,MOR
ZEO22 B	68.0	1.5	20.0	0.0	**2.0**	750.0	**1.0**	MOR
ZEO22 C	68.0	1.5	11.5	3.5	**1.5**	750.0	**1.5**	CHA
ZEO22 D	68.0	1.5	11.5	3.5	**2.0**	750.0	**1.0**	CHA,MOR
ZEO23 A	68.0	1.5	0.0	15.0	**1.5**	750.0	**1.5**	CHA

ZEO23 B	68.0	1.5	0.0	15.0	**1.5**	750.0	**1.5**	CHA
ZEO23 C	68.0	1.5	0.0	15.0	**2.0**	750.0	**1.0**	Amorphous
ZEO23 D	68.0	1.5	0.0	15.0	**2.5**	750.0	**0.5**	Amorphous
ZEO24 A	68.0	1.5	11.5	3.5	**1.5**	750.0	**1.5**	CHA,MOR
ZEO24 B	68.0	1.5	11.5	3.5	**1.5**	750.0	**1.5**	CHA,MOR
ZEO24 C	68.0	1.5	11.5	3.5	**2.0**	750.0	**2.0**	CHA,MOR
ZEO24 D	68.0	1.5	11.5	3.5	**2.5**	750.0	**2.5**	CHA
ZEO25 A	68.0	1.5	11.5	3.5	**0**	750.0	**3.0**	CHA,MOR
ZEO25 B	68.0	1.5	11.5	3.5	**1.5**	750.0	**1.5**	CHA,MOR
ZEO25 C	68.0	1.5	11.5	3.5	**1.5**	750.0	**1.5**	CHA,MOR
ZEO25 D	68.0	1.5	11.5	3.5	**2.0**	750.0	**1.0**	CHA
ZEO26 A	68.0	1.5	0.0	15.0	**1.5**	850.0	**1.5**	CHA
ZEO26 B	68.0	1.5	0.0	15.0	**1.5**	850.0	**1.5**	CHA
ZEO26 C	68.0	1.5	0.0	15.0	**0.0**	850.0	**3.0**	CHA
ZEO26 D	68.0	1.5	0.0	15.0	**0.0**	850.0	**3.0**	CHA
ZEO27 A	68.0	1.5	0.0	15.0	**0.0**	850.0	**3.0**	CHA
ZEO27 B	68.0	1.5	0.0	15.0	**0.0**	850.0	**3.0**	CHA
ZEO28 A	68.0	1.5	0.0	15.0	**1.5**	850.0	**1.5**	CHA
ZEO28 B	68.0	1.5	0.0	15.0	**1.5**	850.0	**1.5**	CHA
ZEO28 C	68.0	1.5	0.0	15.0	**0.0**	850.0	**3.0**	CHA
ZEO28 D	68.0	1.5	0.0	15.0	**0.0**	850.0	**3.0**	CHA
ZEO29 A	68.0	1.5	0.0	15.0	**1.5**	850.0	**1.5**	CHA
ZEO29 B	68.0	1.5	0.0	15.0	**1.5**	850.0	**1.5**	CHA
ZEO29 C	68.0	1.5	0.0	15.0	**1.5**	850.0	**1.5**	CHA
ZEO29 D	68.0	1.5	0.0	15.0	**1.5**	850.0	**1.5**	CHA

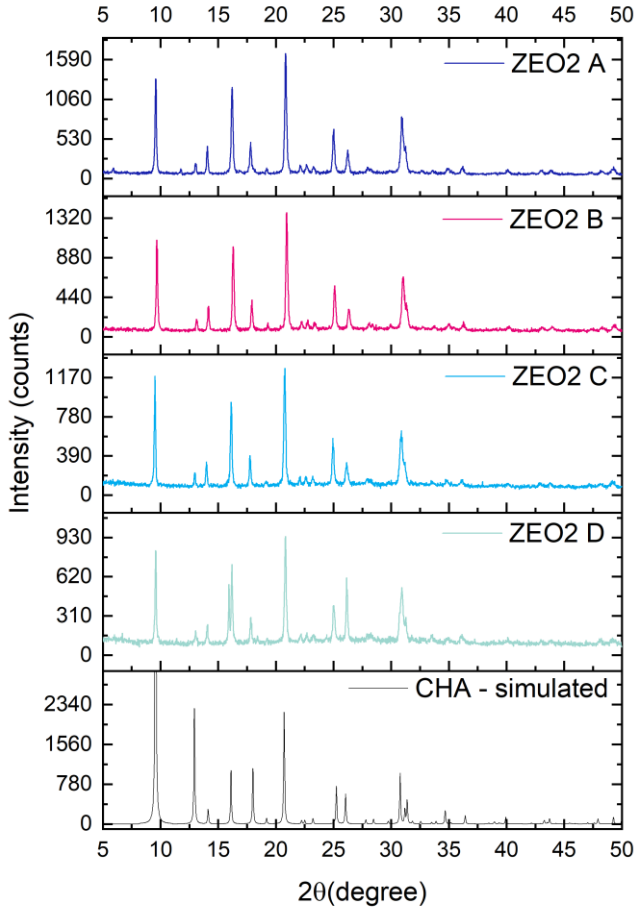

Appendix ii. pXRD patterns attempted chabazite synthesis with FMTMA I^- and TMAdmA OH^-

Appendix iii. Fail repeats of ZEO8 d

	Mol							
Sample name	**SiO_2**	**Al_2O_3**	**Na_2O**	**K_2O**	**FMTMA I^-/ OH^-**	**H_2O**	**TMAdmA OH^-/TEA OH^-**	**Products**
ZEO9 A	68.0	1.5	0.0	50.0	**3.0**	6700.0	0.0	Potassium silicate
ZEO9 B	68.0	1.5	0.0	50.0	**3.0**	6700.0	0.0	Potassium silicate
ZEO9 C	68.0	1.5	0.0	50.0	**3.0**	6700.0	0.0	Potassium silicate
ZEO9 D	68.0	1.5	0.0	50.0	**3.0**	6700.0	0.0	Potassium silicate
ZEO10 A	68.0	1.5	0.0	50.0	**3.0**	6400.0	0.0	Potassium silicate

ZEO10 B	68.0	1.5	0.0	50.0	**3.0**	6400.0	0.0	Potassium silicate
ZEO10 C	68.0	1.5	0.0	50.0	**3.0**	6400.0	0.0	Potassium silicate
ZEO10 D	68.0	1.5	0.0	50.0	**3.0**	6400.0	0.0	Potassium silicate
ZEO11 A	68.0	1.5	0.0	230.0	**3.0**	6400.0	0.0	Potassium silicate
ZEO11 B	68.0	1.5	0.0	230.0	**3.0**	6400.0	0.0	Potassium silicate
ZEO11 C	68.0	1.5	0.0	50.0	**3.0**	6400.0	0.0	Potassium silicate
ZEO11 D	68.0	1.5	0.0	50.0	**3.0**	6400.0	0.0	Potassium silicate
ZEO12 A	68.0	1.5	0.0	50.0	**3.0**	6400.0	0.0	Potassium silicate
ZEO12 B	68.0	1.5	0.0	80.0	**3.0**	6450.0	0.0	Potassium silicate
ZEO12 C	68.0	1.5	0.0	100.0	**3.0**	6500.0	0.0	Potassium silicate
ZEO12 D	68.0	1.5	0.0	150.0	**3.0**	6550.0	0.0	Potassium silicate
ZEO13 A	68.0	1.5	0.0	80.0	**3.0**	6450.0	0.0	Potassium silicate
ZEO13 B	68.0	1.5	0.0	80.0	**3.0**	6450.0	0.0	Potassium silicate
ZEO13 C	68.0	1.5	0.0	80.0	**3.0**	6450.0	0.0	Potassium silicate
ZEO13 D	68.0	1.5	0.0	80.0	**3.0**	6450.0	0.0	Potassium silicate
ZEO14 A	68.0	1.5	0.0	50.0	**3.0**	6450.0	0.0	Potassium silicate
ZEO14 B	68.0	1.5	0.0	55.0	**3.0**	6450.0	0.0	Potassium silicate
ZEO14 C	68.0	1.5	0.0	60.0	**3.0**	6450.0	0.0	Potassium silicate
ZEO14 D	68.0	1.5	0.0	70.0	**3.0**	6450.0	0.0	Potassium silicate
ZEO15 A	68.0	1.5	0.0	50.0	**3.0**	6450.0	0.0	Potassium silicate
ZEO15 B	68.0	1.5	0.0	55.0	**3.0**	6450.0	0.0	Potassium silicate
ZEO15 C	68.0	1.5	0.0	60.0	**3.0**	6450.0	0.0	Potassium silicate
ZEO15 D	68.0	1.5	0.0	70.0	**3.0**	6450.0	0.0	Potassium silicate
ZEO16 A	68.0	1.5	0.0	51.0	**3.0**	6450.0	0.0	Potassium silicate

ZEO16 B	68.0	1.5	0.0	52.0	**3.0**	6450.0	0.0	Potassium silicate
ZEO16 C	68.0	1.5	0.0	53.0	**3.0**	6450.0	0.0	Potassium silicate
ZEO16 D	68.0	1.5	0.0	54.0	**3.0**	6450.0	0.0	Potassium silicate
ZEO17 A	68.0	1.5	0.0	10.0	**3.0**	1600.0	0.0	Amorphous
ZEO17 B	68.0	1.5	0.0	15.0	**3.0**	1600.0	0.0	Amorphous
ZEO17 C	68.0	1.5	0.0	20.0	**3.0**	1600.0	0.0	Amorphous
ZEO17 D	68.0	1.5	0.0	30.0	**3.0**	1600.0	0.0	Unknown
ZEO18 A	68.0	1.5	0.0	30.0	**3.0**	1650.0	0.0	Potassium silicate
ZEO18 B	68.0	1.5	0.0	35.0	**3.0**	1650.0	0.0	Potassium silicate
ZEO18 C	68.0	1.5	0.0	30.0	**3.0**	1650.0	0.0	Potassium silicate
ZEO18 D	71.0	1.8	0.0	28.0	**3.0**	1650.0	0.0	Potassium silicate

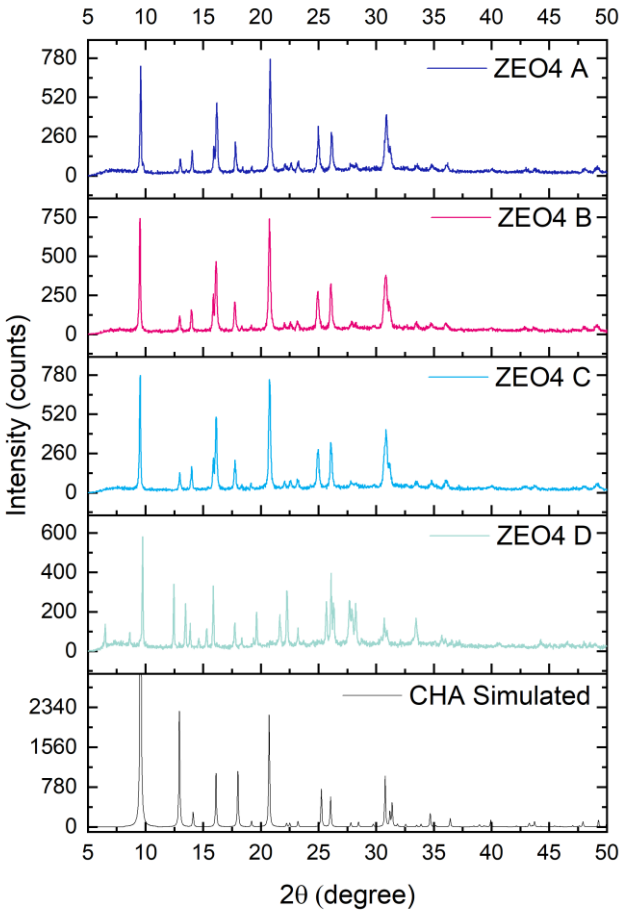

Appendix iv. Chabazite synthesis with varying ratios of TMAda and FMTAM OH

Appendix v. XRF analysis of ZEO3 series of samples

Sample	Na (wt %)	Mg (wt %)	Al (wt %)	Si (wt %)	Fe (wt %)
ZEO3 A	5.92	0.05	2.86	29.34	0.91
ZEO3 B	6.39	0.05	2.62	29.38	1.51
ZEO3 C	7.51	0.03	2.74	29.24	2.35
ZEO3 D	7.55	<0.01	3.00	29.11	3.37

Appendix vi. Zeolite gel composition used for the synthesis in the ZEO4 series of samples

	mol			
	ZEO4-A	**ZEO4-B**	**ZEO4-C**	**ZEO4-D**
SiO_2	68.00	68.00	68.00	68.00
Al_2O_3	1.50	1.50	1.50	1.50
Na_2O	14.13	14.13	0.00	21.00
K_2O	6.87	6.87	21.00	0.00
FMTMA OH	3.00	1.50	3.00	3.00
H_2O	6500.00	3600.00	6400.00	6500.00
TMAdmA	0.00	1.50	0.00	0.00

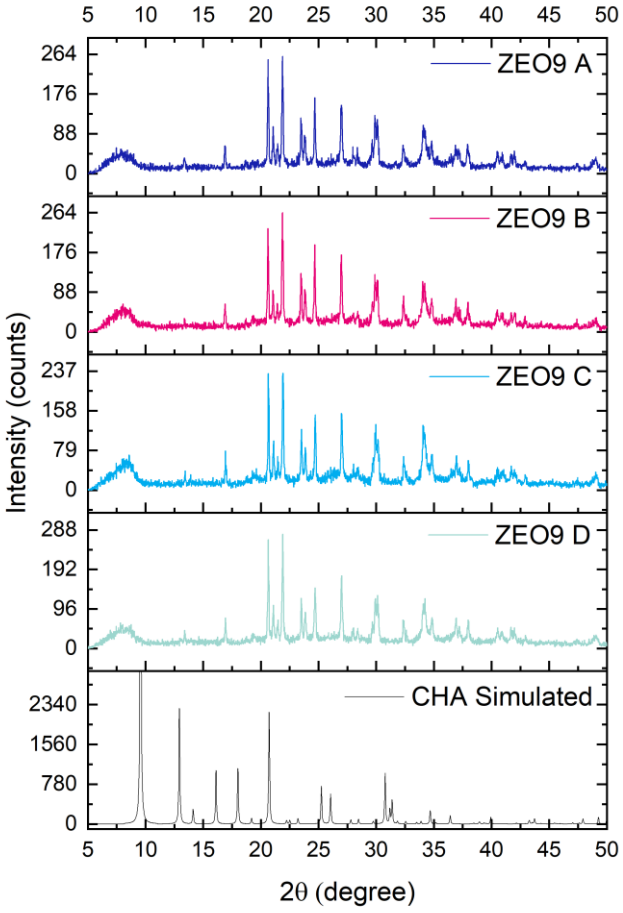

Appendix vii pXRD patterns of failed repeat of ZEO8 D at 96-hour crystallisation time

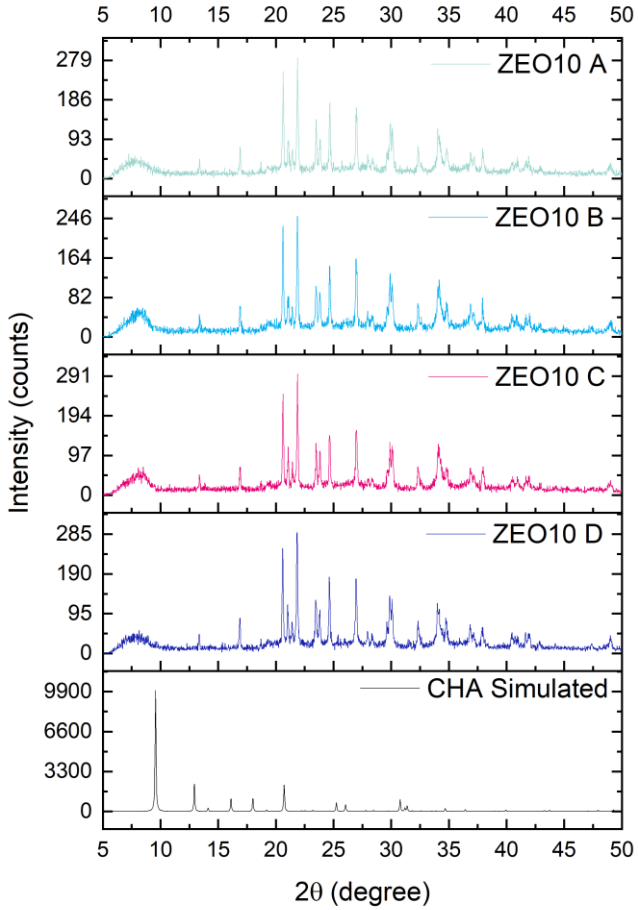

Appendix viii pXRD patterns of failed repeat of ZEO8 D

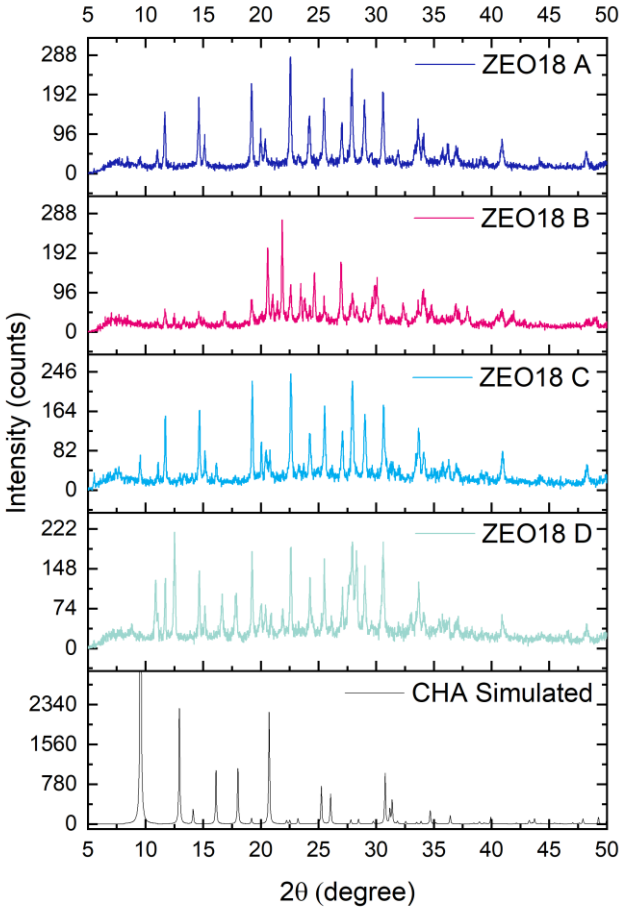

Appendix ix pXRD patterns of failed repeat of ZEO8 D with varied K content in the synthesis gel

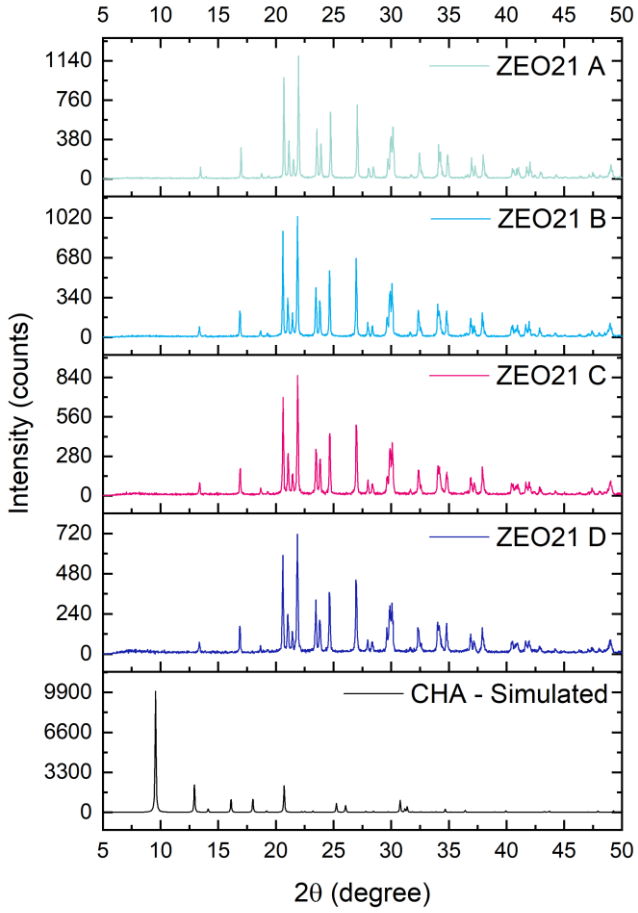

Appendix x. pXRD patterns of sample series of ZEO21

Appendix xi. Zeolite gel composition used for the synthesis in the ZEO21 series of samples

	mol			
	ZEO21-A	**ZEO21-B**	**ZEO21-C**	**ZEO21-D**
SiO_2	68.00	68.00	68.00	68.00
Al_2O_3	1.50	1.50	1.50	1.50
Na_2O	0.00	0.00	0.00	0.00
K_2O	30.00	30.00	30.00	30.00
FMTMA OH	0.50	1.00	1.50	2.00
H_2O	675.00	825.00	980.00	1140.00
TMAdmA	2.50	2.00	1.50	1.00

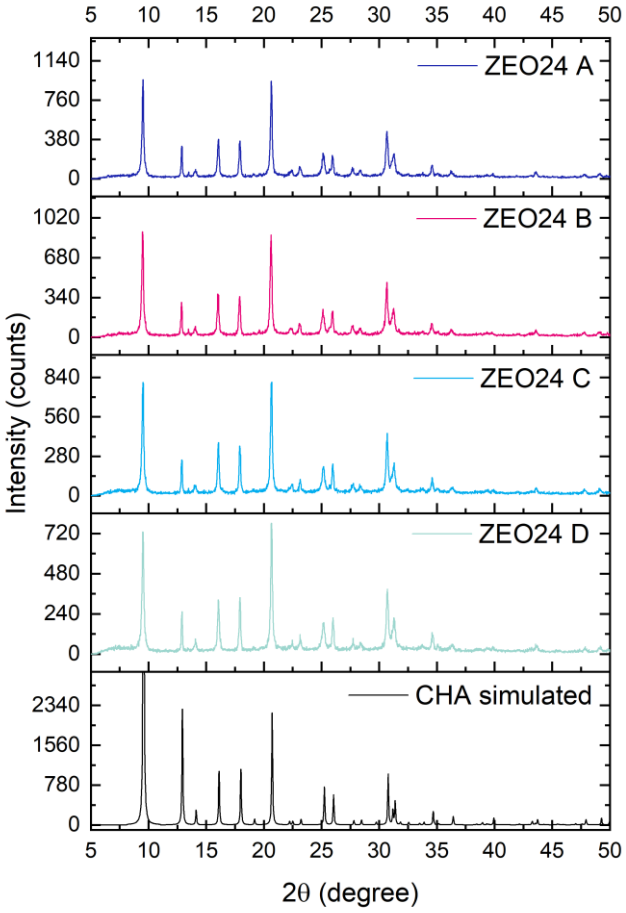

Appendix xii. pXRD patterns of sample series of ZEO24

Appendix xiii. Zeolite gel composition used for the synthesis in the ZEO24 series of samples

	mol			
	ZEO24-A	**ZEO24-B**	**ZEO24-C**	**ZEO24-D**
SiO_2	68.00	68.00	68.00	68.00
Al_2O_3	1.50	1.50	1.50	1.50
Na_2O	0.00	0.00	0.00	0.00
K_2O	15.00	15.00	15.00	15.00
FMTMA OH^-	1.50	1.50	2.00	2.50
H_2O	750.00	750.00	750.00	750.00
TEA OH^-	1.50	1.50	2.00	2.50

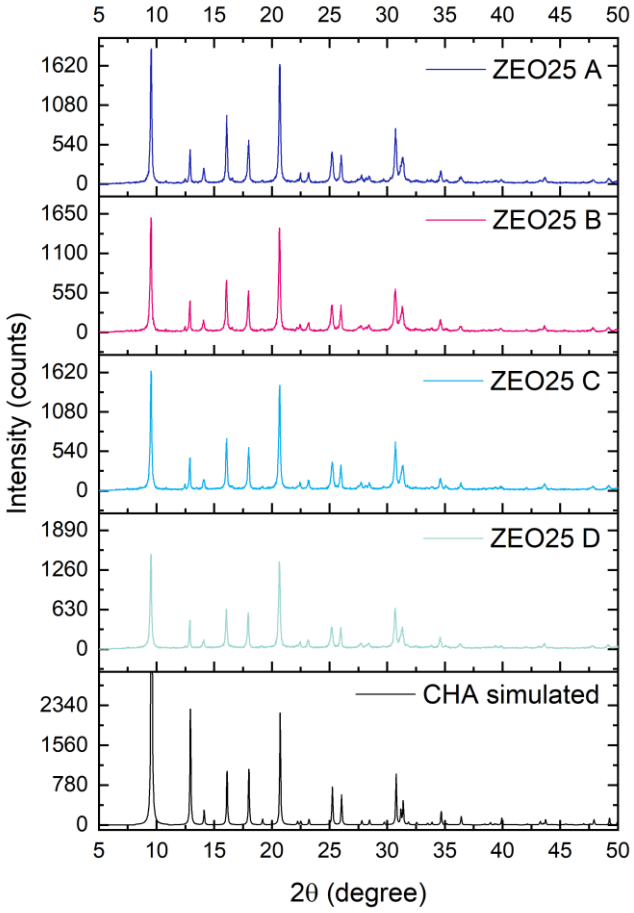

Appendix xiv. pXRD patterns of sample series of ZEO25

Appendix xv. Zeolite gel composition used for the synthesis in the AN1315 series of samples

	mol			
	ZEO25-A	**ZEO25-B**	**ZEO25-C**	**ZEO25-D**
SiO_2	68.00	68.00	68.00	68.00
Al_2O_3	1.50	1.50	1.50	1.50
Na_2O	0.00	0.00	0.00	0.00
K_2O	15.00	15.00	15.00	15.00
FMTMA OH^-	0.00	1.50	1.50	2.00
H_2O	850.00	850.00	850.00	850.00
TEA OH^-	3.00	1.50	1.50	1.00

Appendix xvi. Crystallographic details of all sample ZEO14

	Chabazite	**Mordenite**
Temperature (K)	298	298
Space group	R-3M	Cmcm
X-ray source	Cu	Cu

Diffractometer	Bruker	Bruker
Wavelength (Å)	1.54056	1.54056
a (Å)	13.759	18.593
b (Å)	13.759	20.859
c (Å)	14.863	7.911
Volume (Å^3)	2436.91	3068.36
Phase percent (wt%)	84.7	15.3
Rp	4.47	
Rwp	6.50	

Appendix xvii. Fractional atomic coordinates, occupancies, multiplicities, and isotropic displacement parameters for CHA (in Å^2)

Site	Type	x	y	x	Occup.	Mult.	Biso
O1	O	0.9020	0.0980	0.1227	1	18	1
O2	O	09767	0.3101	0.1667	1	36	1
O3	O	0.1203	0.2405	0.1315	1	36	1
O4	O	0.0000	0.2577	0.0000	1	18	1
T1	Si	0.9997	0.2264	0.1051	1	36	1

Appendix xviii. Fractional atomic coordinates, occupancies, multiplicities, and isotropic displacement parameters for MOR (in Å^2)

Site	Type	x	y	x	Occup.	Mult.	Biso
O1	O	0.28110	0.00000	0.00000	1	8	1
O2	O	0.32680	0.07950	0.25000	1	8	1
O3	O	0.37570	0.09240	0.92430	1	16	1
O4	O	0.23910	0.12230	0.99920	1	16	1
O5	O	0.32530	0.30890	0.25000	1	8	1
O6	O	0.25000	0.25000	0.00000	1	8	1
O7	O	0.37570	0.30580	0.92420	1	16	1
O8	O	0.00000	0.40050	0.25000	1	4	1
O9	O	0.09060	0.30090	0.25000	1	8	1
O10	O	0.00000	0.20130	0.25000	1	4	1

T1	Si	0.30570	0.07360	0.04350	1	16	1
T2	Si	0.30280	0.31060	0.04370	1	16	1
T3	Si	0.08480	0.37910	0.25000	1	8	1
T4	Si	0.08480	0.22270	0.25000	1	8	1